6-26-2015

The Electronic Structure of the Pyranopterin Dithiolene Cofactor and Radical Reporters of Excited State Interactions

Benjamin William Stein

Benjamin W. Stein

Candidate

Chemistry and Chemical Biology

Department

This dissertation is approved, and it is acceptable in quality and form for publication:

Approved by the Dissertation Committee:

Martin L. Kirk , Chairperson

Richard Kemp

Hua Guo

Sang Han

The Electronic Structure of the Pyranopterin Dithiolene Cofactor and Radical Reporters of Excited State Interactions

by

Benjamin William Stein

B.S. Chemistry, University of Northern Colorado, 2007

DISSERTATION

Submitted in Partial Fulfillment of the

Requirements for the Degree of

Doctor of Philosophy

Chemistry

The University of New Mexico

Albuquerque, New Mexico

April, 2015

Dedication

To Katie, who never stopped believing that I was doing something worthwhile.

Acknowledgments

Many hands make light work.
-John Heywood

While the work was never very *light*, the help and support of my coworkers make it *possible*. While I've worked with many excellent scientists, a few have made such contributions that I have a hard time imagining achieving success in their absence. First and foremost, Dr. Joseph Sempombe, who showed me how good humor and tenacity are essential to success in research. I miss our across-the-desk chats where so many exciting ideas were discussed, discarded, and finally perfected. Dr. Logan Giles, for our trips to SSRL and the late nights of data collection . . . I would never have been able to learn so much so quickly without your expertise. Also, Dominic Kersi, Chao Dong, Dr. Regina Mtei-Peters, and Dr. Diana Habel-Rodriguez who have all played their part in helping me become the scientist I am today. I would also like to thank Dr. Shultz and Co., particularly Chris Tichnell and Dan Stasiw who both put up with me not having any idea what I was doing with synthesis and helping me get on the right track. Finally, there is my advisor Dr. Marty Kirk, who gave me the freedom and confidence to explore and succeed.

The Electronic Structure of the Pyranopterin Dithiolene Cofactor and Radical Reporters of Excited State Interactions

by

Benjamin William Stein

B.S. Chemistry, University of Northern Colorado, 2007

Ph.D. Chemistry, University of New Mexico, 2015

Abstract

Crystal structures of multiple molybdenum enzymes clearly demonstrate interesting structural distortions involving the pyranopterin dithiolene. These distortions can be correlated with pyranopterin oxidation state through the use of DFT geometry optimized structures of the possible oxidation states, and these are correlated with enzyme family. The potential role of the pyranopterin dithiolene in electron transfer in the varied enzyme familes has been explored through the use of non-equilibrium Green's function (NEGF) electron transport calculations. These calculations demonstrate clear differences in electron transport behavior as a function of pyranopterin oxidation state.

The Jahn-Teller effect can strongly impact the geometric and electronic structures of molecules which are Jahn-Teller or pseudo-Jahn-Teller active. An intriguing Jahn-Teller effect has been explored in Cp2M(bdt) model compounds, which are shown to be useful models for studying pseudo Jahn-Teller effects in metal dithiolenes and

pyranopterin molybdenum enzymes. Easily synthesized, flexible architecture, and small size enable for complete spectroscopic and theoretical characterization of these classic $Cp_2M(bdt)$ compounds. The three metals studied (M=Ti,V, or Mo) span the d-electron counts from n=0–2, which are the same d electron counts found in molybdenum enzymes. These model systems are shown to be susceptible to either a strong, weak, or no pseudo Jahn-Teller effect, which changes over several orders of magnitude upon oxidation or reduction.

Pendant radicals are shown to be powerful tools probes to better understand the electronic structures of molecules. Radical elaborated square-planar Pt(II) donor-acceptor systems are studied by MCD spectroscopy, even though the parent non-radical elaborated compound is formally diamagnetic. This allows for a level of understanding so far unseen for this well-studied family of molecules. Exchange mixing between the pendant radical and photogenerated open-shell singlet states is shown to be crucial to understanding the complexities associated with the MCD results. This has enabled the determination of many key spectroscopic and electronic structure parameters that are essentially unobtainable by any other methodologies.

Contents

List of Figures

List of Figures

List of Figures

List of Tables

Glossary

AO atomic orbital.

CASSCF complete active space self-consistent field.

CODH carbon monoxide dehydrogenase.

DFT density functional theory.

DMSO dimethyl sulfoxide.

DMSOr dimethyl sulfoxide reductase.

DOS density of states.

EPR electron paramagnetic resonance.

ET electron transfer.

EXAFS x-ray absorption fine structure.

HF Hartree-Fock.

ISC intersystem crossing.

MCD magnetic circular dichroism.

NEGF non-equilibrium Green's function.

PES photoelectron spectroscopy.

PJT pseudo Jahn-Teller.

ppd pyranopterin dithiolene.

QROs quasi-restricted orbitals.

rR resonance Raman.

SO sulfite oxidase.

SOC spin-orbit coupling.

SORCI spectroscopy oriented configuration interaction.

TMAO trimethylamine N-oxide.

XDH xanthine dehydrogenase.

XO xanthine oxidase.

Part I

Spectroscopic and Computational Studies on the Role of the Pyranopterin Dithiolene Cofactor

Chapter 1

Molybdopterin enzyme superfamily

This chapter serves as an overview of important structural and mechanistic aspects of mononuclear molybdenum enzyme chemistry. Many references to background literature are provided, hopefully easing further study. However, pyranopterin dithiolene (ppd) cofactor structure is covered in some depth due to the content of later chapters, and the redox chemistry of model (pyrano)pterins is discussed. An attempt is made to frame the discussion chronologically, with earlier discoveries of ppd structure being discussed first. Particular emphasis is also paid to the electronic structure contributions to reactivity of xanthine oxidase (XO) family enzymes.

Substantial portions of this chapter have been previously published by the author[1–5].

1.1 Molybdenum enzyme superfamily members

The mononuclear molybdenum enzyme superfamily[6, 7] contains a diverse array of members which all utilize the second-row transition metal molybdenum, which is the only second row metal with a known biological function. These enzymes are found in all organisms, from the simplest *Archaea* to *Homo sapiens*, and are among the most ancient enzymes in Nature[8]. The molybdopterin enzyme superfamily is known for catalyzing the two-electron redox processes in a wide variety of polar and non-polar substrates, while avoiding highly reactive and non-selective intermediates such as is found in the cytochrome family of enzymes. This section will serve as a brief overview of molybdenum enzyme structure, function, and spectroscopy with the interested reader being directed to one of many excellent reviews which have been published on the subject[6, 7, 9–11]. As previously mentioned, special emphasis will be paid to recent advances in the understanding of electronic structure contributions to reactivity in XO family enzymes, including CODH.

The molybdopterin enzyme superfamily is conveniently divided up into three constituent families: XO/xanthine dehydrogenase (XDH), sulfite oxidase (SO), and the dimethyl sulfoxide reductase (DMSOr) family (Figure 1.1). These enzyme families contain numerous members, capable of catalyzing two-electron redox chemistry in an astonishingly wide variety of substrates which range from small inorganic molecules such as arsenite[12] and sulfite to aromatics such as ethylbenzene[13, 14] and complicated heterocycles[15].

1.1.1 Xanthine oxidase and carbon monoxide dehydrogenase

The XO enzyme family includes enzymes such as the xanthine oxidoreductases, aldehyde oxidases, nicotinate dehydrogenases, and purine hydroxylases, which catalyze the oxidative hydroxylation of a variety of heterocyclic and aldehyde substrates[9].

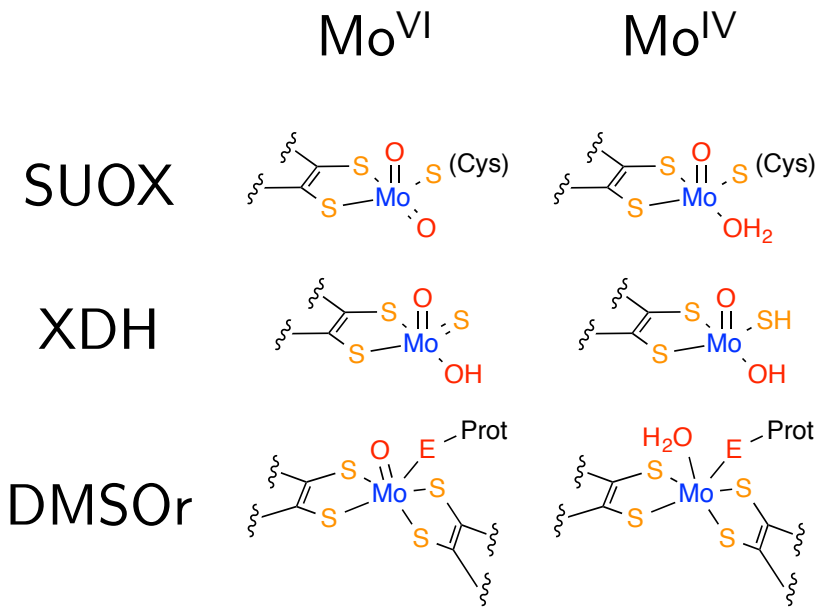

Figure 1.1: Molybdenum enzyme active sites. E=O/S/Se, Prot=proteogenic ligand (e.g. Asp, Ser, etc.)

Unlike the monooxygenases, which formally insert an oxygen atom derived from dioxygen into substrate C-H bonds[16], the molybdenum hydroxylases utilize an oxygen atom derived from metal activated water in the hydroxylation of substrates and generate rather than consume reducing equivalents in the reductive half reaction (Figure 1.2). XOR is important from a human health standpoint, catalyzing the oxidation of hypoxanthine to xanthine and finally xanthine to uric acid. High levels of xanthine in the urine and blood are found in patients that suffer from xanthinuria (type I and type II), which is a rare genetic disorder that results from a deficiency of XOR[6, 7, 10]. This can result in the formation of xanthine kidney stones and even renal failure. High serum uric acid concentrations can lead to uric acid crystallizing in the joints causing inflammation (gout). Finally, within the past decade an appreciation has grown for the role of XOR and AOs in drug metabolism and the activation of various pro-drugs[17].

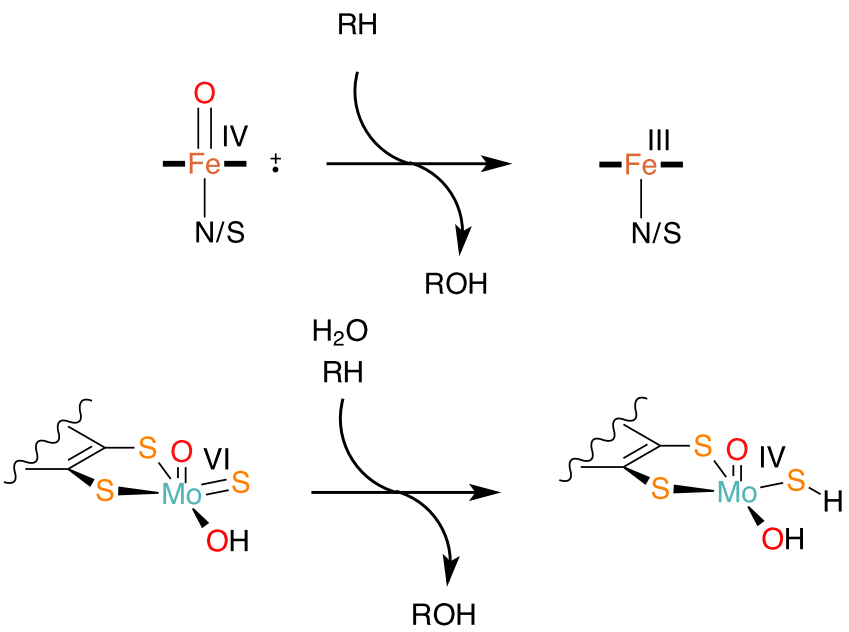

Figure 1.2: Comparison of monooxygenase (top) and hydroxylase (bottom) reactivity.

XO family enzymes catalyze the 2-electron oxidation of a wide variety of substrates according to the general equation:

$$\mathrm{R{-}H + H_2O \longrightarrow R{-}OH + 2\,H^+ + 2\,e^-}$$

where R is typically an aromatic heterocycle or an aldehyde. This reaction represents the formal insertion of an oxygen atom derived from water into a substrate C-H bond, with the generation of two reducing equivalents and two protons. The prototypical member of this enzyme family is xanthine oxidase, which can occur in both an oxidase (XO) and a dehydrogenase (XDH) form, with xanthine oxidoreductase (XOR) referring to the gene product. Throughout this manuscript, the specific enzymes will be referred to as XORs and the enzyme family as the XO family. In the oxidase form (XO), XOR utilizes dioxygen as the ultimate electron acceptor to produce reactive oxygen species (ROS), while the terminal electron acceptor for the dehydrogenase form (XDH) is NAD^+. Oxidase activity only occurs after a reversible disulfide bond

formation in the NAD^+ binding site[18]. XO family enzymes are widespread in biology since very few organisms are known to utilize an alternate degradation pathway for (hypo)xanthine oxidation[19, 20]. Figure 1.3 depicts the generally accepted catalytic cycle of XOR, and includes two of the paramagnetic species that have been detected that are of significant mechanistic importance. The *very rapid* intermediate is a Mo(V)-product complex that results from a split in the catalytic pathway, and the *rapid* species (type 1 and 2) are believed to be paramagnetic analogues of the Michaelis complex. The Mo active site of the AORs is structurally analogous to that found in XORs, but the two enzymes display significant differences in their substrate binding pockets that result in XORs having different substrate specificities than the AOs[15]. Other members of the XO family catalyze the oxidation of substrates such as nicotinate[21] and a variety of quinoline derivatives[22, 23] in addition to the reduction of 4-hydroxylbenzoyl-CoA[24].

A particularly interesting member of the XO family is CODH, which possesses a heterobimetallic Mo-Cu active site[25] (Figure 1.4). Despite the well-known[26, 27] role of Cu in biology as a redox active metal, only Mo is redox active in the oxidation of CO to CO_2:

$$CO + H_2O \longrightarrow CO_2 + 2\,H^+ + 2\,e^-$$

with the Cu ion remaining in the +1 oxidation state throughout the entire catalytic cycle and Mo cycling between the +6 and +4 oxidation states. CODH has also been found[28] to possess hydrogenase activity, capable of oxidizing H_2 to protons and electrons:

$$H_2 \longrightarrow 2\,H^+ + 2\,e^-$$

While Mo functions as the redox active center of catalysis, the Cu is appears to serve as the center of substrate binding, resulting in an interesting organometallic Cu-CO Michaelis complex. Cu(I) is known to bind CO[29, 30], whereas a Cu(II) form of the

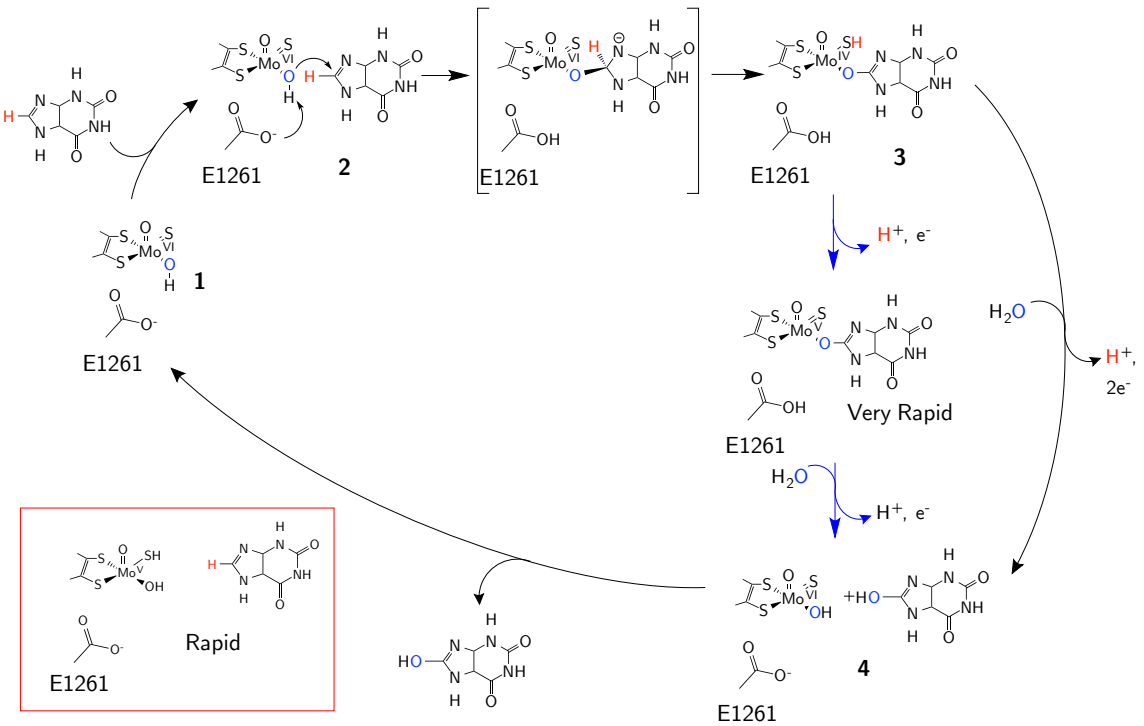

Figure 1.3: Mechanism for oxidation of xanthine to uric acid by XO. Blue arrows show the catalytic cycle during normal physiological conditions, other pathways require particular reaction conditions or substrates.

enzyme would likely be non-functional due to the inability of Cu(II) to bind CO[1].

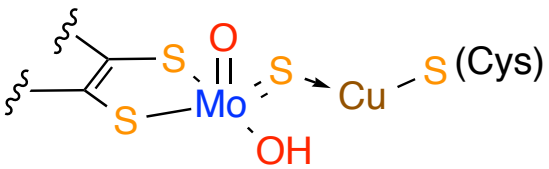

Figure 1.4: Oxidized CODH active site[25].

[1]Interestingly, there are no reports of Cu(II) bound CODH suggesting that the enzyme itself stabilizes the +1 oxidation state even in the presence of air (Cu(I) complexes are typically air-sensitive). A Cu(II) EPR signal only appears after extreme conditions such

Structure

The XO family enzymes contain a five-coordinate square-pyramidal molybdenum active site, two Fe_2S_2 clusters and a redox active flavin (Figure 1.5). Electron transfer is known to occur from the Mo center, through the Fe/S clusters, and finally to the flavin where the reducing equivalents are transferred to NAD^+ or O_2, depending upon whether the enzyme is in the dehydrogenase or oxidase form, respectively[18]. The molybdenum center is coordinated by a bidentate pyranopterin ditholene, an inorganic sulfide, a catalytically labile hydroxide ligand and a non-exchangable axial oxo. Variations on this basic motif include the substitution of sulfide for selenide in nicotinate acid dehydrogenase[21] and in carbon monoxide dehydrogenase (CODH) which catalyzes the oxidation of CO to CO_2. In CODH the sulfido has been appended to a Cu−S(cys) moiety to form a unique bimetallic reaction center.

XO family enzymes have been extensively characterized structurally by X-ray crystallography and EXAFS, and these data have provided a wealth of information regarding coordination geometry, metal-ligand and Mo-Cu bond lengths, the relative orientation of the catalytically essential sulfido ligand, the nature of substrate/product binding, and key amino acid residues in the substrate binding pocket. Approximately 70 years passed between the earliest studies of XOR[31] and the first reported structure of a bacterial AO[32]. However, research efforts in the last 20 years have resulted in the publication of numerous enzyme structures in various forms, and large number of EXAFS studies on enzyme forms not amenable to crystallization. At the time of this writing, there are at least 28 XOR structures that have been deposited into the protein databank (PDB), the vast majority of which are from bovine XO and over half of these were published after 2010[33].

The first structure of AO[32, 34], from *Desulfovibrio gigas* clearly demonstrated

as oxidative wet ashing of the enzyme with H_2SO_4.

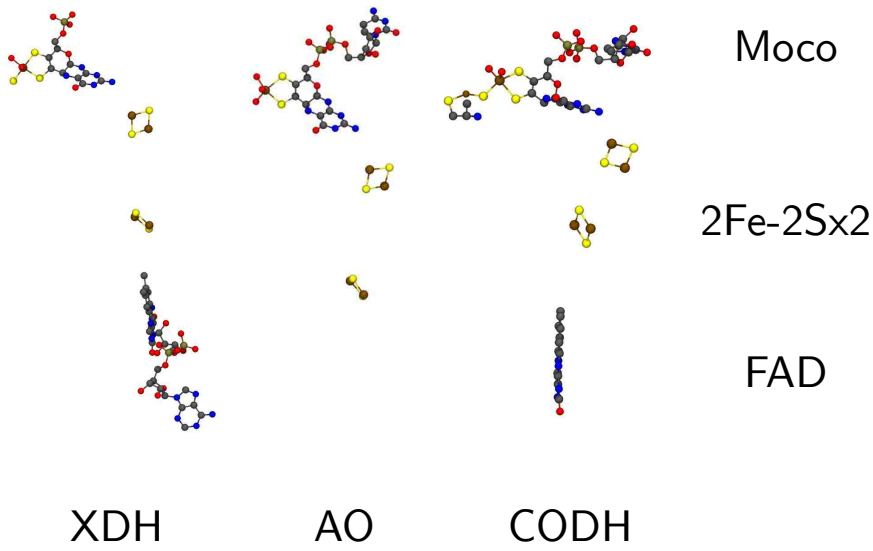

Figure 1.5: Molybdenum hydroxylase redox cofactors: XDH (left), AO (middle) CODH (right). PBD IDs: 3UNC (XDH), 1VLB (AO), 1N5W (CODH). Note that the aldehyde:ferredoxin oxidoreductase from *D. gigas* (shown) lacks the FAD domain, while other AOs possess a FAD similar to the XORs.

dithiolene coordination to Mo in addition to the various amino acid residues implicated in extensive hydrogen bonding interactions with the pyranopterin. AO is a monomeric enzyme which lacks a flavin binding domain, in addition to several subtle but critical differences in the substrate binding residues. Both AO and XOR enzymes possess a catalytically essential glutamate[35] that has been suggested to serve as an active site base in the activation of a metal-bound hydroxide for attack on a substrate carbon atom. However, AO and XOR differ with respect to other amino acid residues in the substrate binding pocket. Namely, AO does not possess the additional Glu and Arg residues that are present in the substrate binding region of XORs to aid in the substrate binding, activation, charge neutralization, and protonation[17].

The general structure of the XORs was known prior to the publication of the first

X-ray structure from enzyme isolated from bovine milk[18] due to sequence similarities with AO, which had been structurally characterized[32]. However, the intimate details regarding the substrate binding pocket, the structure of the flavin binding domain, and the structural basis of XO/XDH interconversion were not known. XO and XDH salicylate structures demonstrated that XOR is a 290kDa homodimer, and showed the geometric relationship between the molybdenum cofactor, 2x[2Fe2S] clusters of the spinach ferredoxin variety, and FAD. The oxidase form of the enzyme differs from the dehydrogenase due to the oxidation of sulfhydryl groups in the flavin binding domain which affects both NAD^+ and O_2 binding and accessibility[18]. The wide variety of substrates oxidized by XOR have resulted in multiple studies directed toward probing the nature of the substrate binding pocket, and include structures with inhibitors (Y-700[36], FYX-051[37], allopurinol[38], TEI-6720[39]) product (urate)[40], and a variety of substrate molecules [41, 42]. Active site residues crucial to catalysis (Figure 1.6) have been determined using site-directed mutagenesis coupled with kinetic studies[35, 43]. The role(s) of these residues in productive substrate orientation has been considered in detail and is a matter ongoing debate. Mechanistic arguments[43] involving Arg 880 stabilizing a built-up of charge on the substrate following nucleophilic attach by the metal-bound hydroxide favor an upside orientation (Figure 1.6). Conversely, urate-bound structures[40] display an upside-down orientation. These issues regarding substrate orientation have recently been addressed using detailed QM/MM calculations, which show that the thermodynamically favored "'upside"' is not the catalytically productive orientation, but rather the upside-down[44, 45].

Spectroscopic studies of XOR and CODH

XO family enzymes have been thoroughly studied by paramagnetic resonance probes (EPR/ENDOR) due to the accessibility of the Mo^V state. Although far fewer optical

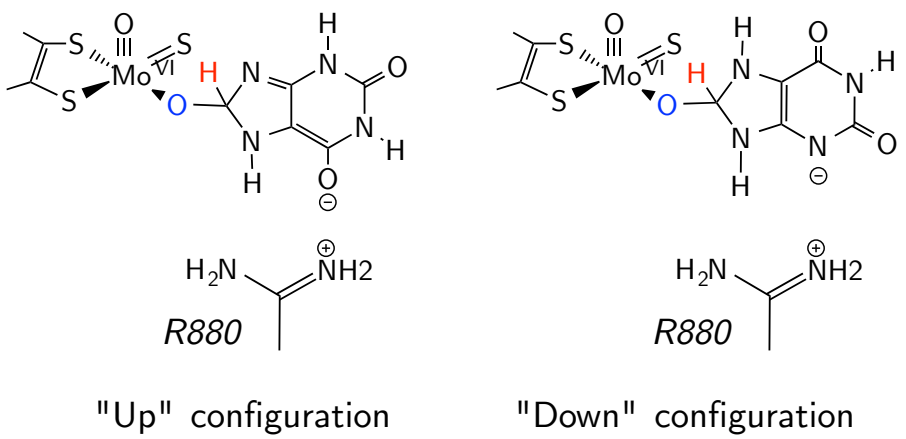

Figure 1.6: Orientation of substrate for the reaction of XO with xanthine. The upside-down orientation has been shown to be favored for catalysis due to a reactant-state destabilization mechanism[44, 45].

studies (e.g. MCD[46], resonance Raman[47]) have been performed on XORs due to the multiple strongly absorbing chromophores (Fe/S and flavin), the information content of these studies has been high and the development of novel methods to collect these data are worthwhile. XORs can form multiple paramagnetic species during the reaction with purines or aldehydes (Figure 1.3) and these have been exhaustively studied in order to gain insight into active site geometric and electronic structure and how this relates to enzyme mechanism. The vast majority of these spectroscopic studies have been performed on bovine XO due to several factors: 1) the large number of EPR active enzyme forms, 2) the high stability of the protein under a variety of conditions, 3) and the well developed purification procedure which results in bovine XO being commercially available at a reasonable price. Four well-characterized EPR detectable species have been observed as a function of incubation time and the particular substrate. These are variously termed aldehyde *inhibited*, *slow* (also called *desulfo*), *rapid* types I and II, and *very rapid* (Figure 1.7). The rapid type I and II species are believed to be paramagnetic analogues of the Michaelis complex that represent different orientations of the substrate in the binding pocket

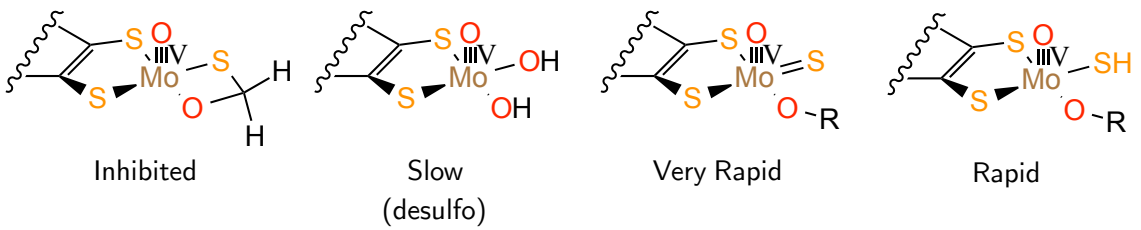

Figure 1.7: EPR active Mo(V) forms of XO.

but not directly coordinated to the Mo center[48]. The desulfo form of XO can be generated by cyanide treatment which removes the catalytically essential terminal sulfido ligand and under specific conditions, dithionite reduction of this catalytically inactive enzyme form yields the slow EPR signal[49].

XO forms a stable product inhibited complex with violopterin, the oxidation product of lumazine. Of interest is that this complex has a low-energy absorption band[50] which is somewhat separated from any other chromophore absorption. This was taken advantage of in a recent study[47] in which sulfur derivatives of lumazine were synthesized, which resulted in the absorption band being shifted to much lower energy and being completely isolated. An additional advantage was this peak was no in resonance with a commonly available rR laser line, allowing for the collection of extremely high quality data. The rR spectra was analyzed within the context of DFT calculations to form a very detailed picture of the structural distortions involved in Mo $\leftrightarrow$ substrate electron transfer and how the pyranopterin may be coupled into ET events. Of particular interest was the first ever identification of low-energy pyranopterin vibrational modes, providing a potential spectroscopic handle for studying how protein mutations can perturb the pyranopterin.

The geometric and electronic structure of aldehyde inhibited XO has been recently probed at high resolution by ENDOR[51] and EPR[2] spectroscopies. Although it was known that aldehyde inhibited XO displayed hyperfine coupling to ^{17}O, ^{33}S, ^{13}C,

and ^{1,2}H nuclei, the general structure of this species had not been unambiguously determined until recently[51]. An unusual aspect of the paramagnetic resonance spectra is the observation of strong and isotropic ^{13}C hyperfine coupling to the carbonyl carbon of the aldehyde. Although originally interpreted as arising from a Mo^{V}-C bond[52], a more recent ^{1,2}H ENDOR study[51] clearly showed that the structure resulted from a Mo(-O-C-S-) four membered chelate ring with a tetrahedral C center. The idea of Mo-C bond formation in the catalytic cycles of XO family enzymes is not new, having been previously postulated for the XO very rapid intermediate based on ENDOR data[52]. However, later ENDOR studies clearly revealed that this is not the case, with the very rapid intermediate possessing a Mo-O-$C_{product}$ linkage[53]. A subsequent EPR and computational study[2] on aldehyde inhibited XO was then used to determine the relative orientation of the ^{95,97}Mo (A_{Mo}), ^{13}C (A_C), and g tensor components to the Mo-ligand bonds. This analysis concluded that the Mo$\rightarrow$C spin delocalization that leads to the large $_{13}$C hyperfine interaction derives from an asymmetric bonding interaction in the Mo(-O-C-S-) chelate. Interestingly, this study related the tetrahedral carbon center in aldehyde inhibited XO with the proposed tetrahedral transition state/intermediate in the oxidation of XO enzyme substrates to show the plausibility of an important Mo-O_{eq}-C delocalization pathway that could contribute to electron transfer between the Mo site and the substrate to lower the energy of the transition state along the reaction coordinate. As such, aldehyde inhibited XO is a rudimentary paramagnetic analogue of the tetrahedral intermediate/transition state along the reaction coordinate, and this highlights the importance of Mo-O_{eq}-C delocalization to enzymatic catalysis.

When compared to the extensive studies which have been done on XOR, spectroscopic studies on CODH are limited. This is a direct result of the smaller number of Mo^{V} species that have been generated for CODH [28, 51, 55] to date, in addition to the inherent problems associated with the additional chromophores common to all XO family enzymes. Chemical reduction of CODH by dithionite, CO, or H_2

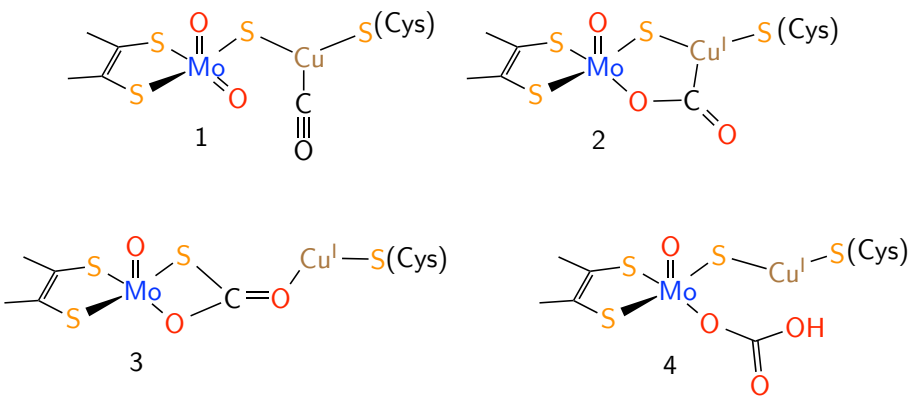

Figure 1.8: Candidates for the EPR signal giving species observed during turnover of CO by CODH[54].

yields a Mo^V EPR signal that displays a nearly isotropic coupling to the diamagnetic $^{63.65}$Cu nucleus. Recently, a detailed combination of ^{13}C and $^{63.65}$Cu ENDOR on the CO species, coupled with spectroscopic and bonding calculations[51] on a variety of trial active-site structures (Figure 1.8) were used to determine potential structures for the signal giving species. Calculated (DFT) spin-Hamiltonian parameters derived for these candidates were then used to eliminate unlikely structures for the spectroscopic intermediate. The authors suggested that MoO_2 dioxo species are unlikely candidates for this intermediate due to the resulting ligand field causing a severe reduction in the g-values, which are inconsistent with the experimental results. The spin-Hamiltonian computations demonstrated that the structure most consistent with the EPR signal-giving species is a modification of a CO bound species (Figure 1.8, structure **1**), and the S-Cu-SCys angle was found to be of critical importance. As S-Cu-SCys angle deviates from 180°, the Cu sp hybridization increases, resulting in an increase in the Cu hyperfine anisotropy. Due to this effect structures 2 and 3 are anticipated (and calculated) to display very rhombic hyperfine anisotropy. However, the calculated g- and ^{13}C hyperfine tensors are in very good agreement with experiment, providing strong supports for structure 1 as the signal giving species. This is important, as structure **1** represents a paramagnetic analogue of the starting

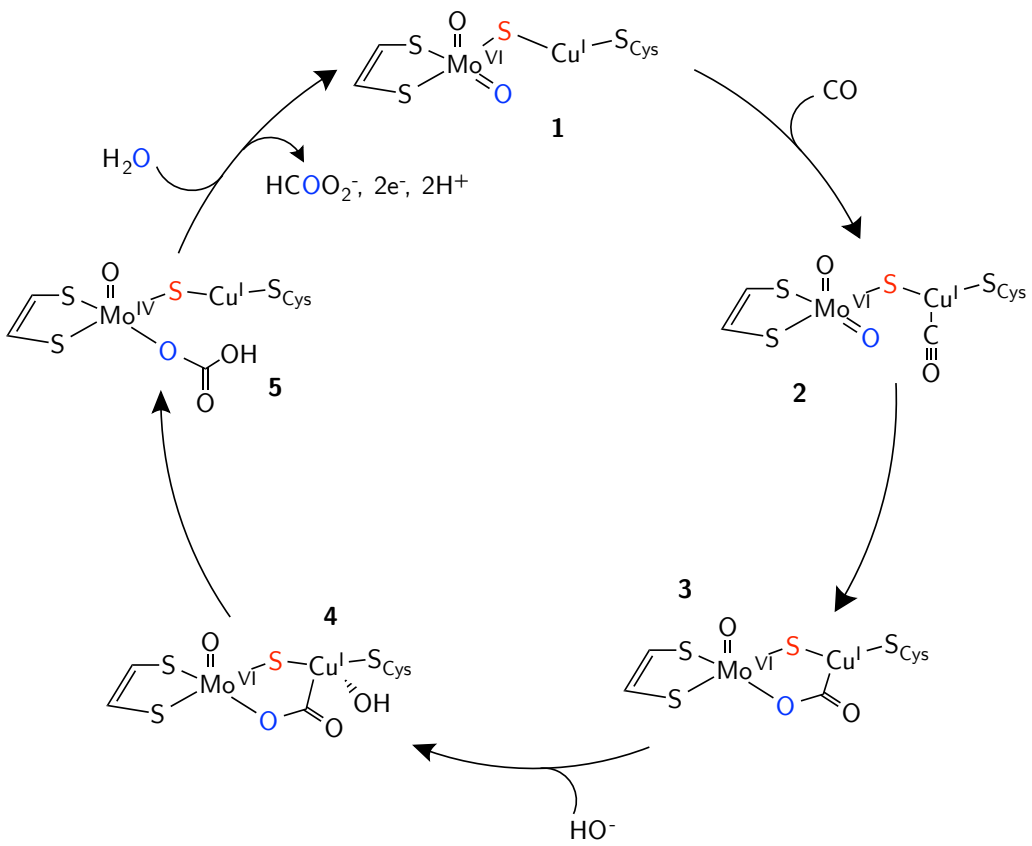

Figure 1.9: Proposed catalytic cycle of CODH[4].

point in the catalytic cycle following binding of substrate. An additional structure was studied computationally which represents a product (bicarbonate) bound species (**4**). Interestingly, this Mo^{V} species is analogous to the very rapid EPR signal seen in related XOR enzymes and recent computational work provides a mechanistic pathway for the formation of this species[4].

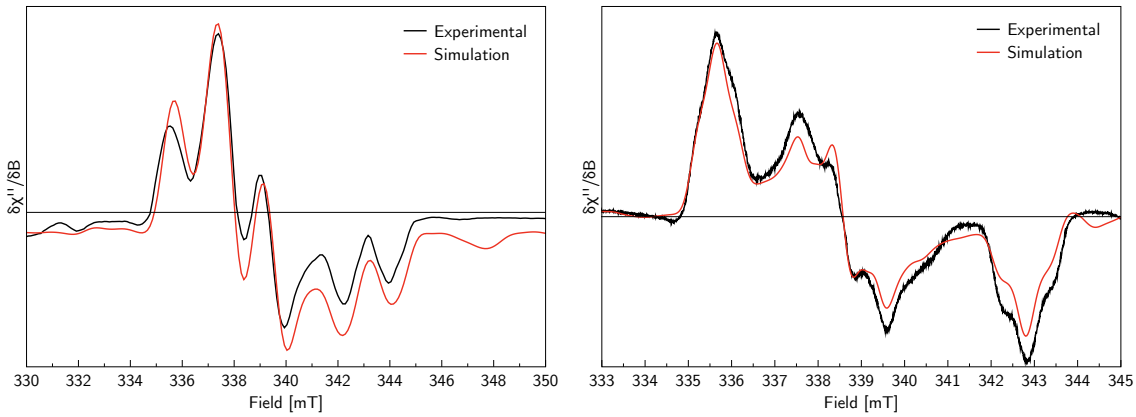

Figure 1.10: EPR of $H^{13}CHO$ (left) and $H_2{}^{17}O$/3-pyridine carboxaldehyde (right) labeled XO inhibited.

Electronic structure contributions to reactivity in molybdenum hydroxylases

While the overall catalytic cycle of XO has been understood for several decades, only recently have studies appeared which attempt to gain an understanding as to how XO activates C-H bonds for hydroxylation without the use of highly reactive intermediates. In particular, it remained to be seen whether the important C-H bond scission/Mo reduction event represented a proton or hydride transfer (Figure 1.11)[2]. While the literature often refers to this transfer as being hydridic, no evidence has been put forth which adequately explains how an electron rich sulfido can serve as a hydride donor. Conversely, if the event is best described as a hydride transfer, an explanation of the electron flow is strongly desired.

Recently, a combined spectroscopic and computational study[2] used XO aldehyde

[2]The possibility of a radical mechanism was briefly considered[56] this was ruled out due to the fact that the enzyme rate was not proportional to substrate one-electron potentials[57].

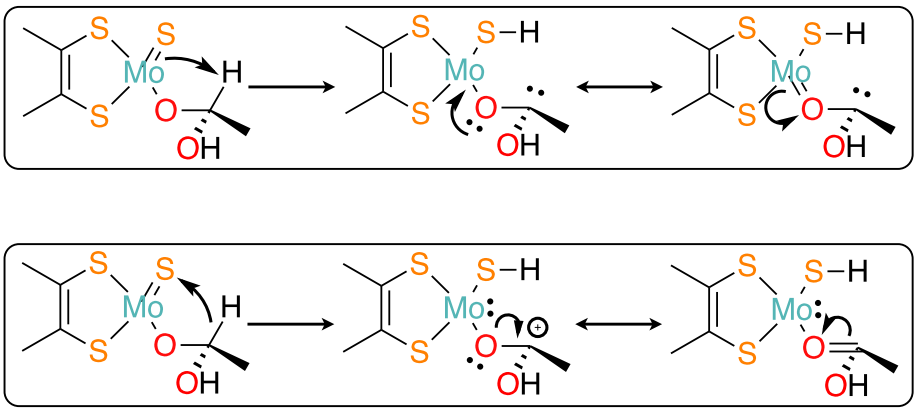

Figure 1.11: Proton (top) vs. hydride (bottom) transfer in XO.

inhibited as a electronic structure model to guide computational work and develop a valence bond description of XO reactivity. Upon reaction of XO with ^{13}C labeled formaldehyde, a large isotropic ^{13}C hyperfine signal is seen[51] (Figure 1.10). This had been previously ascribed to a "transannular" hyperfine interaction, which results from the close proximity of the carbon atom to the spin-bearing d_{xy} orbital. However, ^{17}O labeled XO inhibited shows a large anisotropic ^{17}O hyperfine which arises from a near identical amount of spin density of the C and O atoms, 0.02 electrons. However, the carbon has 5x the amount of s-orbital spin density, due to the sp^3 hybridization of the C atom and this results in the large isotropic hyperfine[3]. The excellent agreement between experiment and theory enabled the determination of the XO inhibited g- and A- tensor orientations, demonstrating the strong directionality associated with the spin containing orbitals (Figure 1.13).

This delocalized Mo-O-C chelate was related to the calculated transition state for "hydride" transfer (Figure 1.3, 2 $\rightarrow$ 3). XO inhibited and the transition state have nearly identical geometries, and so XO inhibited was used as a spectroscopic

[3]A single unpaired electron in a carbon s-orbital results in a A_{iso}=3800 MHz, while an electron in an e.g. p_z-orbital results in an A_{dip}=[214,-108,-108][58]. The values for oxygen are slightly larger.

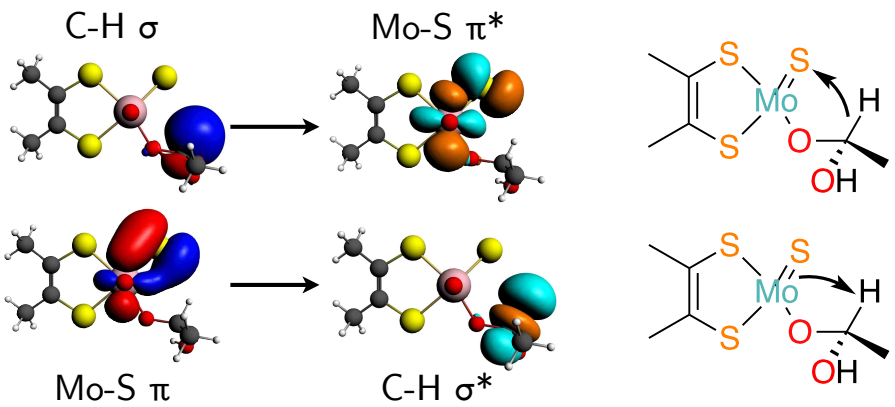

Figure 1.12: NBO description of proton and hydride transfer in XO.

probe of the electronic structure of the transition state. While canonical MOs proved difficult to interpret, natural bond orbitals (NBOs) proved to be an excellent and intuitive way to understand the electronic structure changes which lead to C-H bond scission. NBOs conveniently represent localized lone-pair and bonding regions[59, 60] and provide a convenient way to develop a valence bond, or Lewis structure, description of important bonding interactions along the IM →TS reaction coordinate in XO catalyzed oxidations. Within the NBO framework, the Lewis structure picture laid out in Figure 1.11 can be explored computationally, and the quantitative contributions of the difference Lewis structures to the true wavefunction can be determined. The NBO analysis shows that the C-H bond cleavage results from *equal* contributions of the proton and hydride transfer pathways, and efficient reactivity arises from simultaneous forward and back donation from the Mo-sulfido π and π^* bonds and C-H σ and σ^* bonds (Figure 1.12).

Interestingly, it appears that the reactivity paradigm developed for XO applies to an enzyme with a seemingly vastly different reactivity, CODH. Previously published DFT computations[61, 62] suggest that the CO carbon present in the Mo^{VI}/Cu^{I}-CO complex formed after substrate binding is susceptible to nucleophilic attack by a

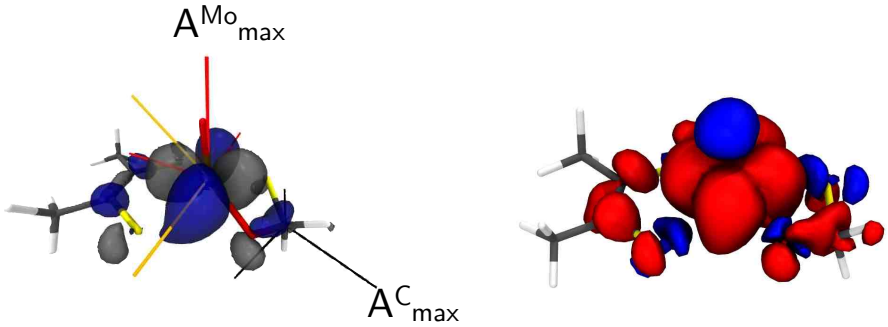

Figure 1.13: Computationally derived tensor orientations (left) and spin density plot (right), showing the delocalized Mo-O-C chelate ring[2].

metal activated water (Mo=O/Mo-OH) to yield a cyclic μ_2-η_2 CO_2 bridged intermediate (Figure 1.9, structure **3**). This intermediate has been proposed to undergo a large geometric rearrangement to form a very stable C-S bonded intermediate, but the stability of the C-S bond leads to large computed reaction barriers for the formation of the reduced Mo^{IV}/Cu^{I} cluster and oxidized product. Support for this intermediate is based upon X-ray crystallographic studies of an n-butylisocyanide inhibited form of CODH[25] that also possesses a C-S bond. Interestingly, EPR and ENDOR spectroscopic studies of the related XO enzyme reveal the presence of an enzyme-substrate C-S bond in an inhibited XO enzyme form (aldehyde inhibited XO) obtained under turnover conditions with certain aldehydes[2]. In light of the inhibitory nature of C-S bond formation in both XO and CODH, we wondered whether the formation of highly covalent enzyme-substrate C-S bonds is a necessary condition for catalysis in CODH. We thought it possible that the elimination of stable C-S bonded structures would lead to reduced activation barriers for CO oxidation and minimal geometric changes at the active site during catalysis. We begin with an electronic description of the cyclic μ_2-η_2 CO_2 bridged intermediate, which is believed to occur prior to C-S bond formation and is common to all currently proposed mechanisms. This provides a convenient starting point for understanding

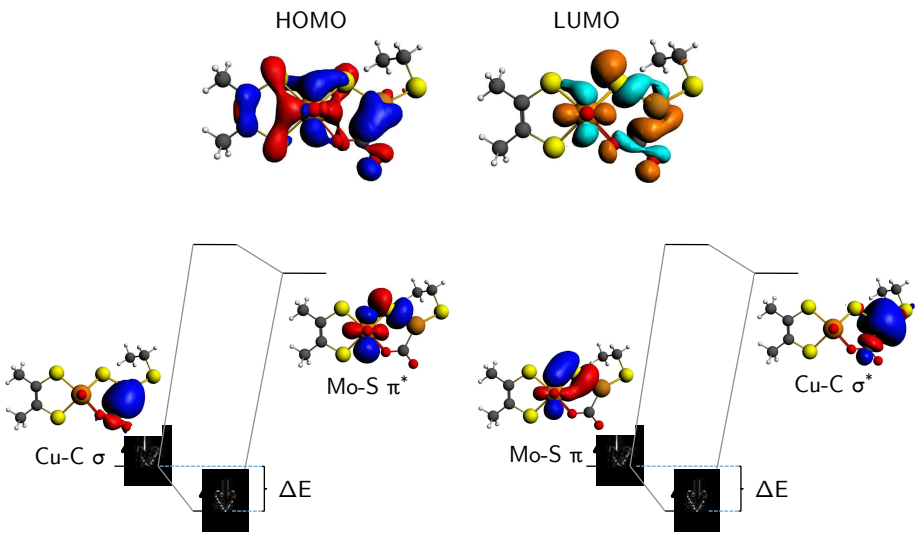

Figure 1.14: Principal donor-acceptor interactions found in the oxidation of CO by CODH (bottom). Also shown are the HOMO and LUMO for the cyclic intermediate (1.9, **3**) in the oxidation of CO by CODH.

electronic structure contributions to catalysis in CODH, particularly with respect to small molecule activation and the avoidance of stable intermediates that possess covalent C-S bonds.

The structure of the cyclic intermediate possesses a bent μ_2-η_2 CO_2 molecule that bridges the Mo and Cu ions. This structure is remarkably similar to that proposed for the transmetallated product of Aresta's complex using organozinc reagents[63], where a bent CO_2 molecule is bound $\mu 2$-$\eta 2$ CO_2 to a heterobinuclear transition metal cluster and activated for nucleophilic attack at carbon. While the CO_2 oxygens are weak Lewis bases, the carbon center is electrophilic. $Cu^{I} \longrightarrow CO_2$ charge donation (back bonding) results in partial occupation of the degenerate CO_2 LUMOs (Figure 1.15), and this will drive a Renner-Teller[64, 65] (R-T) distortion to a bent (C_{2v}) geometry. Structural changes that result from orbital charge transfer between small molecules and transition metals have recently been shown to be a key component in the activation of these ligands[66]. Returning to how this affects , the effect of

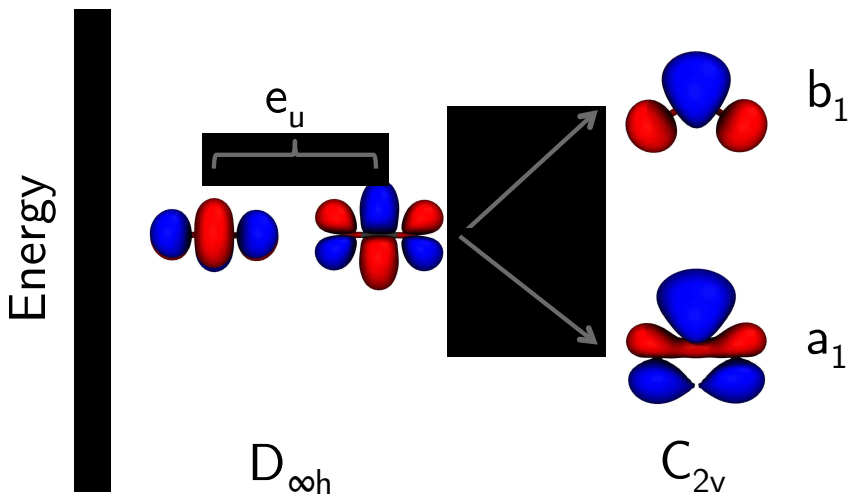

Figure 1.15: LUMOs of CO_2. Orbitals obtained from a CASSCF calculation.

the R-T distortion is to break the degeneracy of the CO_2 LUMOs leading to the in-plane (ip; a_1) LUMO being stabilized relative to the out-of-plane (b_1) LUMO. This bending also results in a LUMO(a_1) orbital with a directional sp hybridized carbon center. Thus, R-T induced bending of CO_2 in the intermediate may activate the coordinated CO_2 for nucleophilic attack at carbon.

Both the HOMO and LUMO of the cyclic intermediate possess CO_2 LUMO(a1) character (Figure 1.14, top and Figure 1.15), highlighting the importance of the CO_2 LUMO(a1) in enzyme reactivity. These highly delocalized orbitals are consistent with the results of EPR and computational studies on CODH models, which show a high degree of Mo-S-Cu covalency[67]. The HOMO of the cyclic intermediate (Figure 1.14, top left) clearly shows the key $Cu^{I} \longrightarrow CO_2$ σ-type charge donation that leads to CO_2 bending and activation for nucleophilic attack. The CO_2 LUMO(a_1) character present in the LUMO of the cyclic intermediate indicates that it possesses an activated CO_2 molecule that is subject to nucleophilic attack by a water or hydroxide at the active site. The LUMO also has considerable Mo-S π^* character that

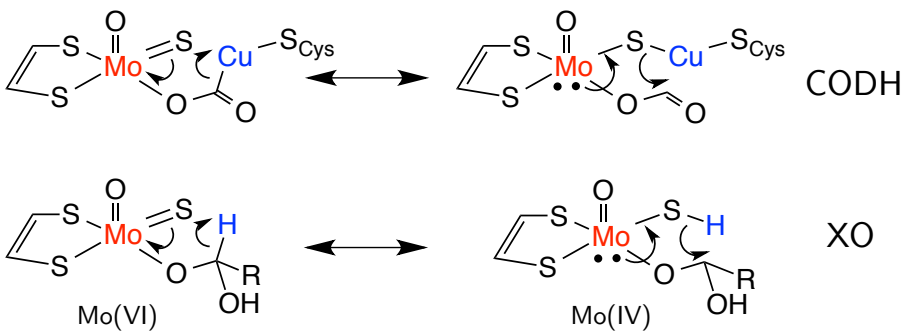

Figure 1.16: Comparisons between XO and CODH reactivity. Note that the Lewis structure description is near identical between XO[2] and CODH[4], but the C-H bond in XO is replaces with a C-Cu bond in CODH.

demonstrates that the Mo ion is not fully reduced. In fact, the occupied Mo character in the HOMO is only ∼30%, compared to ∼60% for the computed fully reduced Mo^{IV} form, *vide infra*. An NBO[59, 60]) analysis of the cyclic intermediate supports this partially reduced character, and further reveals the intermediate to be an approximate 1:1 resonance hybrid of Mo^{VI} and Mo^{IV} structures arising from C-Cu $\sigma \rightarrow$ Mo-S π^* charge donation and Mo-S $\pi \rightarrow$ C-Cu σ^* donation (Figure 1.14). This NBO description of the bonding is remarkably similar to what we previously observed in CODH related XO[2] (Figure 1.16). Specifically, the XO intermediate formed by nucleophillic attack of a metal activated water on the carbonyl carbon of aldehyde substrates possesses an analogous combination of C-H $\sigma \rightarrow$ Mo-S π^* and Mo-S $\pi \rightarrow$ C-H σ^* charge donations, which lead to the resonance structures in Figure 1.16. In this sense, the Cu^{I} ion can be thought of as a "proxy proton" providing a σ orbital which can participate in the crucial donor-acceptor interaction.

1.1.2 Sulfite oxidase

Sulfite oxidase family enzymes catalyze oxygen atom transfer to a variety of substrates, which are typically small, charged, inorganic molecules such as sulfite, ar-

senite, or nitrate[68, 69]. The first coordination sphere around the Mo ion is the typical square pyramidal Mo-oxo (Figure 1.1), but also contains a proteogenic cysteine (or in rare cases, selenocysteine). The role of the cysteine residue has been throughly studied[70] and found to primarily module Mo redox potential. Electron transfer to and from the Mo center has been explored through the use of multiple spectroscopic and flash photolysis techniques, and the role of several conserved amino acids[71, 72], heme domain motion[73], and the binding of small molecules such as chloride[74] or sulfate[75] is rather well understood. SO shows several EPR active forms, typically named for the conditions under which they were generated, and a plethora of studies[76] have throughly characterized the details of these species and there place within the overall catalytic cycle of SO. Recently, the structure of the low-pH (chloride) signal was determined by ESEEM spectroscopy[74], finding that the chloride ion was distant from the Mo site. The contrasts with an earlier CW-EPR study which proposed a chloride ion within the first coordination sphere of the Mo ion[77], which emphasizes the utility of these powerful pulsed EPR methods when dealing with weakly coupled nuclei.

Most recent work has focused upon the YedY and mARC enzymes, both of which are relative newcomers to the study of mononuclear molybdenum enzymes[68, 78, 79]. YedY is located in the periplasm and interacts with a heme-containing redox partner, YedZ. While the physiological substrate of YedY is currently unknown, it does appear to react with a range of sulfur and nitrogen oxides such as DMSO or TMAO. A useful property of YedY is the absence of endogenous chromophores other than the Mo center and the protein can be easily prepared in the Mo^{V} state in nearly quantitative yield. These useful properties result in EPR and MCD[11, 80] spectra of a quality unobtainable by any other molybdenum enzyme. While a crystal structure of YedY is known[78], mARC has only been recently characterized by EXAFS[81]. This study compared the Mo site structure of mARC as compared to HMCS-CT, which is the enzyme responsible for the terminal step in XO biosynthesis (Moco

transfer to apo-XO). While these enzymes have similar amino acid sequences[10], this study showed that the active sites are actually strikingly different in their as-isolated forms.

1.1.3 Dimethyl sulfoxide reductase

DMSOr family enzymes catalyze the two-electron oxidation and reduction[4] of an astonishingly wide variety of substrates, typically through an oxygen atom transfer mechanism involving the lone pair of the substrate and a water derived oxygen atom. The DMSOr family is categorized into three subfamilies based primarily upon their substrate specificity and localization. The substrates effected by DMSOr family enzymes include small molecules such as dimethyl sulfoxide (DMSO), trimethylamine N-oxide (TMAO), formate, nitrate, and arsenite in addition to more exotic organic substrates such as ethylbenzene[14] and other aromatic hydrocarbons.

DMSOr itself is a 88 kDa monomeric protein[82, 83] found in prokaryotic organisms such as *Rhodobacter capsulatus*, a photosynthetic proteobacteria found in aquatic environments. The active site a bis-pyranopterin dithiolene Mo, further coordinated with a serinate oxygen and a water derived oxygen ligand (oxo, hydroxy, or aquo). Other DMSOr family enzymes typically have an overall similar protein fold, however, significant active site differences can be found involving the metal, protein ancillary ligand, pyranopterin oxidation state, and substrate binding. These include substitution of Mo for W, replacement of serine by any number of anionic ligands, ring opening of the pyran, and oxidation of the pyrazine moiety.

[4]With the notable exception of acetylene hydratase, which performs the non-redox hydration reaction of acetylene to acetaldehyde.

Spectroscopic studies

Due to their unique reactivity and interesting bis-ppd active site, there has been an ongoing interest in studying DMSOr family enzymes. The lack of additional chromophores beyond the molybdenum active site makes the type III family members particularly suitable for spectroscopic investigations, including electron paramagnetic resonance (EPR), magnetic circular dichroism (MCD), electronic absorption, resonance Raman (rR), and X-ray based techniques. Determination of the precise structural features of DMSOr by X-ray diffraction provided structures which were initially misleading. Features such as detached ppd ligands were assigned catalytic relevance, and the molybdenum coordination sphere was often shown to have extremely unlikely geometries including atoms well within their respective van der Walls radii. x-ray absorption fine structure (EXAFS) studies suggested that these structures were in error, and this was supported by later X-ray structures.

EPR studies of DMSOr show that the enzyme exists in multiple EPR active forms, depending upon the specific reaction conditions[84]. Of particular interest is the "high-g split" species, which is formed under turnover conditions. It was later shown[85] that this species appears to lie on the catalytic pathway, and is not a dead end or off-pathway species. Furthermore, it was shown that this species can be generated in quantitative amounts by the use of TMAO as opposed to the physiological DMSO, offering the possibility of very high quality spectroscopic studies. This allowed for the study of high-g split species was studied in great detail[1] by EPR and MCD spectroscopy, which were analyzed within the context of advanced *ab initio* calculations. Many spectroscopic features of this intermediate were unique, including the identification of a rhombic A-tensor. This pointed to a low-symmetry relaxed geometry, and computational results show how the strongly mixed SOMO give this result. The MCD spectra of the intermediate showed an intriguing double pseudo-A term, arising from transitions involving two pseudo-degenerate sets of or-

bitals, which was illuminated by the spectroscopy oriented configuration interaction (SORCI) calculations. Finally, it was shown that the unique spectroscopic features of this intermediate arise from the relaxed nature of the 6-coordinate intermediate, and that the stability of this species is responsible for the buildup of the same during catalysis.

Despite the uncanny agreement between theory and experiment in the previous work, recent EXAFS work[86] claim that the interpretation of these results is incorrect. Interpretation of these EXAFS results suggest that the intermediate is actually in a 5-coordinate form, and represents a off-pathway species which comes about due to the dissociation of the serine residue. No attempt was made to determine how well this structure explains the other spectroscopic results, nor was it explained how the difficult problem of determining the coordination number of light atoms in the presence of multiple strong scatters was solved.

1.2 The Pyranopterin Dithiolene Cofactor

The pyranopterin dithiolene cofactor (ppd)[5] is a heterocyclic chelating ligand found in all molybdenum and tungsten containing enzymes, with the exception of nitrogenase[3, 87]. Typically the ppd is depicted as in Figure 1.17, showing the cofactor in tetrahydro oxidation state. The ppd cofactor contains a bicyclic pyrimidine and pyrazine system, collectively called the pterin. This is linked to a pyran-dithiolene, and the pyran ring is known to exhibit reversible ring-chain isomerism. Bacterial molybdenum and tungsten enzymes have a dinucleotide base bound to the phos-

[5]In the literature the ppd cofactor is often (somewhat confusingly) referred to as the molybdopterin cofactor. When molybdopterin is bound to a molybdenum atom it is then called the molybdenum cofactor, or Moco. This work uses the term (ppd) to refer to the organic cofactor with or without an appended metal atom.

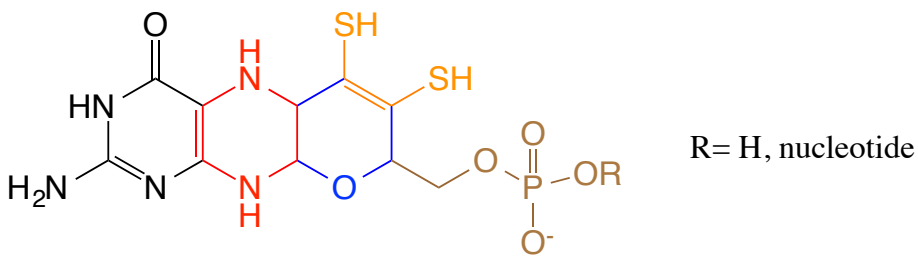

Figure 1.17: Pyranopterin dithiolene cofactor structure. Black: pyrimidine, red: pyrazine, blue: pyran, orange: dithiolene, brown: phosphate/phosphate dinucleotide.

phate, either adenosine, guanosine, or cytidine, while eukaryotes only posess a simple phosphate group.

Pyranopterin structure and model chemistry

While studies of molybdenum containing enzymes date back into the early 1900s[31, 88], clear evidence of a labile cofactor did not appear until the 1960s when it was shown that nitrate reductase and XDH possessed a common cofactor[89, 90]. This discovery of a common metal-binding cofactor moiety in molybdenum containing enzymes immediately spurred studies to discover it's precise chemical nature. However, the extreme instability of this cofactor in the when freed from carrier proteins greatly hindered work. The study[91] of decomposition products[6] gave clues as to the structure of the ppd cofactor, the exact mode of molybdenum binding remained elusive. It was not until the discovery of a carboxamido protected form of the cofactor[92] that the dithiolene structure was proven.

Model chemistry has provided signifigant insight into the diverse behavior of the pyranopterin dithiolene cofactor[93]. Studies have typically focused on either synthesis of the bare cofactor[94–96] or molybdenum/tungsten bound analogues[97–99]. Studies of ppd mimics such as methylated pterins[100, 101] and pyranopterins have

[6]Referred to as Form A or B, depending on how the cofactor was oxidized.

shed insight on the potential redox properties of the pyranopterin moiety itself, with many interesting insights being drawn as to how the pyran ring couples with the complicated redox behavior of the pterin. The dithiolene has been extensively studied, with varying amounts of additional chemical functionality being attached; models range from simple ene-diothiolate and benzenedithiolate[102] to quinoxaline[99] and full pyranopterin ditholene models[103].

1.3 References

(1) Mtei, R. P.; Lyashenko, G.; Stein, B.; Rubie, N.; Hille, R.; Kirk, M. L. *J. Am. Chem. Soc.* **2011**, *133*, 9762–9774, DOI: 10.1021/ja109178q.

(2) Sempombe, J.; Stein, B.; Kirk, M. L. *Inorg. Chem.* **2011**, *50*, 10919–10928, DOI: 10.1021/ic201477n.

(3) Kirk, M. L.; Stein, B. In *Comprehensive Inorganic Chemistry II*; Elsevier: 2013, pp 263–293.

(4) Stein, B. W.; Kirk, M. L. *Chem. Commun.* **2014**, *50*, 1104–1106, DOI: 10.1039/C3CC47705C.

(5) Stein, B. W.; Kirk, M. L. *J. Biol. Inorg. Chem.* **2014**, *20*, 183–194, DOI: 10.1007/s00775-014-1212-8.

(6) Hille, R.; Hall, J.; Basu, P. *Chem. Rev.* **2014**, *114*, 3963–4038, DOI: 10.1021/cr400443z.

(7) Hille, R. *Chem. Rev.* **1996**, *96*, 2757–2816.

(8) Workun, G. J.; Moquin, K.; Rothery, R. A.; Weiner, J. H. *Microbiol. Mol. Biol. Rev.* **2008**, *72*, 228–248, DOI: 10.1128/MMBR.00041-07.

(9) Hille, R. *Arch. Biochem. Biophys.* **2005**, *433*, 107–116, DOI: 10.1016/j.abb.2004.08.012.

(10) Hille, R.; Nishino, T.; Bittner, F. *Coord. Chem. Rev.* **2011**, *255*, 1179–1205, DOI: 10.1016/j.ccr.2010.11.034.

(11) Pushie, M. J.; Doonan, C. J.; Moquin, K.; Weiner, J. H.; Rothery, R.; George, G. N. *Inorg. Chem.* **2011**, DOI: 10.1021/ic101280m.

(12) Ellis, P. J.; Conrads, T.; Hille, R.; Kuhn, P. *Structure* **2001**, *9*, 125–132.

(13) Kniemeyer, O.; Heider, J. *J. Biol. Chem.* **2001**, *276*, 21381–21386, DOI: 10.1074/jbc.M101679200.

(14) Kloer, D. P.; Hagel, C.; Heider, J.; Schulz, G. E. *Structure* **2006**, *14*, 1377–1388, DOI: 10.1016/j.str.2006.07.001.

(15) Kitamura, S.; Sugihara, K.; Ohta, S. *Drug Metab. Pharmacokinet.* **2006**, *21*, 83–98, DOI: 10.2133/dmpk.21.83.

(16) Altun, A.; Kumar, D.; Neese, F.; Thiel, W. *J. Phys. Chem. A* **2008**, *112*, 12904–12910, DOI: 10.1021/jp802092w.

(17) Pryde, D. C.; Dalvie, D.; Hu, Q.; Jones, P.; Obach, R. S.; Tran, T.-D. *J. Med. Chem.* **2010**, *53*, 8441–8460, DOI: 10.1021/jm100888d.

(18) Enroth, C.; Eger, B. T.; Okamoto, K.; Nishino, T.; Pai, E. F. *Proc. Natl. Acad. Sci. U.S.A.* **2000**, *97*, 10723.

(19) Li, X.-L.; Fu, Y. *J. Mol. Struct. THEOCHEM* **2008**, *856*, 112–118.

(20) Cultrone, A.; Scazzocchio, C.; Rochet, M.; Montero Morán, G.; Drevet, C.; Fernández Martín, R. *Mol. Microbiol.* **2005**, *57*, 276–290, DOI: 10.1111/j.1365-2958.2005.04686.x.

(21) Wagener, N.; Pierik, A. J.; Ibdah, A.; Hille, R.; Dobbek, H. *Proc. Natl. Acad. Sci. U.S.A.* **2009**, *106*, 11055–11060, DOI: 10.1073/pnas.0902210106.

(22) Canne, C.; Stephan, I.; Finsterbusch, J.; Lingens, F.; Kappl, R.; Fetzner, S.; Hüttermann, J. *Biochemistry* **1997**, *36*, 9780–9790, DOI: 10.1021/bi970581d.

(23) Tshisuaka, B.; Kappl, R.; Huettermann, J.; Lingens, F. *Biochemistry* **1993**, *32*, 12928–12934, DOI: 10.1021/bi00210a047.

(24) Gibson, J.; Dispensa, M.; Harwood, C. S. *J. Bacteriol.* **1997**, *179*, 634–642.

(25) Dobbek, H.; Gremer, L.; Kiefersauer, R.; Huber, R.; Meyer, O. *Proc. Natl. Acad. Sci.* **2002**, *99*, 15971–15976.

(26) Solomon, E. I.; Szilagyi, R. K.; DeBeer George, S.; Basumallick, L. *Chem. Rev.* **2004**, *104*, 419–458, DOI: 10.1021/cr0206317.

(27) Solomon, E. I. *Inorg. Chem.* **2006**, *45*, 8012–8025, DOI: 10.1021/ic060450d.

(28) Wilcoxen, J.; Hille, R. *J. Biol. Chem.* **2013**, *288*, 36052–36060, DOI: 10.1074/jbc.M113.522441.

(29) Tsuda, T.; Habu, H.; Saegusa, T. *J. Chem. Soc., Chem. Commun.* **1974**, 620–620, DOI: 10.1039/C39740000620.

(30) Strauss, S. H. *J. Chem. Soc. Dalton Trans.* **2000**, 1–6, DOI: 10.1039/A908459B.

(31) Dixon, M.; Thurlow, S. *Biochem. J.* **1924**, *18*, 976.

(32) Romão, M. J.; Archer, M.; Moura, I.; Moura, J. J. G.; LeGall, J.; Engh, R.; Schneider, M.; Hof, P.; Huber, R. *Science* **1995**, *270*, 1170–1176, DOI: 10.1126/science.270.5239.1170.

(33) Dobbek, H. *Coord. Chem. Rev.* **2011**, *255*, 1104–1116, DOI: 10.1016/j.ccr.2010.11.017.

(34) Rebelo, J.; Dias, J.; Huber, R.; Moura, J.; Romão, M. *J. Biol. Inorg. Chem.* **2001**, *6*, 791–800, DOI: 10.1007/s007750100255.

(35) Leimkühler, S.; Stockert, A. L.; Igarashi, K.; Nishino, T.; Hille, R. *J. Biol. Chem.* **2004**, *279*, 40437–40444, DOI: 10.1074/jbc.M405778200.

(36) Fukunari, A.; Okamoto, K.; Nishino, T.; Eger, B. T.; Pai, E. F.; Kamezawa, M.; Yamada, I.; Kato, N. *J. Pharmacol. Exp. Ther.* **2004**, *311*, 519–528, DOI: 10.1124/jpet.104.070433.

(37) Okamoto, K.; Matsumoto, K.; Hille, R. In, Proceedings of the ... 2004, DOI: 10.1073/pnas.0400973101.

(38) Okamoto, K.; Eger, B. T.; Nishino, T.; Pai, E. F.; Nishino, T. *Nucleosides Nucleotides Nucleic Acids* **2008**, *27*, 888–893, DOI: 10.1080/15257770802146577.

(39) Okamoto, K.; Eger, B. T.; Nishino, T.; Kondo, S.; Pai, E. F.; Nishino, T. *J. Biol. Chem.* **2003**, *278*, 1848–1855, DOI: 10.1074/jbc.M208307200.

(40) Okamoto, K.; Kawaguchi, Y.; Eger, B. T.; Pai, E. F.; Nishino, T. *J. Am. Chem. Soc.* **2010**.

(41) Pauff, J. M.; Zhang, J.; Bell, C. E.; Hille, R. *J. Biol. Chem.* **2008**, *283*, 4818–4824, DOI: 10.1074/jbc.M707918200.

(42) Cao, H.; Pauff, J. M.; Hille, R. *J. Biol. Chem.* **2010**, *285*, 28044–28053, DOI: 10.1074/jbc.M110.128561.

(43) Pauff, J. M.; Hemann, C. F.; Jünemann, N.; Leimkühler, S.; Hille, R. *J. Biol. Chem.* **2007**, *282*, 12785–12790, DOI: 10.1074/jbc.M700364200.

(44) Metz, S.; Thiel, W. *J. Am. Chem. Soc.* **2009**, *131*, 14885–14902, DOI: 10.1021/ja9045394.

(45) Metz, S.; Thiel, W. *J. Phys. Chem. B* **2010**, *114*, 1506–1517, DOI: 10.1021/jp909999s.

(46) Jones, R. M.; Inscore, F. E.; Hille, R.; Kirk, M. L. *Inorg. Chem.* **1999**, *38*, 4963–4970, DOI: 10.1021/ic990154j.

(47) Dong, C.; Yang, J.; Leimkühler, S.; Kirk, M. L. *Inorg. Chem.* **2014**, *53*, 7077–7079, DOI: 10.1021/ic500873y.

(48) Gutteridge, S.; Tanner, S. J.; Bray, R. C. *Biochem. J.* **1978**, *175*, 869–878.

(49) Malthouse, J. P. G.; WIlliams, J. W.; Bray, R. C. **1981**.

(50) Hemann, C.; Ilich, P.; Stockert, A. L.; Choi, E.-Y.; Hille, R. *J. Phys. Chem. B* **2005**, *109*, 3023–3031, DOI: 10.1021/jp046636k.

(51) Shanmugam, M.; Zhang, B.; McNaughton, R. L.; Kinney, R. A.; Hille, R.; Hoffman, B. M. *J. Am. Chem. Soc.* **2010**, *132*, 14015–14017, DOI: 10.1021/ja106432h.

(52) Howes, B. D.; Bray, R. C.; Richards, R. L.; Turner, N. A.; Bennett, B.; Lowe, D. J. *Biochemistry* **1996**, *35*, 1432–1443, DOI: 10.1021/bi9520500.

(53) Manikandan, P.; Choi, E. Y.; Hille, R.; Hoffman, B. M. *J. Am. Chem. Soc.* **2001**, *123*, 2658–2663.

(54) Shanmugam, M.; Wilcoxen, J.; Habel-Rodriguez, D.; Cutsail III, G. E.; Kirk, M. L.; Hoffman, B. M.; Hille, R. *J. Am. Chem. Soc.* **2013**, *135*, 17775–17782, DOI: 10.1021/ja406136f.

(55) Zhang, B.; Hemann, C. F.; Hille, R. *J. Biol. Chem.* **2010**, *285*, 12571, DOI: 10.1074/jbc.M109.076851.

(56) Page, C. C.; Moser, C. C.; Chen, X.; Dutton, P. L. *Nature* **1999**, *402*, 47–52, DOI: 10.1038/46972.

(57) Stockert, A. L.; Shinde, S. S.; Anderson, R. F.; Hille, R. *J. Am. Chem. Soc.* **2002**, *124*, 14554–14555, DOI: 10.1021/ja027388d.

(58) Morton, J. R.; Preston, K. F. *J. Magn. Reson.* **1978**, *30*, 577–582.

(59) Weinhold, F.; Landis, C. R., *Valency and bonding : a natural bond orbital donor-acceptor perspective*; Cambridge University Press: Cambridge, UK ; New York, 2005.

(60) Weinhold, F.; Landis, C. R. *Chem. Eur. J.* **2001**, *2*, 91–104.

(61) Hofmann, M.; Kassube, J. K.; Graf, T. *J. Biol. Inorg. Chem.* **2005**, *10*, 490–495, DOI: 10.1007/s00775-005-0661-5.

(62) Siegbahn, P. E. M.; Shestakov, A. F. *J. Comput. Chem.* **2005**, *26*, 888–898, DOI: 10.1002/jcc.20230.

(63) Yeung, C. S.; Dong, V. M. *J. Am. Chem. Soc.* **2008**, *130*, 7826–7827, DOI: 10.1021/ja803435w.

(64) Bersuker, I. B., *Electronic Structure and Properties of Transition Metal Compounds*, 2nd; John Wiley and Sons: Hoboken, New Jersey, 2010.

(65) Bersuker, I. B., *The Jahn-Teller Effect*, 1st; Cambridge University Press: Cambridge, UK, 2006.

(66) Gorinchoy, N. N.; Balan, I. I.; Bersuker, I. B. *Computational and Theoretical Chemistry* **2011**, *976*, 113–119, DOI: 10.1016/j.comptc.2011.08.013.

(67) Gourlay, C.; Nielsen, D. J.; White, J. M.; Knottenbelt, S. Z.; Kirk, M. L.; Young, C. G. *J. Am. Chem. Soc.* **2006**, *128*, 2164–2165, DOI: 10.1021/ja056500f.

(68) Kappler, U. *Biochimica et Biophysica Acta (BBA) - Bioenergetics* **2011**, *1807*, 1–10, DOI: 10.1016/j.bbabio.2010.09.004.

(69) Feng, C.; Tollin, G.; Enemark, J. H. *Biochim. Biophys. Acta BBA-Proteins Proteomics* **2007**, *1774*, 527–539, DOI: 10.1016/j.bbapap.2007.03.006.

(70) Helton, M. E.; Pacheco, A.; McMaster, J.; Enemark, J. H.; Kirk, M. L. *J. Inorg. Biochem.* **2000**, *80*, 227–233, DOI: 10.1016/S0162-0134(00)00082-9.

(71) Johnson-Winters, K.; Davis, A. C.; Arnold, A. R.; Berry, R. E.; Tollin, G.; Enemark, J. H. *J. Biol. Inorg. Chem.* **2013**, DOI: 10.1007/s00775-013-1010-8.

(72) Emesh, S.; Rapson, T. D.; Rajapakshe, A.; Kappler, U.; Bernhardt, P. V.; Tollin, G.; Enemark, J. H. *Biochemistry* **2009**, *48*, 2156–2163, DOI: 10.1021/bi801553q.

(73) Astashkin, A. V.; Elmore, B. O.; Fan, W.; Guillemette, J. G.; Feng, C. *J. Am. Chem. Soc.* **2010**, *132*, 12059–12067, DOI: 10.1021/ja104461p.

(74) Klein, E. L.; Astashkin, A. V.; Ganyushin, D.; Riplinger, C.; Johnson-Winters, K.; Neese, F.; Enemark, J. H. *Inorg. Chem.* **2009**, *48*, 4743–4752, DOI: 10.1021/ic801787s.

(75) Astashkin, A. V.; Johnson-Winters, K.; Klein, E. L.; Byrne, R. S.; Hille, R.; Raitsimring, A. M.; Enemark, J. H. *J. Am. Chem. Soc.* **2007**, *129*, 14800–14810, DOI: 10.1021/ja0704885.

(76) Pushie, M. J.; George, G. N. *Coord. Chem. Rev.* **2011**, *255*, 1055–1084, DOI: 10.1016/j.ccr.2011.01.056.

(77) Doonan, C. J.; Wilson, H. L.; Bennett, B.; Prince, R. C.; Rajagopalan, K. V.; George, G. N. *Inorg. Chem.* **2008**, *47*, 2033–2038, DOI: 10.1021/ic7017083.

(78) Loschi, L.; Brokx, S. J.; Hills, T. L.; Zhang, G.; Bertero, M. G.; Lovering, A. L.; Weiner, J. H.; Strynadka, N. C. J. *J. Biol. Chem.* **2004**, *279*, 50391–50400, DOI: 10.1074/jbc.M408876200.

(79) Havemeyer, A.; Bittner, F.; Wollers, S.; Mendel, R.; Kunze, T.; Clement, B. *J. Biol. Chem.* **2006**, *281*, 34796–34802, DOI: 10.1074/jbc.M607697200.

(80) Yang, J.; Rothery, R.; Sempombe, J.; Weiner, J. H.; Kirk, M. L. *J. Am. Chem. Soc.* **2009**, *131*, 15612–15614, DOI: 10.1021/ja903087k.

(81) Giles, L. J.; Ruppelt, C.; Yang, J.; Mendel, R. R.; Bittner, F.; Kirk, M. L. *Inorg. Chem.* **2014**, *53*, 9460–9462, DOI: 10.1021/ic5015863.

(82) Romão, M. J. *Dalton Trans.* **2009**, 4053–4068, DOI: 10.1039/b821108f.

(83) McAlpine, A. S.; McEwan, A. G.; Bailey, S. *J. Mol. Biol.* **1998**, *275*, 613–623, DOI: 10.1006/jmbi.1997.1513.

(84) Bennett, B.; Benson, N.; McEwan, A. G.; Bray, R. C. *Eur. J. Biochem.* **1994**, *225*, 321–331.

(85) Cobb, N.; Conrads, T.; Hille, R. *J. Biol. Chem.* **2005**, *280*, 11007–11017, DOI: 10.1074/jbc.M412050200.

(86) Pushie, M. J.; Cotelesage, J. J. H.; Lyashenko, G.; Hille, R.; George, G. N. *Inorg. Chem.* **2013**, *52*, 2830–2837, DOI: 10.1021/ic301660e.

(87) Seefeldt, L. C.; Hoffman, B. M.; Dean, D. R. *Annu. Rev. Biochem.* **2009**, *78*, 701, DOI: 10.1146/annurev.biochem.78.070907.103812.

(88) Morgan, E. J.; Stewart, C. P.; Hopkins, F. G. *Proc. R. Soc. Lond. B Biol. Sci.* **1922**, *94*, 109–131, DOI: 10.1098/rspb.1922.0047.

(89) Pateman, J. A.; Cove, D. J.; Rever, B. M.; Roberts, D. B. *Nature* **1964**, *201*, 58–60, DOI: 10.1038/201058a0.

(90) Rajagopalan, K. V.; Johnson, J. L. *J. Biol. Chem.* **1992**, *267*, 10199–10202.

(91) Johnson, J. L.; Hainline, B. E.; Rajagopalan, K. V.; Arison, B. H. *J. Biol. Chem.* **1984**, *259*, 5414–5422.

(92) Kramer, S. P.; Johnson, J. L.; Ribeiro, A. A.; Millington, D. S.; Rajagopalan, K. V. *J. Biol. Chem.* **1987**, *262*, 16357–16363.

(93) Basu, P.; Burgmayer, S. N. J. *Coord. Chem. Rev.* **2011**, *255*, 1016–1038, DOI: 10.1016/j.ccr.2011.02.010.

(94) Bradshaw, B.; Dinsmore, A.; Collison, D.; Garner, C. D.; Joule, J. A. *J. Chem. Soc., Perkin Trans. 1* **2001**, 3232–3238, DOI: 10.1039/B108576J.

(95) Bradshaw, B.; Dinsmore, A.; Ajana, W.; Collison, D.; Garner, C. D.; Joule, J. A. *J. Chem. Soc., Perkin Trans. 1* **2001**, 3239–3244, DOI: 10.1039/B108579B.

(96) Burgmayer, S. J. N.; Pearsall, D.; Blaney, S.; Moore, E.; Sauk-Schubert, C. *J. Biol. Inorg. Chem.* **2004**, *9*, 59–66, DOI: 10.1007/s00775-003-0496-x.

(97) Burgmayer, S. J. N.; Stiefel, E. I. *J. Chem. Educ.* **1985**, *62*, 943–953.

(98) Burgmayer, S. J. N.; Kim, M.; Petit, R.; Rothkopf, A.; Kim, A.; BelHamdounia, S.; Hou, Y.; Somogyi, A.; Habel-Rodriguez, D.; Williams, A.; Kirk, M. L. *J. Inorg. Biochem.* **2007**, *101*, 1601–1616, DOI: 10.1016/j.jinorgbio.2007.07.012.

(99) Matz, K. G.; Mtei, R. P.; Leung, B.; Burgmayer, S. J. N.; Kirk, M. L. *J. Am. Chem. Soc.* **2010**, *132*, 7830–7831, DOI: 10.1021/ja100220x.

(100) Karber, L. G.; Dryhurst, G. *J. Electroanal. Chem. Interfacial Electrochem.* **1982**, *136*, 271–289.

(101) Karber, L. G.; Dryhurst, G. *J. Electroanal. Chem. Interfacial Electrochem.* **1984**, *160*, 141–157.

(102) Inscore, F. E.; McNaughton, R. L.; Westcott, B. L.; Helton, M. E.; Jones, R.; Dhawan, I. K.; Enemark, J. H.; Kirk, M. L. *Inorg. Chem.* **1999**, *38*, 1401–1410.

(103) Williams, B. R.; Fu, Y.; Yap, G. P. A.; Burgmayer, S. J. N. *J. Am. Chem. Soc.* **2012**, *134*, 19584–19587, DOI: 10.1021/ja310018e.

Chapter 2

Pyranopterin Oxidation State and Electron Transfer

The pyranopterin dithiolene has a remarkably complex structure and redox behavior, with model chemistry demonstrating this complex electronic structure behavior. However, the specifics of how this behavior is involved in specific biologically relevant function in unknown. Here is presented work which links experimentally derived ppd structures to pyranopterin oxidation state[1] and that this oxidation state is further correlated with enzyme function. Through the use of advanced DFT non-equilibrium Green's function calculations, it is shown that the pyranopterin oxidation states have remarkably distinct electron transport behavior and that these behaviors are linked the the aformentioned specific electronic needs of the specific enzyme family.

Substantial portions of this chapter have been previously published by the author[1].

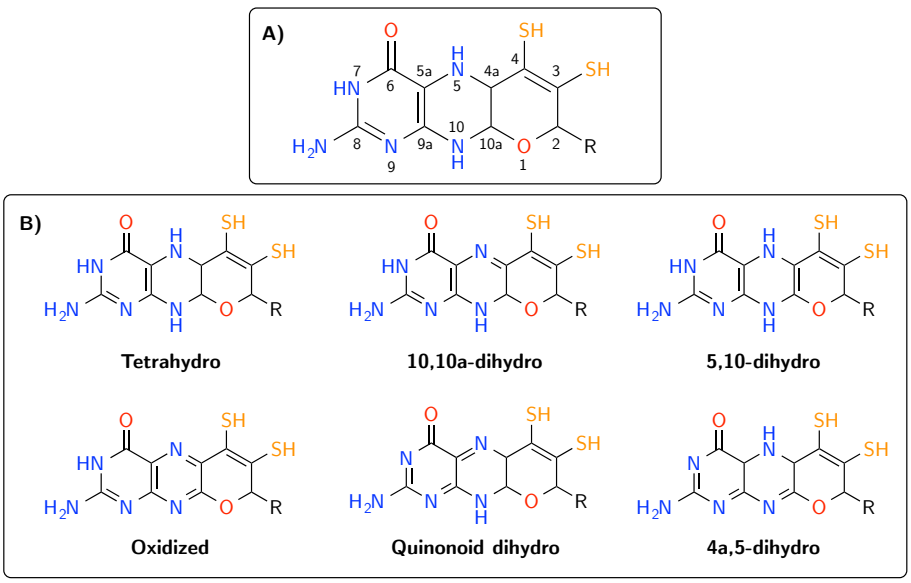

Figure 2.1: Pyranopterin dithiolene oxidation states explored in this study. A) Pyranopterin dithiolene numbering, B) Tetrahydro, dihydro tautomers, and oxidized pyranopterins.

2.1 Relationship between oxidation state and geometry

The molybdenum cofactor is possibly the most redox active cofactor in biology, with the pterin having three oxidation states (reduced tetrahydro, intermediate dihydro, and fully oxidized), the dithiolene having a reduced dithiolene, one-electron oxidized radical, and fully oxidized dithione forms in addition to the three accessible oxidation states of molybdenum. This results in a potential nine redox equivalents, discounting the additional six present in the bis-ppd DMSOr family enzymes. Furthermore, the pyran ring has been shown to exist in open forms in two enzymes thus far, EBDH[2] and NarGHI[3][1].

[1]Interestingly these two enzymes also appear to have the bicylic pterin in different oxidation states, fully oxidized for EBDH and partially oxidized for NarGHI.

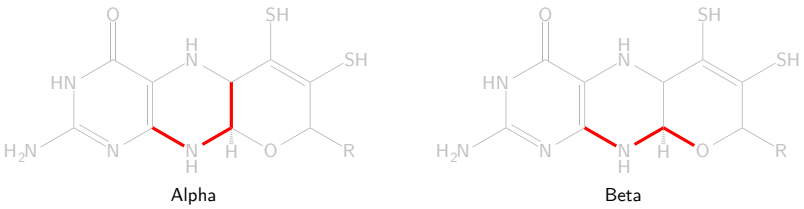

Figure 2.2: Definition of α and β dihedral angles.

In contrast to the extensive model and electrochemical studies discussed in Section 1.2, limited computational studies have been performed to make sense of the vast number of potential oxidation and dihydro tautomers. In[4] 40 dihydro pterin tautomers had their energetics compared in order to determine the most likely form, assuming a dihydro oxidation state. The authors determined that the 10,10a form (Figure 2.1) is the most stable tautomer, but could not rule out the 5,10- or 4a,5-dihydro pterins due to the limits of computational accuracy. In addition they mentioned the potential for the quinonoid dihydro to be a relevant tautomer, in particular due to it being the immediate precursor of the 10,10a-dihyrdo after the oxidation of a tetrahydro pterin[5, 6].

An examination of molybdenum containing enzyme crystal structures reveals an intriguing relationship between two critical geometric parameters (Figure 2.2) in nearly all of the published structures (Figure 2.3. These angles appear to have a linear correlation, with more distorted pyranopterins falling on the lower left and more planar being found on the upper right. Also of particular interest is that it was seen that the angles were clustered by enzyme family, with the pyranopterins found in SUOX family enzymes being similar to the distal pyranopterin found in DMSOr enzymes and the XO family pyranopterins being similar to the proximal DMSOr pyranopterins. This strongly suggests a link between pyranopterin geometry and function as the XOR family pyranopterins are known be be involved in electron transport due to the proximity of the terminal amine to an 2Fe2S cluster, as are the

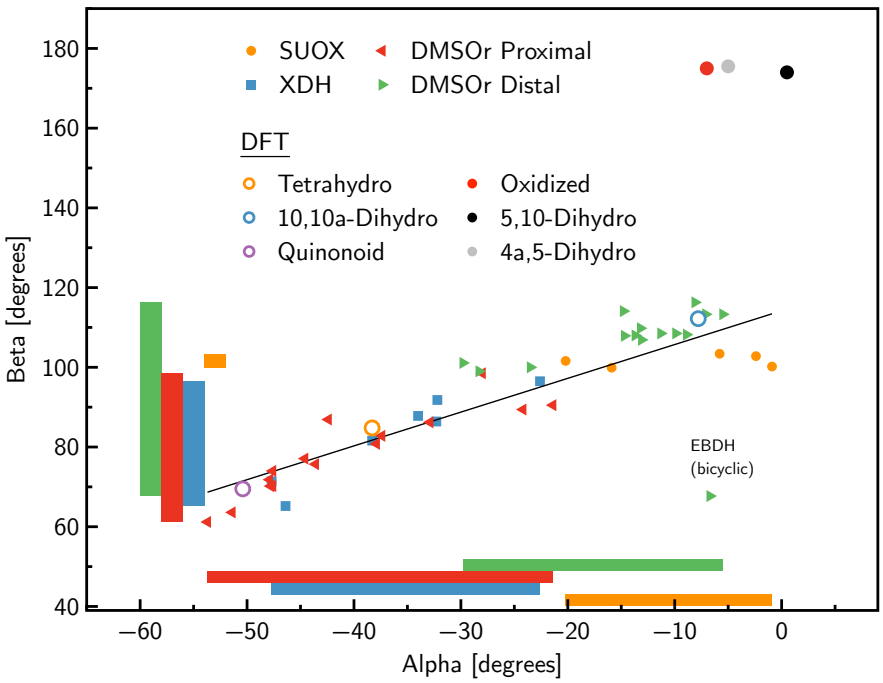

Figure 2.3: Correlation between alpha/beta and molybdenum enzyme family. Also shown are DFT derived geometries for differing pterin oxidation states.

DMSOr proximal pyranopterins[2].

With this starting point, we hypothesized that these dihedral angles were correlated with specific pyranopterin oxidation states, and that these oxidation states possessed unique electronic structures which made them well suited to particular biological roles. While the tetrahydro and oxidized pyranopterins only possess one tautomer each, there are a great number of potential dihydro tautomers. Based upon the previous computational work[4], the pyranopterin oxidations states and tautomers listed in Figure 2.1 were selected and DFT optimized models of these were constructed.

[2]The proximal pyranopterin is so named because of its *proximity* to the Fe-S clusters in DMSOr family enzymes.

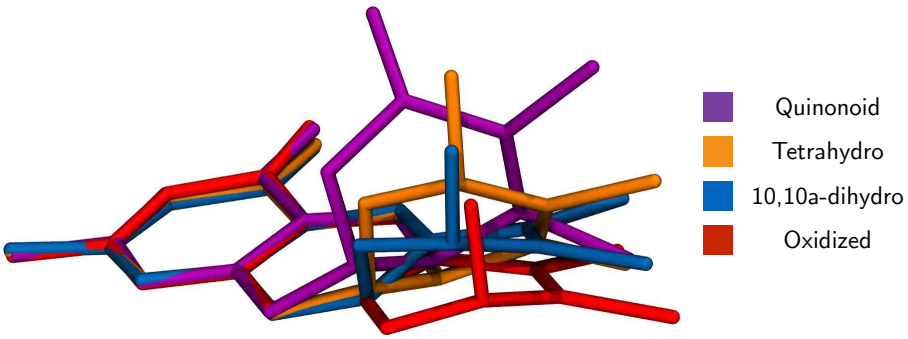

Figure 2.4: DFT optimized (PBE/TZP) pyranopterin dithiolenes.

After optimization of the six potential structures, several could be immediately ruled out due to their distance from the experimental geometries: the oxidized, 5,10-dihydro, and the 4a,5-dihydro (Figure 2.3)[3]. Figures 2.3 and 2.4 show that the different oxidation states are clearly distinct from one another, and that these oxidation states are correlated with enzyme family: tetrahydro and possibly quinonoidal with XDH/DMSOr proximal and 10,10a-dihydro with SO and DMSOr distal. The quinonoid/tetrahydro distinction is an interesting one, as the quinonoid/10,10a-dihydro pair fall on opposite ends of the distortion coordinate raising speculation that the dihydro oxidation state is solely responsible for all observed pyranopterin geometries.

During the past 15 years, the literature[7–9] seems to have settled upon the tetrahydro being the favored oxidation state. This raises the possible counter-point that the tetrahydro geometry is responsible for all of the observed geometries, and that the protein simply enforces these distorted geometries on the pyranopterin dithiolene. An examination of the energetics involved[4] in such a distortion (Figure 2.5)

[3]These geometries address an additional concern, namely that α and β are not truely independent measurements (i.e. due to bond torsions or sterics).

[4]Few experimental values are available for such an analysis, however the experimental reduction potential of 10,10a- dihydropterins is available[5] and was used to reference the

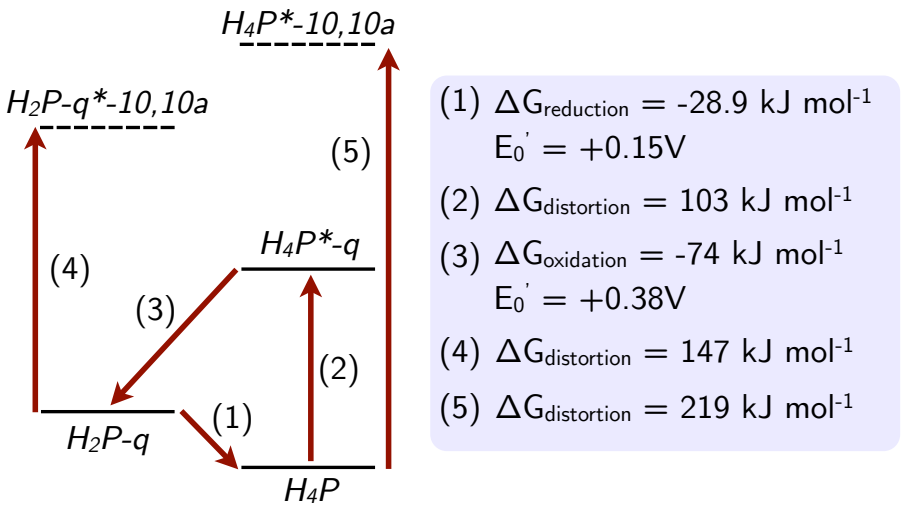

Figure 2.5: Energetics of pyranopterin distortion and redox. H_4P: DFT minimized tetrahydro, H_2P-q: DFT minimized quinonoid dihydro, H_2P-*10,10a*: DFT minimized 10,10a-dihydro, H_4P^*-q: tetrahydro at quinonoid dihydro geometry, H_4P^*-q: tetrahydro at 10,10a-dihydro geometry, H_2P-q^*-*10,10a*: quinonoid dihydro at 10,10a-dihydro geometry.

demonstrates that the distortion[5] of the tetrahydro geometry to either the quinonoid or 10,10a-dihydro geometries increases the free energy of the molecule to levels far higher than that necessary to induce an oxidation to the dihydro level. Therefore, it is strongly unlikely that the entire distortion coordinate is described by distortions of the tetrahydro.

energy cycle.

[5]Performed by changing the number of hydrogens in the dihydro geometry and then optimizing only the hydrogen atoms.

2.2 Electron transport through the pyranopterin dithiolene cofactor

As discussed in the previous section it is extremely likely that the mononuclear molybdenum enzymes possess ppd cofactors in particular oxidation states, an obvious question presents itself: what role (if any) does this oxidation state play in i) electron transport, ii) redox potential modulation, and iii) poising of the enzyme in reactive states. Here is presented a computational study in which non-equilibrium Green's function (NEGF) calculations are used to demonstrate the striking differences in electron transport behavior of the different oxidation states of the ppd cofactor. It is seen that the 10,10a-dihydro form has simple Ohmic behavior[6], while the alternative quinonoid form has greatly increased resistance and could function as an insulator. Finally, the tetrahydro form shows fascinating diode like behavior, and this behavior is explained within the context of XO family enzymes.

2.2.1 Motivation

Very little is known regarding how the ppd contributes to catalysis, but it has been postulated to serve as an electron transfer conduit to couple the active site Mo ion to other biological redox centers and as a modulator of the Mo reduction potential. Regarding the electron transfer role of the ppd, the crystal structure of xanthine dehydrogenase clearly shows that the ppd is oriented between the Mo site and a putative electron transfer chain comprised of two 2Fe2S centers and a FAD, where electrons are ultimately delivered to NAD^+. However, in most pyranopterin Mo enzymes, the role of the ppd in vectorial electron transfer is less clear. In particular, heme-containing SO family enzymes appear to facilitate electron egress to a heme

[6]Follows Ohm's law, i.e. the current is linear in applied voltage.

cofactor which docks opposite to the pyranopterin[10, 11]. This docking and heme reduction has been shown to correlation to molybdenum oxidation[12] and so it appears that in this case the pyranopterin is not important to directly facilitating electron transport.

In order to investigate the hypothesis that pyranopterin oxidation state is correlated with enzyme function[1], a detailed study of the electron transport properties of pyranopterins was undertaken. NEGF DFT calculations were used, which allow for the determination of conductance through a bridge moiety between two electrodes. These calculations were performed using ADF2013.01, and further details of the calculations may be found in Appendix B. Model systems (TH', DH', and QN', Figure 2.6) have been constructed with the ppd covalently attached to model gold electrodes via the sulfur atoms of the dithiolene fragment and a thiolate functional group on the pterin side of the molecule[7].

NEGF calculations result in the density of states (DOS) and the transmission, $\mathcal{T}(\epsilon)$ of the system in question. Of primary importance is the transmission, which is a representation of the probability of an electron successfully transporting across the junction if it contains a given energy, ϵ. The transmission is related to conductance by the *conductance quantum* g_0, $g(V) = g_0\mathcal{T}(\epsilon_F + eV)$. The calculation of transmission also enables the determination of the current-voltage (I-V) relationship of a device, through the use of the Landauer formula:

$$I = g_0 \int_{-\frac{1}{2}V_b}^{\frac{1}{2}V_b} \mathcal{T}(E + E_F)dE \tag{2.1}$$

where V_b is the bias voltage[8].

[7]In biological pterins this is an amine, however to ensure tight coupling with the gold leads sulfur was used. Amines typically show slightly greater conductivity than thiols, but the conductance spectra are not found to differ qualitatively[13].

[8]Note that this is simply the integration of the conductance over the entire range of

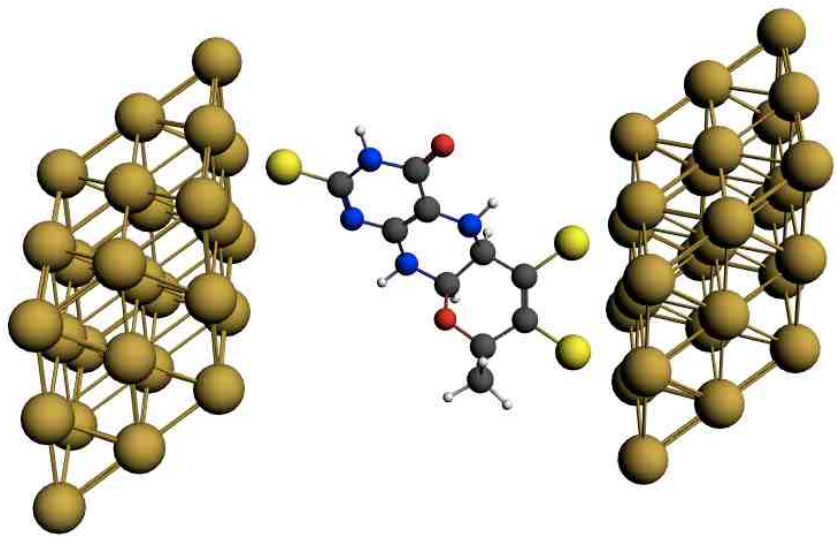

Figure 2.6: Tetrahydro pyranopterin dithiolene model system. Grey: carbon, blue: nitrogen, red: oxygen, yellow: sulfur, gold: gold, white: hydrogen.

2.2.2 Results and Analysis

The calculated transmission spectra are given in Figure 2.7 (left). The three model systems are strikingly distinct in their electron transport behavior, with DH showing markedly increased and symmetric transmission near the Fermi level. TH' ppd shows a single peak in the transmission spectrum, corresponding to a single pyranopterin π-dithiolene sulfur inplane MO (Figure 2.8). Finally, QN has damped transmission relative to DH' with a noticeable asymmetry about the Fermi level. Note that QN' and TH' have transmission peaks on opposite sides of the Fermi level, suggesting that under asymmetric bias conditions these two systems may demonstrate even more distinct electron transport behavior.

The calculated I-V curves for TH', DH', and QN' depicted in Figure 3 (right).

energies defined by the bias voltage. While not necessary, for simplicity here we assume a symmetric bias is applied.

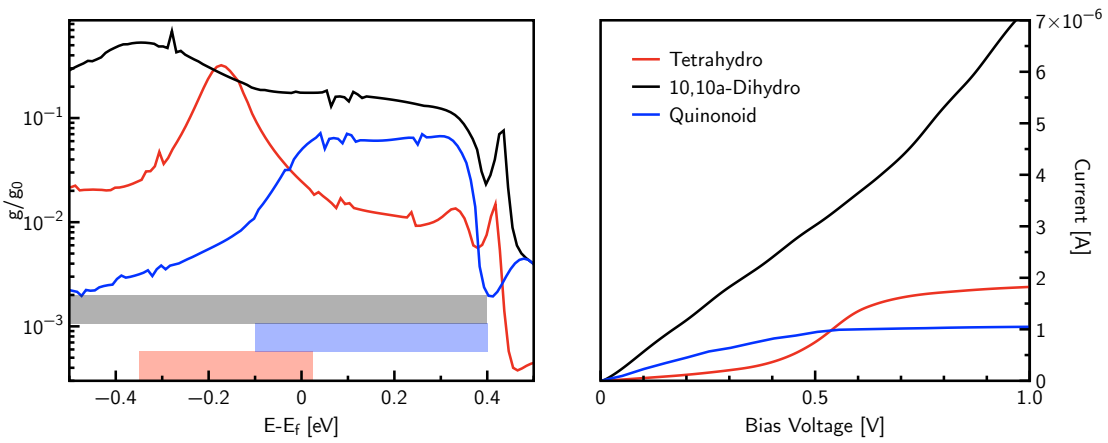

Figure 2.7: Conductance spectra (left) and current-voltage (I-V) traces (right) for the tetrahydro (red), 10,10a-dihydro (black), and quinonoid (blue) model systems.

The single peak in the transmission spectrum of TH' results in a threshold voltage for conductance in the tetrahydro system, giving an I-V curve similar to that seen for diodes. The DH' model shows Ohmic behavior, due to the high density of conducting states around the Fermi level. Finally, QN' displays Ohmic behavior at low bias, but quickly reaches a limiting current that is lower than that calculated for TH' or DH',

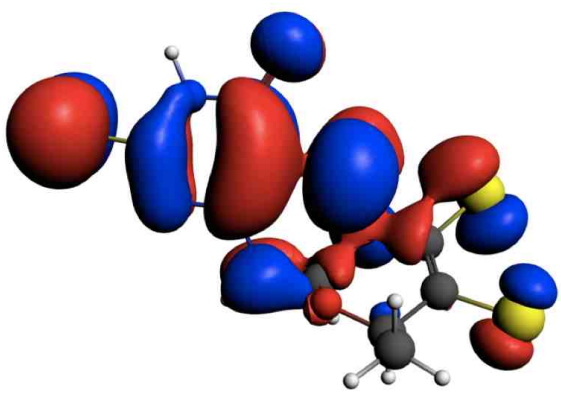

Figure 2.8: The principle conductance orbital responsible for the unique "switch" (diode) behavior of the tetrahydro pyranopterins. Note the appreciable AO character of all the electrode binding atoms.

due to a small plateau of conductance between -0.01 Eh and 0.01 Eh.

Conductance through a bridge B can be related to donor→ acceptor transfer rates ($k_{D\to A}$ through the same bridge by the use of relationships derived by Nitzan[14]. It was shown that conductance is related to k,

$$g \approx k_{D\to A}\frac{e^2}{\Gamma_D\Gamma_A F} \tag{2.2}$$

where g is the conductance, k is the electron transfer rate from D to A, Γ are factors which describe the broadening of donor and acceptor levels by the electrodes, and F is a Franck-Condon (vibrational overlap) factor. While this expression was derived for a D-B-A system placed between two electrodes, it was subsequently demonstrated[15] that this relationship holds even for an isolated bridge moiety between two electrodes. Another point worthy of mention is that in the limit of no perturbation of the bridge levels by the electrodes, Equation 2.2 is a strict equality[14]. However, even if strong perturbation is present, the ratio of the conductance of two similar bridges will result in a cancellation of the inequality terms[9].

Through the use of the Marcus equation there is a relationship between electron transfer rates and the electronic coupling matrix element:

$$k_{D\to A} = \frac{2\pi}{\hbar}\left|H_{DA}\right|^2 F \tag{2.3}$$

Using the Marcus equation (Equation 2.3) and Equation 2.2, the following expressions relating the relative rates of electron transfer at E-Ef=0 V and the transmission peak found for TH (E-Ef=-0.17 V) through the three ppd systems and the magnitudes of Hab can be obtained:

$$\frac{g_{DH}}{g_{TH}} \approx \frac{k_{DH}}{k_{TH}} = \frac{H^2_{DA,DH}}{H^2_{DA,TH}} \approx 9 \text{ (at E-Ef=0 V, 0.8 at -0.17 V)} \tag{2.4}$$

[9]This implies the assumption that there is no appreciable difference between bridge-electrode coupling in the different model systems. Due to the strong chemical similarities between the pyranopterin model systems this will be viewed as a safe assumption.

$$\frac{g_{DH}}{g_{QN}} \approx \frac{k_{DH}}{k_{QN}} = \frac{H^2_{DA,DH}}{H^2_{DA,QN}} \approx 3 \text{ (at E-Ef=0 V, 42 at -0.17 V)} \tag{2.5}$$

which shows that DH is gives approximately a 3-fold increase in H_{DA}, relative to TH and 1.7-fold increase relative to QN at zero bias, yet at -0.17 V TH shows markedly higher transmission than DH.

2.2.3 Discussion and Conclusions

Starting from the assumption that TH pyranopterins are directly involved in electron transfer[10], it is tempting to speculate as to why a threshold voltage (chemical potential difference) is desirable in these circumstances. When the potential between the Mo center and the remainder of the ET chain is below the TH threshold voltage, the Mo center is effectively "unplugged" from the rest of the electron transfer chain and ET is inhibited. This can be quite effective as a fully oxidized or reduced Mo center is particularly reactive and it would be counterproductive to facilitate unwanted ET into/out of the Mo center before substrate has a chance to react. Comparatively, DH will more effectively couple into the Mo center for electron transfer (ET), and this would suggest easier redox potential modulation through effects such as hydrogen bonding to the pyranopterin. Due to this stronger coupling, electronic communication between the Mo center and any other redox centers opposite the ppd would be greatly increased. A side effect of this would be the tendency for ET involving the Mo center, regardless of metal oxidation state and an increased difficulty in poising the active site at a particular oxidation state for catalysis, as any free endogenous redox partner would be able to bind and immediately reduce or oxidize the metal center. For some SO family enzymes this is likely not an issue, as ET is dependent upon the binding of a heme domain[11], which contrasts with XO family enzymes

[10]Per the discussion in Section 2.1.

that have a Mo center is at a fixed distance from the proximal 2Fe2S cluster.

Several experimental results are supportive of these hypotheses, namely the small range of measured Mo reduction potentials seen in XO family enzymes and a large range of potentials in SO and DMSOr family enzymes [16–21]. XO enzyme reduction potentials are typically near -350 mV (Mo VI/V) or -360 mV (Mo V/IV) with very minor deviations from this value. Conversely, SO family enzymes show potentials which vary from +38 to +2 mV for the Mo VI/V couple, and a very wide range of -6 to -239 for the V/IV couple. DMSOr family enzymes show an even wider range of potentials[22], commensurate with their broad substrate specificity, demonstrating the strong role that first coordination sphere effects have upon the metal reduction potentials. This supports the hypothesis that the reduced ppd found in XO family enzymes appears to serve as an ET conduit, but is less able to tune the reduction potential of the metal center. Conversely, the partially oxidized dihydro form effectively communicates protein effects into the metal center at any given voltage bias, potentially allowing for a wide variety of metal reduction potentials. It should be noted that the dihydro form may be quite electron withdrawing, and tend to poise the reduction potential of the Mo toward more positive potentials at parity of other effects. The extensive complexity of dihydro ppds ensures that their study will be a fertile one in the future.

Close examination of the important transmission orbitals allows for an understanding of how ppd oxidation state is closely tied to electron transport/transfer behavior. Conductance orbitals can be analyzed by examination of their atomic orbital (AO) character, as efficient electron transfer requires MOs which contain appreciable character of the AOs which are in contact with the electrodes[23]. For tetrahydro ppds, this condition holds only for a single MO near the Fermi level, shown in Figure 2.8. Conversely, the fully conjugated DH has many orbitals that possess AO character of the contact atoms, and this results in a large transmission

over a wide energy range and a corresponding increase in current for a given bias voltage. Finally, quinonoid appears be similar to the tetrahydro ligand in that it has a large transmission peak which is situated asymmetrically relative to the Fermi level.

Remarkably, the large distortion of the tetrahydro ligand (due to the saturated pyrazine-pyrano linkage and the pyran ring) appears to effectively mix in-plane sulfur orbitals with the out-of-plane pterin πsystem (Figure 2.8), allowing communication between the nominally non-conjugated dithiolene and the pterin. Communication with the ip sulfur orbitals is critical, as the Mo redox $d_{x^2-y^2}$ orbital is also oriented in-plane, and this orbital interaction is known to be crucial for effective Mo-dithiolene communication[24]. Therefore, this ppd distortion may provide a means of electron transport tuning, to the degree that the protein scaffold is able to affect ppd distortions. The quinonoid dihydro is highly distorted, even when compared to the tetrahydro form. This results in extensive mixing of ip dithiolene and oop pterin orbitals. However, for the more oxidized quinonoid form, the pterin orbital that is mixing with the dithiolene is unoccupied, and so the resultant conductance orbital appears on the high energy side of the fermi level. The electron withdrawing nature of the quinoinoid also reduces the dithiolene sulfur character in the orbital, slightly reducing the maximum conductance when compared to the tetrahydro form (Figure 2.7).

In summary, DFT-NEGF transport calculations show that reduced and partially oxidized pyranopterin dithiolenes have remarkably distinct electron transport behavior. This study, coupled with recent work[1] strongly suggests a relationship between pyranopterin oxidation state which is intimately linked with electron transport behavior and enzyme function. Interestingly, the three types of ppds explored give a wide variety of electron transport behavior that includes diode like tetrahydro, a conductive 10,10a-dihydro, and finally weakly conductive/current limiting quinonoid

form. The degree of mixing between the out-of-plane pyranopterin π system and the in-plane dithiolene is modulated by out-of-plane distortions facilitated by the pyran ring, and these appear to be of crucial importance in tuning transport and electron transfer behavior.

2.3 References

(1) Rothery, R. A.; Stein, B.; Solomonson, M.; Kirk, M. L.; Weiner, J. H. *Proc. Natl. Acad. Sci. U.S.A.* **2012**, *109*, 14773–14778, DOI: 10.1073/pnas.1200671109.

(2) Kloer, D. P.; Hagel, C.; Heider, J.; Schulz, G. E. *Structure* **2006**, *14*, 1377–1388, DOI: 10.1016/j.str.2006.07.001.

(3) Bertero, M. G.; Rothery, R. A.; Palak, M.; Hou, C.; Lim, D.; Blasco, F.; Weiner, J. H.; Strynadka, N. C. J. *Nat. Struct. Biol.* **2003**, *10*, 681–687, DOI: 10.1038/nsb969.

(4) Greatbanks, S. P.; Hillier, I. H.; Garner, C. D.; Joule, J. A. *J. Chem. Soc. Perkin Trans. 2* **1997**, *1997*, 1529–1534, DOI: 10.1039/A700330G.

(5) Karber, L. G.; Dryhurst, G. *J. Electroanal. Chem. Interfacial Electrochem.* **1982**, *136*, 271–289.

(6) Karber, L. G.; Dryhurst, G. *J. Electroanal. Chem. Interfacial Electrochem.* **1984**, *160*, 141–157.

(7) Hille, R.; Hall, J.; Basu, P. *Chem. Rev.* **2014**, *114*, 3963–4038, DOI: 10.1021/cr400443z.

(8) Romão, M. J. *Dalton Trans.* **2009**, 4053–4068, DOI: 10.1039/b821108f.

(9) Dobbek, H. *Coord. Chem. Rev.* **2011**, *255*, 1104–1116, DOI: 10.1016/j.ccr.2010.11.017.

(10) Emesh, S.; Rapson, T. D.; Rajapakshe, A.; Kappler, U.; Bernhardt, P. V.; Tollin, G.; Enemark, J. H. *Biochemistry* **2009**, *48*, 2156–2163, DOI: 10.1021/bi801553q.

(11) Feng, C.; Tollin, G.; Enemark, J. H. *Biochim. Biophys. Acta BBA-Proteins Proteomics* **2007**, *1774*, 527–539, DOI: 10.1016/j.bbapap.2007.03.006.

(12) Johnson-Winters, K.; Tollin, G.; Enemark, J. H. *Biochemistry* **2010**, *49*, 7242–7254l, DOI: 10.1021/bi1008485.

(13) Kim, G.; Wang, S.; Lu, W.; Nardelli, M. B.; Bernholc, J. *J. Chem. Phys.* **2008**, *128*, 024708, DOI: 10.1063/1.2822180.

(14) Nitzan, A. *J. Phys. Chem. A* **2001**, *105*, 2677–2679, DOI: 10.1021/jp003884h.

(15) Ricks, A. B.; Solomon, G. C.; Colvin, M. T.; Scott, A. M.; Chen, K.; Ratner, M. A.; Wasielewski, M. R. *J. Am. Chem. Soc.* **2010**, *132*, 15427–15434, DOI: 10.1021/ja107420a.

(16) Hille, R. *Chem. Rev.* **1996**, *96*, 2757–2816.

(17) Kalimuthu, P.; Leimkühler, S.; Bernhardt, P. V. *J. Phys. Chem. B* **2012**, *116*, 11600–11607, DOI: 10.1021/jp307374z.

(18) Kalimuthu, P.; Fischer-Schrader, K.; Schwarz, G.; Bernhardt, P. V. *J. Phys. Chem. B* **2013**, *117*, 7569–7577, DOI: 10.1021/jp404076w.

(19) Chen, K. I.; McEwan, A. G.; Bernhardt, P. V. *J. Biol. Inorg. Chem.* **2009**, *14*, 409–419.

(20) Aguey-Zinsou, K. F.; Bernhardt, P. V.; McEwan, A. G.; Ridge, J. P. *J. Biol. Inorg. Chem.* **2002**, *7*, 879–883, DOI: 10.1007/s00775-002-0374-y.

(21) Aguey-Zinsou, K.-F.; Bernhardt, P. V.; Kappler, U.; McEwan, A. G. *J. Am. Chem. Soc.* **2003**, *125*, 530–535, DOI: 10.1021/ja028293e.

(22) Creevey, N. L.; McEwan, A. G.; Hanson, G. R.; Bernhardt, P. V. *Biochemistry* **2008**, *47*, 3770–3776, DOI: 10.1021/bi702444r.

(23) Tsuji, Y.; Staykov, A.; Yoshizawa, K. *J. Am. Chem. Soc.* **2011**, *133*, 5955–5965, DOI: 10.1021/ja111021e.

(24) Inscore, F. E.; McNaughton, R. L.; Westcott, B. L.; Helton, M. E.; Jones, R.; Dhawan, I. K.; Enemark, J. H.; Kirk, M. L. *Inorg. Chem.* **1999**, *38*, 1401–1410.

Chapter 3

Jahn-Teller Effects in Model Systems

It has been well established that transition metal dithiolene complexes possess a strong relationship among a) metal-ligand fold angle, b) metal oxidation state, and c) metal-ligand covalency. Here is presented a complete spectroscopic and computational study on a series of Cp_2M^{II}(benzenedithiolato) complexes, where M=Ti (d^0), V (d^1), and Mo (d^2). rR, MCD, electronic absorption, and EPR spectroscopies are used in conjunction with multiple advanced computational techniques to form a complete understanding of the electronic structure of these compounds. This is understood within the context of a pseudo-Jahn-Teller model to describe how 1-electron changes in oxidation state result in extremely large swings in vibronic coupling behaviors.

3.1 Jahn-Teller Effects in Transition Metal Dithiolenes

The Jahn-Teller effect was first described in 1937 by Jahn and Teller[1], and describes how a molecule containing an orbital degeneracy cannot be stable to distortions which remove that degeneracy. This was exhaustively proven by a perturbation theory analysis of all of the degenerate representations of the varied point groups, which showed that it is the vibrational-electronic (vibronic) interaction which results in a lowering of the electronic energy. This section will briefly layout the fundamentals of vibronic coupling the related (pseudo) Jahn-Teller effect to a degree necessary that the reader will be able to easily follow the remainder of this chapter. For a further discussion, there are several excellent texts by Bersuker[2, 3] and other related publications[4, 5].

Here we frame the discussion of the dithiolene fold in $Cp_2M(bdt)$ compounds in the pseudo Jahn-Teller (PJT) formalism. The PJT effect relates to the vibronic mixing of non-degenerate states, in a manner analogous to the proper JT effect. The PJT does not, however, require the states to be strictly degenerate and and so is operative even in point groups without any degenerate representations. The magnitude of the PJT effect can be quantified with a vibronic constant:

$$F_{0i}^{\Gamma} = \left\langle \Psi_0 \left| \frac{\delta V}{\delta Q_{\Gamma}} \right| \Psi_i \right\rangle \tag{3.1}$$

where Ψ are the state labels and Q_{Γ} is a vibrational mode of symmetry Γ.

This mechanism is operative even for states which are forbidden by symmetry to mix by a configuration interaction mechanism, and so provides a way for orbitals of different symmetry to mix, giving an overall lower point group. In order for a PJT to be observed the triple product $\Gamma_0 \times \Gamma_Q \times \Gamma_i$ must contain the totally symmetric representation for at least one state Ψ_i. In addition, the energy between the ground

state Ψ_0 and Ψ_i must be small enough for effective coupling. A simple two state, one mode vibronic Hamiltonian can be diagonalized to give an explicit expression for the PJT adiabatic potential energy surface (APES):

$$\epsilon_{\pm} = {}^1\!/_2 K_0 Q^2 \pm \sqrt{\Delta^2 + F^2 Q^2} \tag{3.2}$$

where K_0 is the primary (non-vibronic) force constant, Δ is $^1\!/_2$ of the energy gap between the mixing states, and Q is a dimensionless normal mode mode coordinate. At a certain threshold ($\Delta > F^2/K_0$), the molecule will become unstable w.r.t. a distortion along Q and will distort to a lower point group. Equation 3.2 shows that there are 3 parameters which result in a large PJT stabilization: 1) small Δ, 2) small K_0, and 3) large F. These requirements are easily understood, as a large F/$\Delta$is the typically requirement of perturbational mixing of two states, and a small K_0 results in a low barrier to distorting along the particular Q.

3.2 Cp_2M(benzenedithiolato) complexes as models of the Jahn-Teller effect in molybdenum dithiolene active sites

3.2.1 Synthesis and previous studies of Cp_2M(bdt) complexes

Synthesis

Cp_2MoCl_2 (Alfa Aesar), Cp_2VCl_2, Cp_2TiCl_2 (Aldrich) were purchased and used without further purification. 1,2-benzenedithiol was synthesized following a published procedure[6]. Synthesis of the compounds Cp_2M(bdt) (M= Mo, Ti, V) was carried out as previously described in the literature[7, 8] using standard Schlenk techniques.

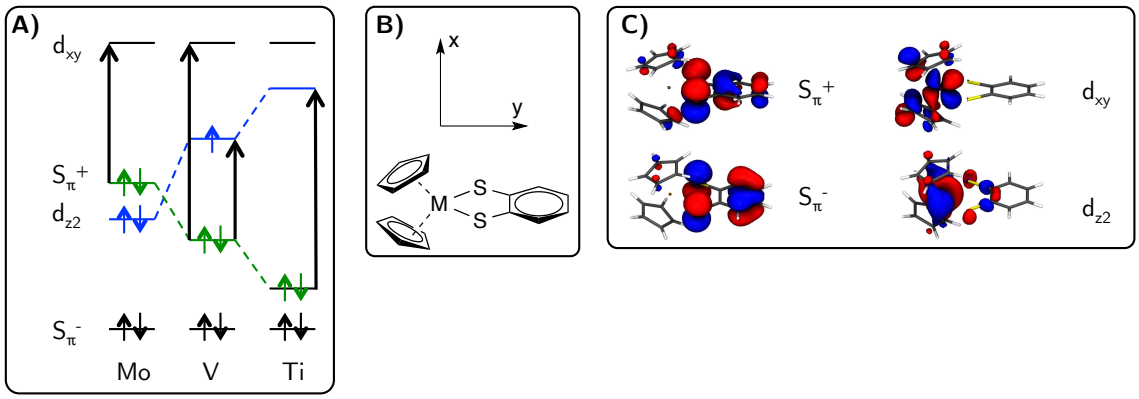

Figure 3.1: Frontier MOs of Cp_2M(benzenedithiolato). A) Frontier MOs of M=Mo (**1**),V (**2**), and Ti (**3**), arrows represent important electronic transitions studied here (*vide infra*), B) coordinate system definition, C_s symmetry convention, C) isosurface plots of frontier MOs (M=Mo).

Electronic Absorption Spectroscopy

Solution electronic absorption spectra were collected using a double beam Hitachi U-3501 UV-vis-NIR spectrophotometer capable of scanning a wavelength region between 185 and 3200 nm. All absorption spectra were collected at 2.0 nm slit width. The instrument was calibrated with reference to the 656.10 nm deuterium line. Solution samples were prepared by dissolving the compounds in degassed dichloromethane (M=Mo,Ti) or 2-methyltetrahydrofuran (M=V). The electronic absorption spectra were subsequently collected in 1 cm pathlength quartz cells (blackmasked Suprasil II, equipped with a Teflon lined screw cap). Gaussian resolution of spectral bands were accomplished with the *Magicplot* software package.

Resonance Raman

RR spectra were collected in a 180° (780 nm) or 90° (all other lines) geometry. Coherent Innova (5W) Ar+ (457.9-528.7 nm, 9 discrete lines) and 300°C Kr+ (406.7-

676.4 nm, six discrete lines) ion lasers were used as the photon sources. The scattered radiation was dispersed onto a liquid N_2 cooled 1" Infrared Associates CCD detector using a Princeton Acton spectrograph. The laser power at the sample was kept between 40 and 100 mW in order to prevent possible photo- and thermal degradation of the sample. 780nm Raman spectra were collected with a Thermo-Scientific DXR SmartRaman, with a 2 mW laser power due to the observed sensitivity of $Cp_2V(bdt)$ to photodegradation. Solid samples were prepared as finely ground powders and dispersed in a NaCl(s) matrix with Na_2SO_4 added as an internal standard. These samples were subsequently sealed in a glass capillary tube and Raman spectra were obtained by spinning the sample in a custom sample holder/spinner or standard brass holder with the sample applied to carbon tape (780 nm). The construction of resonance Raman profiles was accomplished by comparing the integrated intensity of a Raman band at a given excitation wavelength relative to that of the 992.4 cm^{-1} band of Na_2SO_4. All data were scan averaged, and any individual data set with vibrational bands compromised by cosmic events was discarded.

Magnetic Circular Dichroism Spectroscopy

Low-temperature MCD data were collected on a system consisting of a Jasco J-810 CD spectropolarimeter employing Hamamatsu photomultiplier tubes of either S-1 or S-20 response, an Oxford Instruments SM4000-7T superconducting magneto-optical cryostat (0-7 Tesla and 1.4-300 K), and an Oxford Instruments ITC503 temperature controller. The spectrometer was calibrated for CD intensity and wavelength using camphorsulfonic acid and a Nd-doped reference glass sample (Schott Glass). MCD samples were prepared as frozen 2-methyltetrahydrofuran (Alfa Aesar, purified by passage down a column of activated alumina followed by freeze-pump-thaw degassing) solutions. Depolarization of the incident radiation was checked by comparing the difference in CD intensity of a standard Ni (+)-tartrate solution positioned

before and then after the sample. Samples which depolarized the light by <5% were deemed suitable. All MCD spectra were collected in an applied magnetic field of 7 Tesla.

Calculations

RR calculations were performed with the advanced spectral analysis (ASA) package of ORCA 3.0.0[9, 10]. Geometry optimizations and frequency calculations used the def2-TZVPP[11] basis set and the PBE[12] functional. TD-DFT spectra and excited state gradients used in the calculation of resonance Raman spectra were calculated with the PBE0 hybrid functional[13] (M=Mo, Ti) and the RIJCOSX[14] approximation or the PBE GGA functional (M=V). TD-DFT calculations of MCD spectra were done with ADF 2012.01[15, 16] using a triple-ζ STO basis (TZP) and the PBE functional. Electron density difference maps (EDDMs) were created with the orca_plot utility.

3.2.2 Results and analysis

Here is presented a detailed analysis of spectroscopic and computational studies performed on $(Cp)_2Mo(bdt)$ (**1**), $(Cp)_2V(bdt)$ (**2**), and $(Cp)_2Ti(bdt)$ (**3**), with a specific focus on the relatively small frontier orbital bases shown in Figure 3.1 and the DFT frontier MOs for **1-3** are depicted in Figures 3.4, 3.8, and 3.11, respectively. The spectroscopic results are analyzed in the context of DFT calculations to develop a pseudo-Jahn-Teller (PJT) description of folding in metallodithiolenes and to understand how the interplay between electronic and geometric structure uniquely poises the d^1 configuration for tunable facile electron transfer processes like those found in the Mo(V) state of pyranopterin molybdenum enzymes.

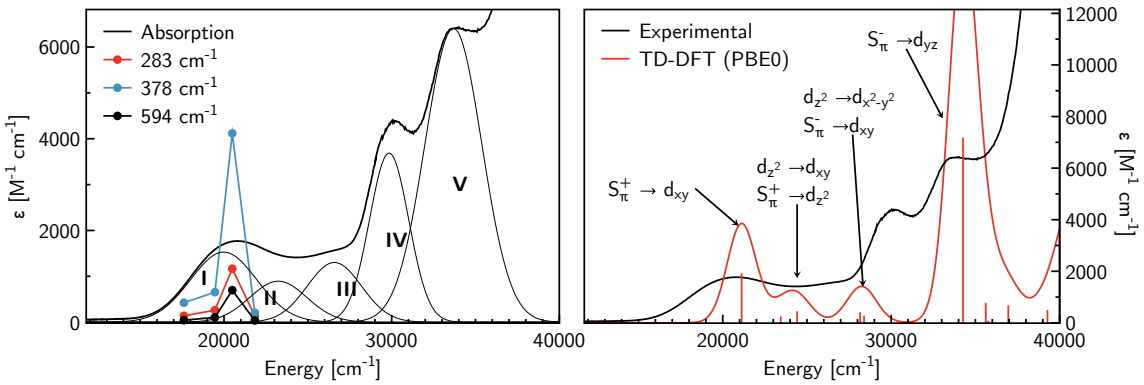

Figure 3.2: Absorption and rR spectroscopy of Cp_2Mo(benzenedithiolato). Left: rR profiles and gaussian resolved absorption spectrum, right: TD-DFT (PBE0) calculated spectrum.

$Cp_2Mo(bdt)$ (1)

The solution electronic absorption spectrum and rR profiles of **1** are shown in Figure 3.2. Compound **1** displays a single absorption feature at low-energy that is well isolated from higher energy excitations with strong relative resonance enhancement of the 378 cm^{-1} vibration. The frontier orbital description detailed in Figure 3.1 suggests two possible low-energy excitations. The first is a low energy ligand-to-metal charge transfer (LMCT) transition from the doubly occupied S_π^+ orbital to the vacant d_{xy}. The second is a formally ligand field (LF) transition described as a one-electron promotion from the double occupied $d_{x^2-y^2}$ orbital to d_{xy}. Clearly the LMCT transition is anticipated to possess much greater oscillator strength than the LF transition which allows for the assignment of the 21,000 cm^{-1} band a the $S_\pi^+ \rightarrow d_{xy}$ LMCT transition. The LF band is likely obscured by the CT absorption envelope at higher energy, disallowing for the direct assignment in the electronic absorption spectrum. TD-DFT results (Figure 3.2 and Table 3.1) are in excellent agreement with experimental data, allowing a confident assignment of other absorption bands.

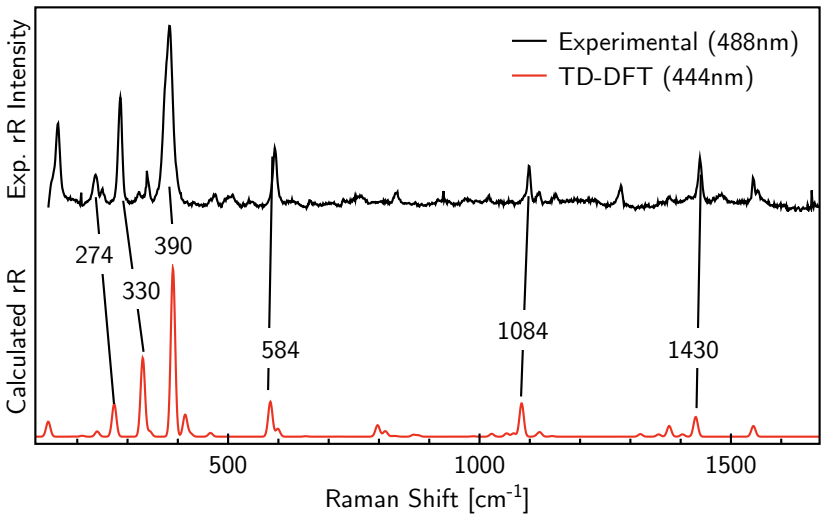

Figure 3.3: Resonance Raman of $Cp_2Mo(bdt)$. The experimental and calculated spectra are both on resonance with band I (Figure 3.2).

In particular, Band IV appears to contain the $S_\pi^- \rightarrow d_{xy}$ LMCT band, which is the anti-symmetric counterpart to Band I.

The calculated electron density difference map (EDDM) for the $S_\pi^+ \rightarrow d_{xy}$ transition and the S_π^+ and d_{xy} orbitals involved in the one-electron promotion are given in Figure 3.4. In the effective C_{2v} geometry of 1 with a non-bent Mo-dithiolene geometry the filled S_π^+ orbital (b_1 symmetry) and the filled Mo d_{z^2} orbital (a_1 symmetry) do not have the same symmetry and therefore do not mix, and vibronic interactions

	Energy [cm^{-1}]		$f \times 10^3$		
Band	exp.	calc.	exp.	calc.	Assignment
I	20614	21121	41	35	$S_\pi^+ \rightarrow d_{xy}$
II/III	26402	23439/24416	36	5/8	$d_{z^2} \rightarrow d_{xy}/S_\pi^+ \rightarrow d_{x^2-y^2}$
IV	29874	28152/28390	42	8/5	$d_{z^2} \rightarrow d_{x^2-y^2}/S_\pi^- \rightarrow d_{xy}$
V	33690	34265	120	130	$S_\pi^- \rightarrow d_{yz}$

Table 3.1: $Cp_2Mo(bdt)$ absorption data.

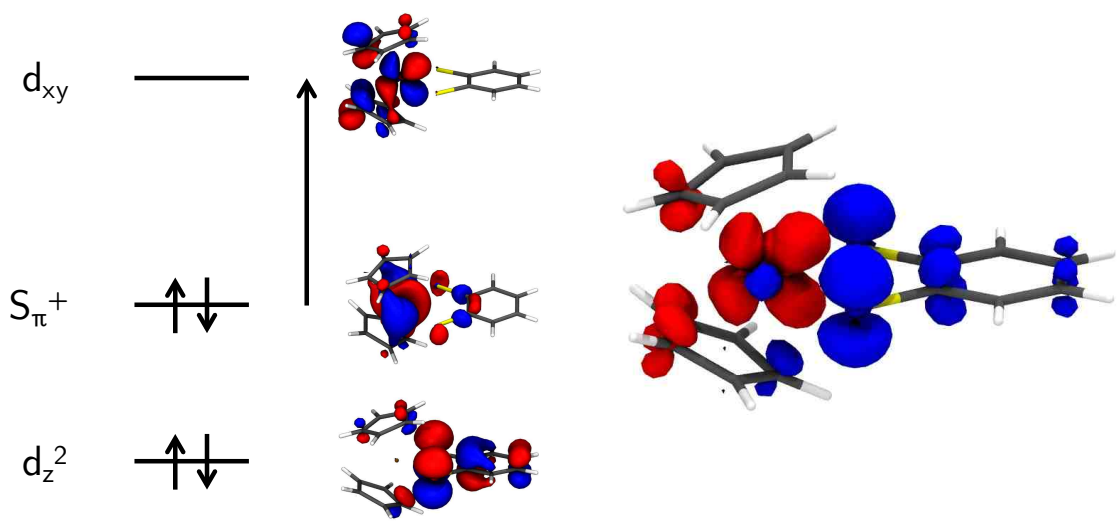

Figure 3.4: TD-DFT results for $Cp_2Mo(bdt)$. Left: orbital description of transition, right: EDDM, blue=electron loss and red=electron gain.

are unable to mix these two orbitals due to both being doubly occupied (Section 3.2.3). The Mo d_{xy} LUMO is strongly antibonding with respect to the two Cp rings and therefore the $S_\pi^+ \rightarrow d_{xy}$ LMCT transition is expected result in a large excited state distortion along the totally symmetric Cp-Mo-Cp stretching coordinate with a markedly less pronounced excited state distortion along the totally symmetric S-Mo-S coordinate.

The experimental and computed resonance Raman (rR) spectra for **1** are presented in Figure 3.3, where it can be seen that the most intense feature is the 378 cm^{-1} vibration. Resonance Raman spectroscopy, through the analysis of Raman profiles and relative enhancement of vibrational modes under resonance conditions, provides an extremely powerful probe for identifying the nature of the CT excited state by detailing how the excited state geometry is distorted relative to the ground state geometry[9, 17]. Typically, the most accurate method for assigning vibrational bands is to perform an isotopic substitution study but this is often impractical due

Frequency (cm^{-1})		Intensity		
Exp.	Calc.	Exp.	Calc.	Mode description
Not obs.	28	-	0.04	Dithiolene fold
236	274	0.2	0.2	M-Cp str. (s) + C-S ip bend
286	330	0.61	0.47	M-Cp str. (as) + C-S ip bend
383	390	1	1	Cp-M-Cp str. (s)
593	584	0.34	0.21	M-Cp str. (single Cp)
1098	1084	0.25	0.2	C-S str. + C-C str.
1438	1430	0.29	0.11	Ph ring mode

Table 3.2: $Cp_2Mo(bdt)$ vibrational modes.

to the inherent difficulties associated with the synthesis of the molecules of interest and the cost of the isotopes. Here, we have used a combination of experimental and computed Raman spectra obtained under resonance conditions to analyze the resonance enhancement patterns of the vibrational modes and make detailed assignments of the vibrational spectra of compound **1**. Several Raman vibrations show strong resonance enhancement, namely vibrational bands at 1438 $^{-1}$, 1098 $^{-1}$, 593 $^{-1}$, 384 $^{-1}$, 286 $^{-1}$, and 238 $^{-1}$. These modes have been assigned (Table 3.2) on the basis of their frequencies as calculated by DFT and by their remarkably similar relative resonance enhancements compared with experiment.

Analysis of the TD-DFT derived resonance Raman spectrum shows that most intense Raman vibration is the 383 cm^{-1} mode, which is assigned as the totally symmetric Cp-Mo-Cp stretch. This confirms the assignment of the 20,000 cm^{-1} band in the electronic absorption spectrum as the $S_{\pi}^{+} \rightarrow d_{xy}$ LMCT transition with a large excited state distortion along the totally symmetric Cp-Mo-Cp relative to the ground state. The absence of a resonantly enhanced totally symmetric S-Mo-S stretch, further supports the molecular orbital description of orthogonal S_{π}^{+} and Mo d_{z^2} molecular orbitals in **1**. Thus, neither the ground state of **1** nor the LMCT excited state (Figure 3.4) should exhibit an appreciable fold angle of the Mo-dithiolene chelate

ring.

photoelectron spectroscopy (PES) is a technique which is used to probe the energies of molecular orbitals by relating the ionization energies of molecules to the energy of the orbital from which the electron originated (Koopman's theorem). Within the more accurate state picture, the ionization process can be viewed as an electronic transition from the ground state of a neutral molecule to a cationic state and an electron. As such, the profile of the ionization band is a sampling of the vibrational structure of the cation that results from the removal of a specific electron. If the energy of the vibration is large enough, the individual energy levels can be resolved in the photoelectron spectrum. This observation can provide a wealth of information, including the energy of the vibration and the energy of vibrational reorganization, λ_v, associated with the loss of an electron from that orbital. The advantage of finding λ_v with gas-phase photoelectron spectroscopy is the absence of contributions from solvation. Vibrational structure has been observed in the first ionization band of Cp2Mo(bdt) which has previously been assigned as predominantly S_π^+ in character[8].

Frequency (cm^{-1})	$\|\Delta\|$	S_b
71	0.23	0.03
96	0.25	0.03
198	1.4	0.98
258	2.7	3.6
312	1.3	0.84
471	1.0	0.5
1090	0.52	0.14

Table 3.3: $Cp_2V(bdt)$ rR fitting results used int the calculation of the missing mode observed in the PES of $Cp_2Mo(bdt)$.

While the rR of **1** shows a vibrational mode at 383 cm^{-1}, this is a ground state vibrational mode of the neutral species, not the cationic form probed in PES. Fur-

thermore, this mode has been assigned as a M-Cp stretch (Table 3.2, which should not be the most distorted mode in a S_π^+ based ionization, rather M-S/C-S modes are expected to predominate. To model and understand what vibration (or combination of vibrations) could be responsible for the structure seen in the ionization envelope of the S_π^+, we have used the rR spectrum obtained for **2** as a model of the vibrational modes which are activated during the photoionization process. The rR of **2** is on resonance with a transition which involves redistribution of electron density among the S_π^+ and d_{z^2} orbitals, which should induce a distortion similar to that seen in the photoionization of **1**. Conversely, the transition probed in the rR of **1** involves a transition to the strongly M-Cp antibonding d_{xy} orbital, and should therefore be dominated by the Cp-M-Cp stretch. Fitting of the experimental rR spectrum[9] of **2** gives a set of excited state displacements (Table 3.3) which can be used to determine the frequency of the missing mode (MIME[18]) seen in the PES spectrum. The MIME is described by the following equation which has been derived for the missing mode:

$$\omega_{eff} = \frac{\sum_k (\omega_k^2 \Delta_k^2) + 4\Gamma^2}{\sum_k \omega_k \Delta_k^2 n_k} \tag{3.3}$$

where ω are the vibrational modes, Δ are the dimensionless displacements, n_k is related to the ratio between the mode k and the missing mode, and Γ is an broadening factor (usually 100-150 cm^{-1}). This equation should be solved iteratively, using an initial guess for the MIME frequency and updating the n_k values each cycle until self-consistency is reached (Appendix E). The use of Equation 3.3 with the results in Table 3.3 gives an ω_{eff} of 323 cm^{-1}, which is in reasonable agreement considering the approximations made.

As an additional check of this hypothesis, we have performed frequency calculations on both the neutral and cationic versions of $Cp_2Mo(bdt)$. Since the ionized electron originates from an orbital with dominant sulfur character, vibrational modes that alter the bonding/anti-bonding interactions of S_π^+ are the main focus. Deter-

Frequency (cm^{-1})	$\|\Delta\|$	S_b	Description
311	1.9	1.9	Cp-M symm. stretch + S-Mo-S bend
332	2.5	3.0	Cp-M asymm. stretch
474	6.8	23	C-S stretch

Table 3.4: Calculated displacements of $Cp_2Mo(bdt)$ ionization. While all modes were included in the missing mode calculation, only the largest three displaced modes are shown here.

mination of the modes which contribute to the observed vibrational progression was accomplished by the projection of Cartesian displacement differences between the calculated geometries of the neutral and cationic forms of **1** into dimensionless normal coordinates (Table 3.4)[1]. Interestingly, this appears to be an excellent example of a MIME, as no mode near the observed frequency is displaced. However, three modes near the experimental value were found to have sizeable displacements (Table 3.4) and the use of Equation 3.3 results in an effective frequency of 394 cm^{-1}, which is in excellent agreement with the experimental value of 383 $\pm$ 65 cm^{-1}. The strongly distorted higher energy vibration (474 cm^{-1} calculated) consists primarily of C-S stretch character as expected for a S_π^+ ionization. The lower frequency modes (311 cm^{-1} and 332 cm^{-1} calculated), however, have appreciable Mo-Cp stretch which demonstrates the role of electronic relaxation in the ionization process. Upon ionization of the S_π^+ orbital, a pseudo Jahn-Teller effect is immediately operable (*vide infra*) and which mixes the d_{z^2} orbital with the S_π^+ and the appreciable amount of Mo-Cp pseudo $\sigma*$ character in the d_{z^2} orbital neatly explains this Mo-Cp distortion.

[1]Dimensionless normal coordinates are defined as $\Delta = \sqrt{\frac{\omega}{\hbar}}\mathbf{LqM}^{1/2}$, where ω is the angular frequency, $\mathbf{L}$ is the normal mode matrix, $\mathbf{q}$ are the displacements in cartesian coordinates, and $\mathbf{M}$ is a vector of atomic masses. The Huang-Rhys factor is defined as $S = \Delta^2/2$.

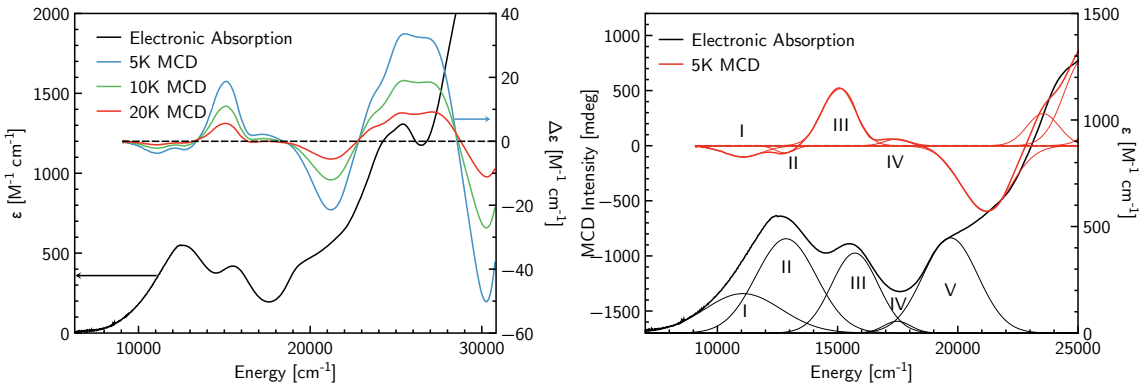

Figure 3.5: Electronic absorption and MCD spectroscopy of $Cp_2V(bdt)$. Solvent: 2-methyltetrahydrofuran, B=7T.

$Cp_2V(bdt)$

The electronic absorption spectrum of **2** (Figure 3.5) shows a similar overall absorption envelope as **1**, but with a distinct redshift. A slight low energy tail is observed, but individual transitions are not resolved with room temperature absorption spectra. These transitions are resolved through the use of low temperature

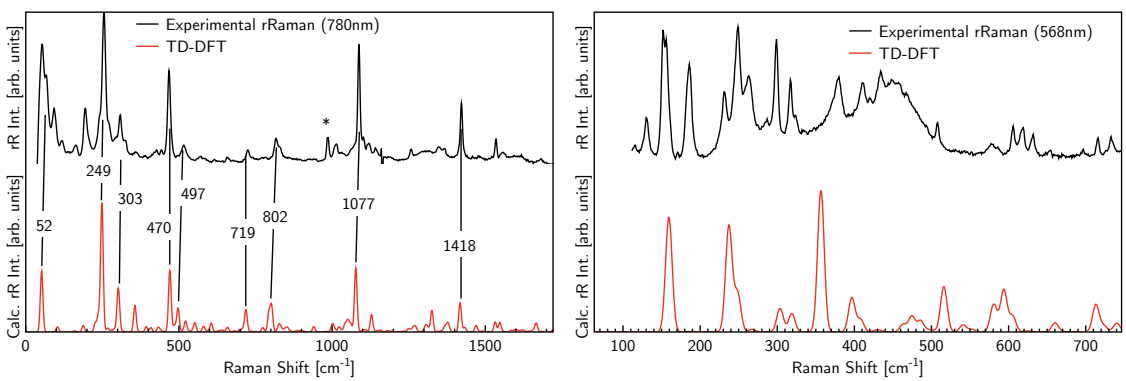

Figure 3.6: Resonance Raman of $Cp_2V(bdt)$. On resonance with left: band II, right: band III. Asterisks denote internal standard (Na_2SO_4) modes.

frozen solution MCD spectroscopy of **2** clearly shows the presence of two low energy bands within the absorption envelope. This is of particular interest as the simple MO model (Figure 3.1) predicts several possible CT transitions that are likely of comparable energy: $S_\pi^+ \rightarrow d_{xy}$, $S_\pi^+ \rightarrow d_{z^2}$, or $d_{z^2} \rightarrow d_{xy}$. Band II is assigned as a $S_\pi^+ \rightarrow d_{z^2}$ transition due to the higher absorption intensity expected for a transition between two mixed orbitals. This mixing is made allowed by the distortion observed in **2**, driven by the removal of one electron from the metal-based redox orbital of **1**. Band I is therefore assignable as $d_{z^2} \rightarrow d_{xy}$ or $S_\pi^+ \rightarrow d_{xy}$. Both transitions are expected to have reasonable oscillator strength, but the second is expected to arise at an energy of at least 25,000 cm^{-1}, where the same transisiton is found in **1**. Mixing of the S_π^+ and d_{z^2} orbitals should only raise this transition to an even higher energy. Therefore, this transition is assigned as the $d_{z^2} \rightarrow d_{xy}$ The lack of oscillator strength can be explained by an intensity borrowing effect in which the CI mixing of two excited configurations results in a reduction in absorption intensity of one state and the strengthing of the other. Further confidence in this assignment is provided by the calculated MCD and absorption spectra of **2**, which are in good agreement with experimental results (Figure 3.7). The TD-DFT results give assignments as shown in Table 3.5. The intensity borrowing alluded to earlier is supported by the TD-DFT calculations which show a mixing between the $d_{z^2} \rightarrow d_{xy}$ and $S_\pi^+ \rightarrow d_{z^2}$ one-electron promotions, but the lower energy one has a cancellation of dipoles.

The rR spectrum of **2** shows a marked increase in the number of enhanced modes as compared to **1**. This suggests either a notable reduction in symmetry of the molecule and/or a distinct difference in the nature of the electronic transition. The former does not appear to substantially affect the rR enhancement, as a change in geometry does cause a shift in the rR profile maximum[2] but not in the enhancement

[2]rR profiles of **1** in the solid state show a rR enhancement maximum apparently off resonance. However, the low frequency dithiolene fold is likely easy to be distorted by solid-state packing effects and so the absorption band shifts in the solid-state.

	Energy [cm^{-1}]			$f \times 10^3$		
Band	exp. (Abs/MCD)	calc.	Sign	exp.	calc.	Assignment
I	10713/11063	9586	(-)	2.4	1.6	$d_{z^2} - S_\pi^+ \rightarrow d_{xy}$
II	12804/12804	11309	(-)	6.8	20	$S_\pi^+ + d_{z^2} \rightarrow d_{z^2} - S_\pi^+$
III	15726/15049	13097/13580	(+)	3.9	1/2	$d_{z^2} - S_\pi^+ \rightarrow d_{yz}/S_\pi^- \rightarrow d_{z^2} - S_\pi^+$
IV	17467/17472	15800	(+)	0.4	3	$S_\pi^+ + d_{z^2} \rightarrow d_{xy}$
V	25274/25256	-	(-)	33	-	$S_\pi^- \rightarrow d_{xy}$ (tent.)

Table 3.5: $Cp_2V(bdt)$ absorption data.

pattern. Based upon the aforementioned band assignments the dominant transition is of different character in **2**, and so a different enhancement pattern is expected. The S_π^+ to d_{z^2} is expected to show stronger enhancement of M-S modes, due to the increased M-S bonding character in both the HOMO and SOMO.

Frequency (cm^{-1})		Intensity		
Exp.	Calc.	Exp.	Calc.	Mode description
64	52	0.79	0.47	Dithiolene fold
266	249	1	1	M-Cp str. (s) + dt fold
319	300	0.32	0.17	52 + 249 combination
	304		0.19	M-Cp str. (s) + S-M-S ip bend
478	470	0.61	0.46	C-S str. (s) + ring str.
526	497	0.12	0.18	249 overtone
735	719	0.09	0.17	249 + 470 combination
828	794	0.16	0.14	Cp-H wag
833	802		0.20	Cp-H wag
1092	1077	0.79	0.48	C-S + C-C str.
1432	1418	0.40	0.21	Ph ring mode

Table 3.6: $Cp_2V(bdt)$ vibrational modes.

Important modes include the low energy dithiolene fold (experimental: 71 cm^{-1}, calculated: 52 cm^{-1}), central to the role that dithiolene bending plays in modulating

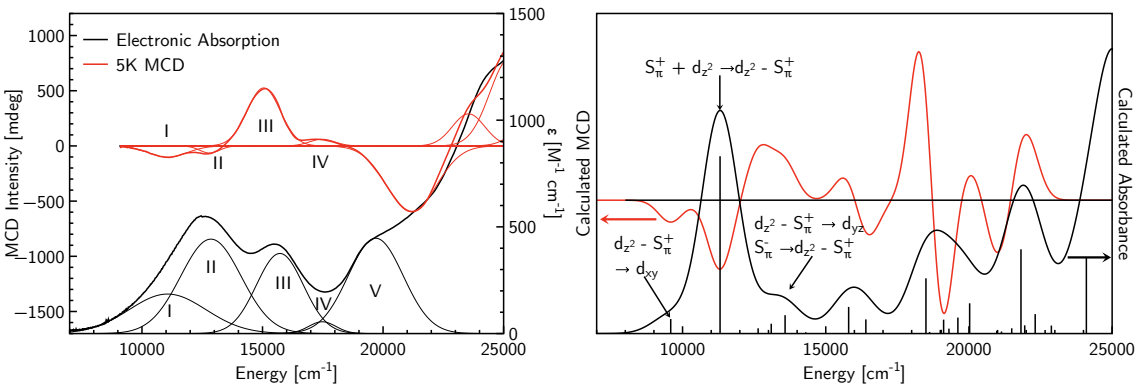

Figure 3.7: Cp_2V(benzenedithiolato) TD-DFT MCD spectrum. Left: experimental, right: TD-DFT (ADF, PBE/TZP).

metal-sulfur covalency through a pseudo Jahn-Teller effect (*vide infra*). Only a few modes appear to be in common with those seen enhanced in **1**, however, the degree of M-Cp stretch character is reduced and dithiolene fold character is increased. Several C-S/M-S stretch and S-M-S bend modes are enhanced, probing the changes in M-

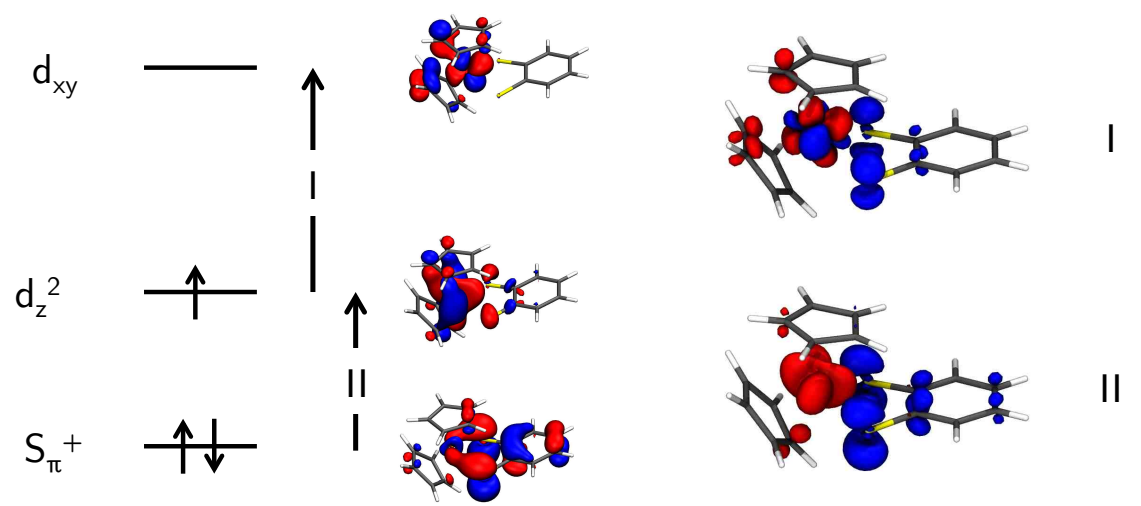

Figure 3.8: TD-DFT results for Cp_2V(bdt). Left: orbital description of transition, right: EDDM, blue=electron loss and red=electron gain.

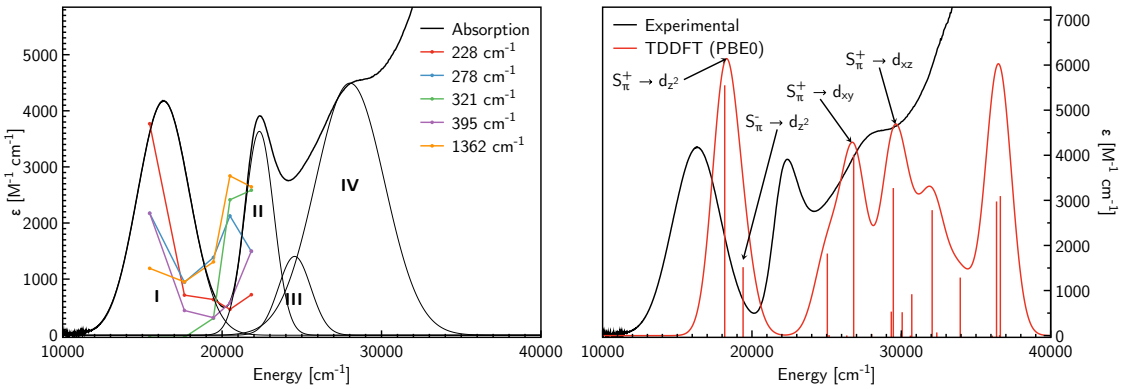

Figure 3.9: Absorption and rR spectroscopy of Cp_2Ti(benzenedithiolato). Left: rR profiles, center: gaussian resolved absorption spectrum, right: TD-DFT (PBE0) calculated spectrum.

L covalency with d-electron counts. The fact that these modes are excited in **2** and not **1** suggests that even with minimal ligand character electron count changes in the d_{z^2}) orbital has strong effects on M-L bonding. Multiple M-Cp modes are still present, however, they are all mixed with M-S or C-S stretches or dithiolene folding. Interestingly, the calculations suggest that several of the observed modes are combination and overtone bands.

Cp_2Ti(bdt)

The absorption spectrum of **3** (Figure 3.9) shows a large blue shift relative to **1** and **2**. This transition is easily assigned as a $S_\pi^+ \rightarrow d_{z^2}$ and the increased intensity of this transition relative to **2** is explained by the large increase in S_π^+/d_{z^2} mixing driven by further reduction in d-electron count. The rR spectrum of **3** (Figure 3.10) shows C-S and M-S modes being more strongly enhanced relative to M-Cp modes as compared to **1** and **2**. Mode descriptions are given in Table 3.8.

Of note is that the strongest two modes in the calculated spectrum involve ditho-

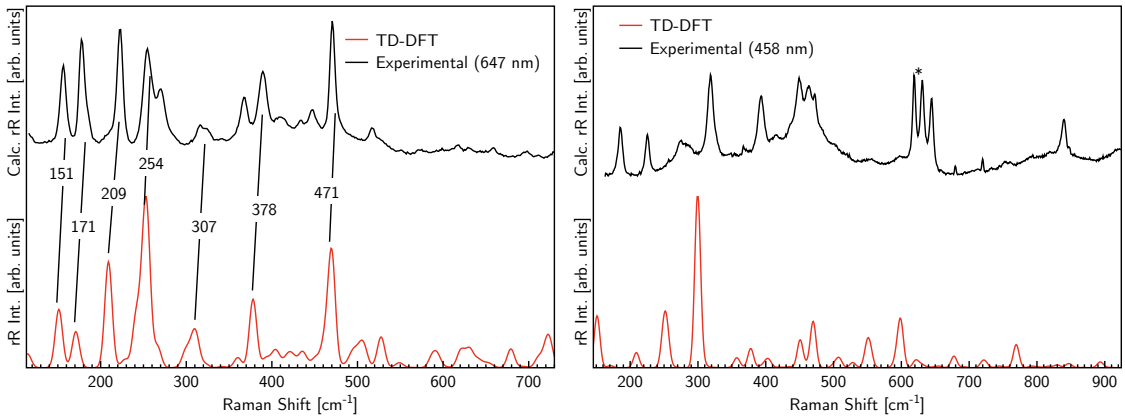

Figure 3.10: Resonance Raman spectra of $Cp_2Ti(bdt)$. On resonance with left: band I, right: band II.

	Energy [cm^{-1}]		$f \times 10^3$		
Band	exp.	calc.	exp.	calc.	Assignment
I	16323	18176	74	50	$S_\pi^+ + d_{z^2} \rightarrow S_\pi^+ - d_{z^2}$
II	22337	26810	36	40	$S_\pi^+ + d_{z^2} \rightarrow d_{xy}$
III	24542	-	14	-	-
IV	28019	-	108	-	-

Table 3.7: $Cp_2Ti(bdt)$ absorption data.

lene fold character, understandable within the context of the PJT surfaces discussed later. M-Cp modes are quite weak, completing the progression seen between **1** and **2**, and the M-S based distortions expected from a transition between highly mixed S_π^+ and d_{z^2} (bonding $\rightarrow$ transition) are dominant in the spectrum. Band II can be assigned as either a S_π^- to d_{z^2} or S_π^+ to d_{xy} based transition. TD-DFT calculations suggest that band II is the latter, and the strongest mode corresponds to a M-Cp stretch, analogous with the observed 236 cm^{-1} mode of 1.

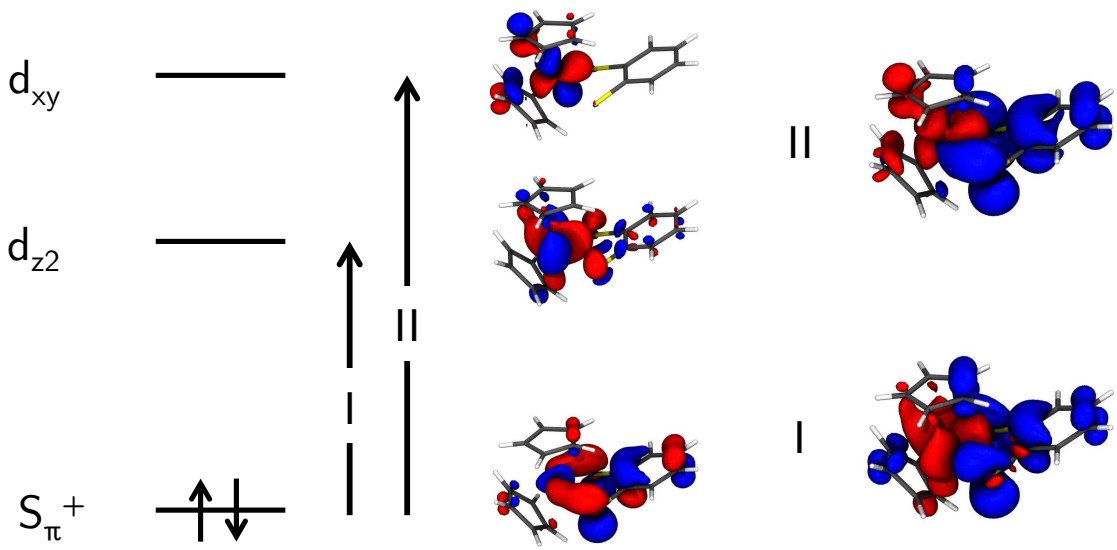

Figure 3.11: TD-DFT results for $Cp_2Ti(bdt)$. Left: orbital description of transition, right: EDDM, blue=electron loss and red=electron gain.

Frequency [cm^{-1}]		Intensity		
Exp.	Calc.	Exp.	Calc.	Mode description
Not obs.	57	-	0.99	Dithiolene fold
157	151	0.70	0.47	M-S Stretch
178	171	0.87	0.29	M-Cp str. + dt fold
223	209	0.94	0.75	S-M-S bend + M-S str.
255	250	0.8	0.55	M-Cp str + dt fold
270	254	0.54	1.0	Dithiolene fold + M-Cp str (as)
316	307	0.29	0.12	57 + 250 combination
325	312	0.26	0.22	57 + 254 combination
389	378	0.66	0.51	M-S str.
471	470	1.0	0.90	C-S str. + Ph ring mode

Table 3.8: $Cp_2Ti(bdt)$ vibrational modes.

3.2.3 Discussion: metal dithiolenes as an electron configuration dependent Jahn-Teller active system

Crystal structures of **1-3** show a trend towards larger dithiolene fold angles with a decrease in d-electron count, which has been typically described in the context of increased metal ligand covalency involving the redox orbital. Here we will show how this can be more rigorously described within the context of a PJT active system that is tuned by a) LMCT energy, and b) the value of F to give a system capable of changing the value of J-T stabilization by nearly 20-fold.

$Cp_2Ti(bdt)$

As an example of a system with a strong PJT effect, compound **3** will be examined first. To understand the origins of the PJT effect in $Cp_2Ti(bdt)$, DFT calculations were performed on the high symmetry C_{2v} form of **3**. These calculations show a nearly degenerate HOMO (S_π^+, b_1 symmetry) and LUMO ($d_{z^2\text{-}x^2}$, a_1 symmetry) with an orbital splitting of only 0.17 eV. The ground state of symmetry of C_{2v} **3** is A_1, and the HOMO (b_1) $\rightarrow$ LUMO (a_1) transition results in an excited state of B_1 symmetry which cannot directly mix with the ground state by configuration interaction (Figure 3.12). While the CT state cannot mix by CI due to symmetry restrictions, if the triple product $\Gamma_{A_1} \times \Gamma_Q \Gamma_{B_1}$ contains the totally symmetric representation (A_1) then the state mixing will be allowed by the vibronic coupling mechanism. This demonstrates that a vibrational mode of b_1 symmetry is capable of mixing these two states by a PJT mechanism. In support of this argument, frequency calculations on the high-symmetry geometry show a single negative frequency mode (-343 cm^{-1}) of b_1 symmetry, described as a bdt bending mode (i.e. ligand folding) (Figure 3.13).

Equation 3.1 can be rewritten in an orbital form for transitions that are well

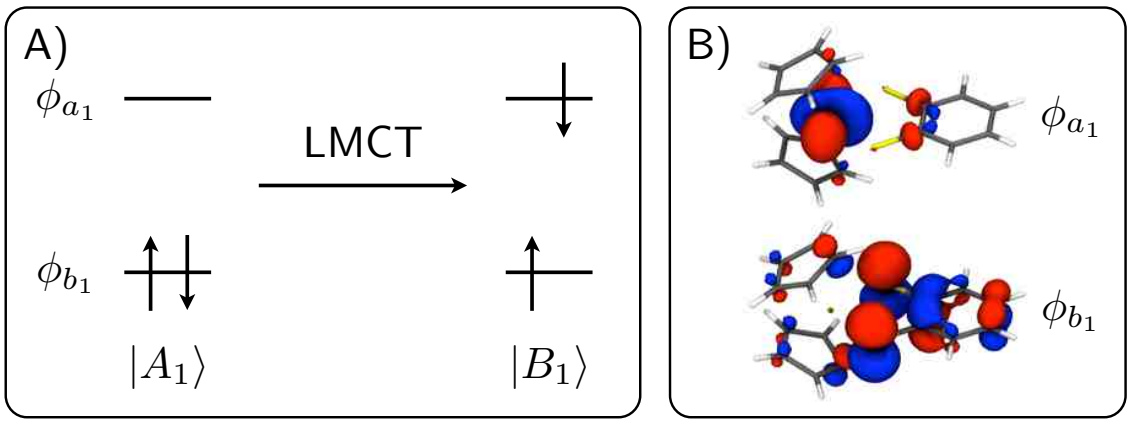

Figure 3.12: Orbital description of the pseudo Jahn-Teller effect in $Cp_2Ti(bdt)$. Symmetry labels are from the C_{2v} point group.

described by a single one-electron promotion $\psi_a \rightarrow \psi_b$:

$$F_{0i}^{\Gamma} = \left\langle \Psi_0 \left| \frac{\delta V}{\delta Q_{\Gamma}} \right| \Psi_i \right\rangle \tag{3.4}$$

$$= (q_a - q_b) \left\langle \psi_a \left| \frac{\delta V}{\delta Q_{\Gamma}} \right| \psi_b \right\rangle \tag{3.5}$$

$$= (q_a - q_b) f_{ab}^{\Gamma} \tag{3.6}$$

where ψ_a and ψ_b are the donor and acceptor orbitals involved in the electronic tran-

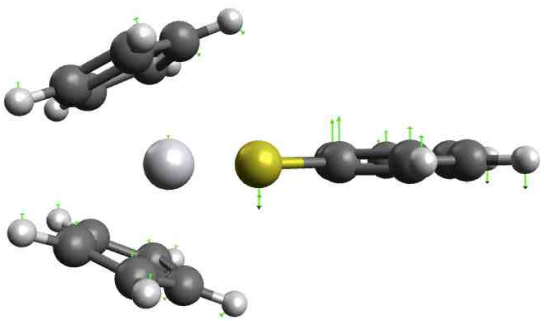

Figure 3.13: Pseudo Jahn-Teller active (B_1) vibrational mode of high-symmetry **3**. ω= -343 cm^{-1}, $K = -0.98$ mDyne/Å.

sition and q_a and q_b are their respective occupation numbers (0, 1, or 2). This clearly demonstrates how simply changing the occupation number of one of the orbitals involved in the PJT state mixing results in large changes in the magnitude of the off-diagonal elements of the vibronic coupling matrix.

$Cp_2V(bdt)$

With the orbital formalism described above, we can predict the behavior of **2**, which is a d^1 analogue of **3**. Using Equation 3.4 the reduction in orbital occupation can be seen to have a 4 fold decrease in F^2, even in the absence of any orbital character change. In addition, using simple electronic repulsion arguments, the transition is likely to occur at higher energies than in **3** as the acceptor orbital is now singly occupied. DFT calculations on the high-symmetry form of **2** show that the HOMO/LUMO gap has increased nearly 5-fold (to 0.8 eV). A 5x increase in Δ combined with the 4x decrease in F^2 will result in a 20x overall decrease in the $\frac{F^2}{\Delta}$ off-diagonal vibronic coupling matrix element.

$Cp_2Mo(bdt)$

Compound **1** provides an important example of a system with no PJT effect, as the mixing of the key LMCT state in **2** and **3** is no longer present due to the double occupation of the d_{z^2} orbital. This compound also provides a convenient benchmark for the non-vibronic force constant K_0, which is calculated to be only 2.8x10^{-3} mDyne/Åand corresponds to a 28 cm^{-1} vibrational mode. This small non-vibronic force constant is a necessary component (*vide supra*) of a large vibronic distortion.

3.2.4 Conclusions

Here we have shown how the simple series of metal dithiolenes (**1-3**) can be fully characterized by a combination of multiple spectroscopic techniques and advanced theoretical calculations. The results of these calculations serve as a foundation of understanding the PJT effect in metal dithiolenes, to a degree which is not yet possible in more complete structural models of the molybdenum active sites of enzymes. The PJT effect is found to arise from the uniquely close energetic arrangement of metal and ligand orbitals, which poises the complex for rapid electronic structure changes upon d-electron count change.

3.3 References

(1) Jahn, H. A.; Teller, E. *Proc. R. Soc. Lond. Math. Phys. Eng. Sci.* **1937**, *161*, 220–235, DOI: 10.1098/rspa.1937.0142.

(2) Bersuker, I. B., *The Jahn-Teller Effect*, 1st; Cambridge University Press: Cambridge, UK, 2006.

(3) Bersuker, I. B., *Electronic Structure and Properties of Transition Metal Compounds*, 2nd; John Wiley and Sons: Hoboken, New Jersey, 2010.

(4) Bersuker, I. B. *Theor. Exp. Chem.* **1981**, *16*, 235–240.

(5) Bersuker, I. B. *Chem. Rev.* **2001**, *101*, 1067–1114, DOI: 10.1021/cr0004411.

(6) Giolando, D. M.; Kirschbaum, K. *Synthesis* **1992**, *1992*, 451–452, DOI: 10.1055/s-1992-26132.

(7) Stephan, D. W. *Inorg. Chem.* **1992**, *31*, 4218–4223, DOI: 10.1021/ic00047a003.

(8) Joshi, H. K.; Cooney, J. J. A.; Inscore, F. E.; Gruhn, N. E.; Lichtenberger, D. L.; Enemark, J. H. *Proc. Natl. Acad. Sci. U.S.A.* **2003**, *100*, 3719, DOI: 10.1073/pnas.0636832100.

(9) Petrenko, T.; Neese, F. *J. Chem. Phys.* **2007**, *127*, 164319.

(10) Petrenko, T.; Kossmann, S.; Neese, F. *Chem. Phys.* **2011**, *134*, 4116, DOI: 10.1063/1.3533441.

(11) Weigend, F.; Ahlrichs, R. *Phys. Chem. Chem. Chem. Phys.* **2005**, *7*, 3297–3305, DOI: 10.1039/b508541a.

(12) Perdew, J. P.; Burke, K.; Ernzerhof, M. *Phys. Rev. Lett.* **1996**, *77*, 3865–3868.

(13) Adamo, C.; Barone, V. *J. Chem. Phys.* **1999**, *110*, 6158–6170.

(14) Neese, F.; Wennmohs, F.; Hansen, A.; Becker, U. *Chem. Phys.* **2009**, *356*, 98–109, DOI: 10.1016/j.chemphys.2008.10.036.

(15) Velde, G. T.; Bickelhaupt, F. M.; Baerends, E. J.; Guerra, C. F.; Van Gisbergen, S. J. A.; Snijders, J. G.; Ziegler, T. *J. Comput. Chem.* **2001**, *22*, 931–967.

(16) Seth, M.; Ziegler, T.; Autschbach, J. *J. Chem. Phys.* **2008**, *129*, 104105, DOI: 10.1063/1.2976568.

(17) Heller, E. J.; Sundberg, R.; Tannor, D. *J. Phys. Chem.* **1982**, *86*, 1822–1833.

(18) Tutt, L. W.; Zink, J. I.; Heller, E. J. *Inorg. Chem.* **1987**, *26*, 2158–2160, DOI: 10.1021/ic00260a029.

Part II

Radicals Reporters of Excited State Configurations

Chapter 4

Excited State Exchange Interactions as Probes of Dark States

A series of (diimine)M(L) (where L=bidentate chalcogen donor) compounds provide a promising framework for the study of how large excited state interactions can effect excited state properties. The charge separated (diimine$^{\bullet-}$)M(L$^{\bullet+}$) LLCT excited state formally creates a spin-singlet biradical, potentially creating large excited state interactions with pendant radicals. In this chapter a magnetic circular dichroism (MCD) study of several radical elaborated (dbbpy)Pt(Cat-B-NN) compounds is presented, where B=none, thiophene, or phenyl and NN=nitronyl nitroxide. This for the determination the effect of varied excited state exchange interactions on the magnetic properties of the system and provides a direct probe of states that are only very weakly allowed with conventional optical techniques.

4.1 Introduction

Square planar platinum donor-acceptor compounds have been extensively studied due to their interesting photophysical and redox properties[1–3]. Typically the acceptor group is a diimine (e.g. bipyridine) and the donor is a dichalcogen containing ligand such as benzenedithiol, catechol, or non-aromatic counterparts of the same. In particular, the dithiolene containing complexes typically show long-lived emission[1], while the catechol complexes do not[4]. This has been attributed to ligand field states providing for an efficient pathway to relax singlet excited state, but no evidence has been presented identifying these states, nor explaining how the sulfur analogues avoid this problem. Recently, a study was published[5] which proposed a solution to this problem. Through the use of a variety of chalcogens (O,S,Se) it was shown that the excited state lifetimes appeared to be dominated by spin-orbit and spin-vibronic effects. Furthermore, it was shown that the $S_1 \rightarrow T_1$ intersystem crossing (ISC) was symmetry forbidden but the $S_1 \rightarrow T_2$ pathway was allowed. In L=catechol, the T_2 state is *above* S_1, and so no ISC is possible. For the heavier chalcogens the T_2 state is found near or below S_1, enabling efficient ISC.

In recent years, there has been a surge of interest in the effect of organic radicals on excited state dynamics. Questions have been raised as to the role that the radical can play in facilitating ISC[6, 7] or photoinduced electron transfer[8]. The systems studied thus far are typically in the weak exchange limit, with couplings on the order of 1 cm^{-1} or less. Even with these small exchange coupling values, measurable differences in excited state lifetimes and electron transfer rates have been observed.

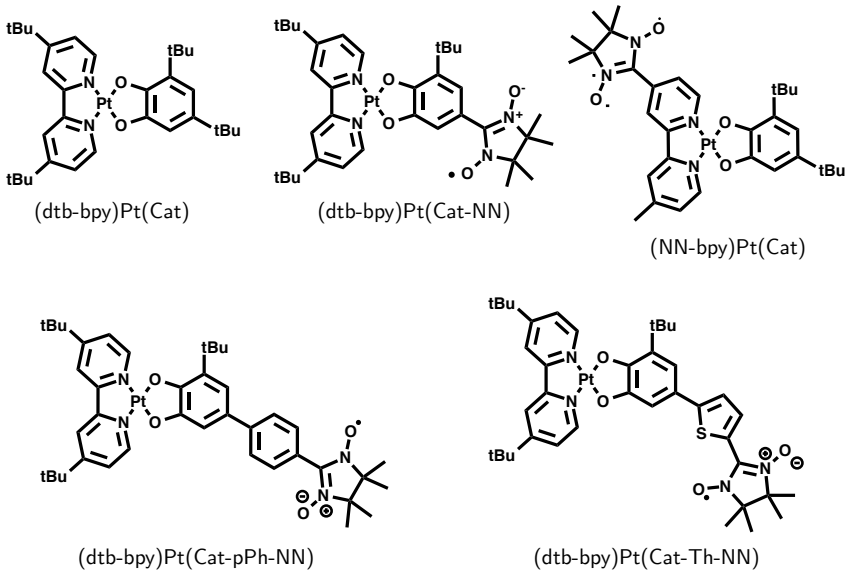

Figure 4.1: (bipyridine)Pt(catechol) compounds studied by MCD in this work.

4.2 Synthesis and Spectroscopy

Synthesis

The syntheses of the compounds under study are outlined in Figure 4.2, and shown in Figure 4.1. The previously published synthesis[4] consists of a simple halide exchange reaction between (bpy)$PtCl_2$ and the potassium salt of the desired catechol ligand, formed by the reaction between the catechol and KOH. The parent compound, (4,4'-di-tertbutyl-2,2'-bipyridine)Pt(3,5-di-tert-butylcatechol) was synthesized at UNM. NN appended compounds were synthesized at NCSU by Chris Tichnell.

Magnetic Circular Dichroism Spectroscopy

MCD spectra were taken with an Oxford SM4000T magnetooptical cryostat interfaced with a Jasco J-810 spectropolarimeter. Samples were made up as 2-methyl-

tetrahydrofuran solutions and injected into a custom brass sample holder containing quartz windows, a butyl rubber spacer, and rubber o-rings. The samples were frozen in liquid N_2 and loaded into the cryostat which was held at $\sim$ 60K[1]. Depolarization was checked by the use of a nickel tartrate sample placed before and after the cryostat and samples which showed less than 5% depolarization were deemed suitable. Baseline corrections were performed by subtraction of a 0T spectrum and, where necessary, B-term spectral contributions were eliminated by subtraction of a high-temperature (50K), high-field (7T) spectrum from the low-temperature spectra. Samples with very weak S/N were enhanced by the collection of forward and reverse field spectra and subtraction of these gives a spectra free of field independent contributions.

Electronic Absorption Spectroscopy

Absorption spectra were taken on a Hitachi U-4100 double beam spectrophotometer. Room temperature samples were made up as 2-methyltetrahydrofuran solutions and loaded into a micro-volume quartz cuvette. Low temperature absorption spectra were taken with a custom Janis LHe flow cryostat mounted in a Hitachi U-3100 spectrophotometer. Samples were loaded into a brass sample holder identical to that used for MCD measurements, and baseline corrected with a frozen solvent sample. Temperature was monitored with a Si diode interfaced to a Lakeshore temperature controller and was adjusted by changing the flow of LHe through the cryostat and with nichrome wire heaters located above the sample and at the bottom of the cryostat.

[1] 2-MeTHF samples show a tendency to severely crack if cooled too quickly.

Electron Paramagnetic Resonance Spectroscopy

EPR spectra were taken on a Bruker EMX X-band EPR spectrometer. Samples were made up as CH_2CL_2 solutions of approximately 1mM concentration. All spectra were taken at room temperature. Instrument settings are given with the figures in the text.

Computational Methods

All calculations were performed with the ORCA 3.0.1 or 3.0.2 program suite[9]. Density functional theory (DFT) geometry optimizations were done with the def2-TZVP basis[10] and the PBE[11] GGA functional. complete active space self-consistent field (CASSCF)/NEVPT2 calculations used quasi-restricted orbitals (QROs) from the DFT calculations as the initial guess orbitals. Minimal active space calculations (CAS(3,3) or CAS(2,2) for radical elaborated or non-elaborated compounds, respectively) were first performed, and the molecular orbitals obtained were used for subsequent calculations using larger active spaces (see Appendix D). MCD spectra were calculated using the quasi-degenerate perturbation theory (QDPT) spin-orbit coupling module in ORCA[12].

4.3 Results and Analysis

Absorption spectra of all compounds are shown in Figure 4.3 and the MCD spectra of the LLCT region of compounds 2 and 3 are shown in Figure 4.6. Low temperature absorption spectra is overlaid with the VT-MCD of **1** in Figure 4.5[2]. Of immediate

[2]Direct comparison of the room-temperature absorption and MCD spectra of **1** will result in a different MCD $\longleftrightarrow$ absorption correspondence, due to the large dipole change

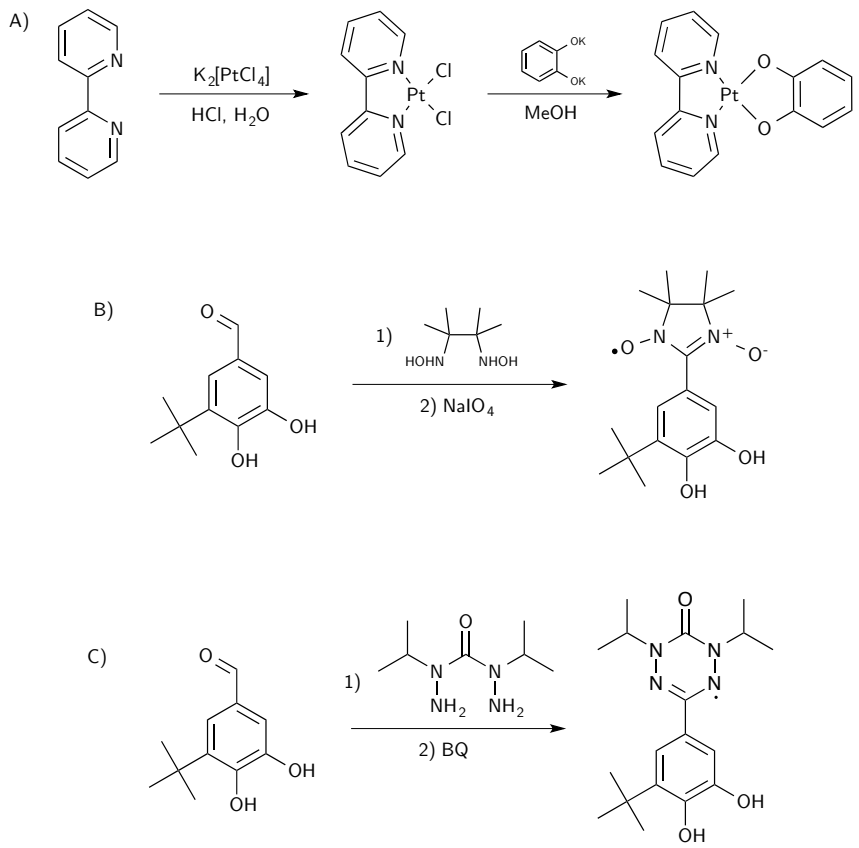

Figure 4.2: Synthesis of (diimine)Pt(catechol) complexes. A) General (diimine)Pt(catechol) synthetic procedure, B) synthesis of catechol-NN ligand, C) synthesis of catechol-VZ ligand.

note is the drastic decrease in MCD intensity between the three compounds, however the spectra of **2** and **3** can be seen to have some features in common, notably a prominent pseudo-A term at low energy, which corresponds to low-energy LLCT band. The MCD spectrum of **4** was difficult to obtain due to very low MCD dispersion, however the high energy positive component is clearly detectable and some small temperature dependent features can be seen on the low energy side. The EPR spectrum of **1** is shown in Figure 4.4. The EPR shows $_{14}$N hyperfine which is nearly identical to that previously reported for free NN radicals[14].

which 2-MeTHF undergoes upon freezing[13].

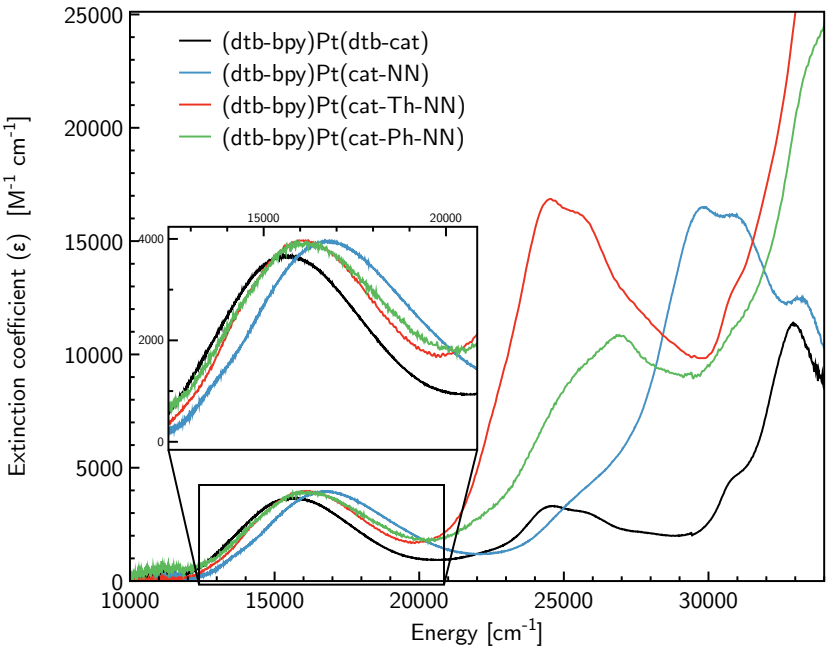

Figure 4.3: Room temperature absorption spectra of the (bpy)Pt(catechol) complexes under study. Solvent: CH_2Cl_2.

The absorption spectra of square-planar platinum compounds has been well studied, and is known to possess a reasonably intense low-energy (15-20k cm^{-1}) LLCT band[2, 4, 15]. The calculated MCD spectrum of 2 is shown in Figure (CAS spectrum). Good agreement is obtained, with the relative intensities and signs being well reproduced. The calculated MCD spectra show a pronounced "pseudo-A"[3] term at low energy, with the higher energy positive component corresponding to the intense absorption feature. Interesting, the low energy negative C-term does not appear to correspond with any notable absorption features and so it is of great interest to determine the origin of this transition.

[3]Pseudo-A term refers to a spectral feature which has the same derivative band shape as a traditional A-term, but shows temperature dependence. This is actually a set of unresolved overlapping C-terms[16].

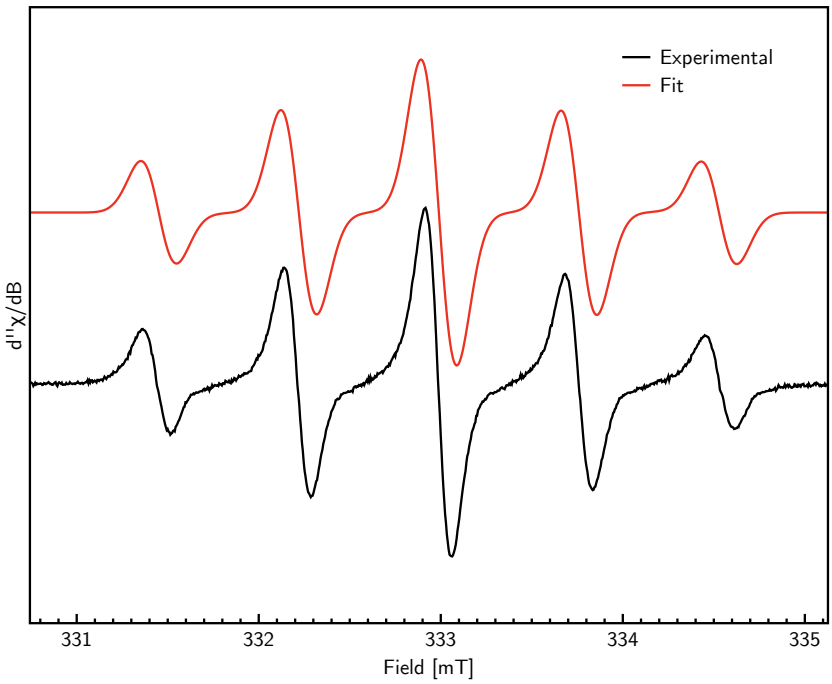

Figure 4.4: RT EPR spectrum of (dbbpy)Pt(cat-NN). Modulation amplitude: 1G, modulation frequency: 100kHz, frequency: 9.36GHz. Fit parameters: A=21.5 MHz, linewidth=0.2 mT.

The MCD intensity drops dramatically as the bridge is modified (Figure 4.6), being reduced by a factor of 3.5 from no bridge, to thiophene bridged and finally phenyl bridged. Here we show how the wavefunctions derived from a simple three-spin exchange Hamiltonian can adequately describe 1) the signs of the observed C-terms, 2) the relative intensities of the two C-terms, and 3) the observed radical-semiquinone exchange dependence. The three-spin model allows for the derivation of explicit expressions for the MCD intensity, with matrix elements being able to be analyzed graphically resulting in the determination of absolute MCD signs for several potential energy manifolds.

In general, the MCD C-term intensity for a transition $A \rightarrow J$ is a function of spin-orbit coupling between either J and other excited states K, or between the

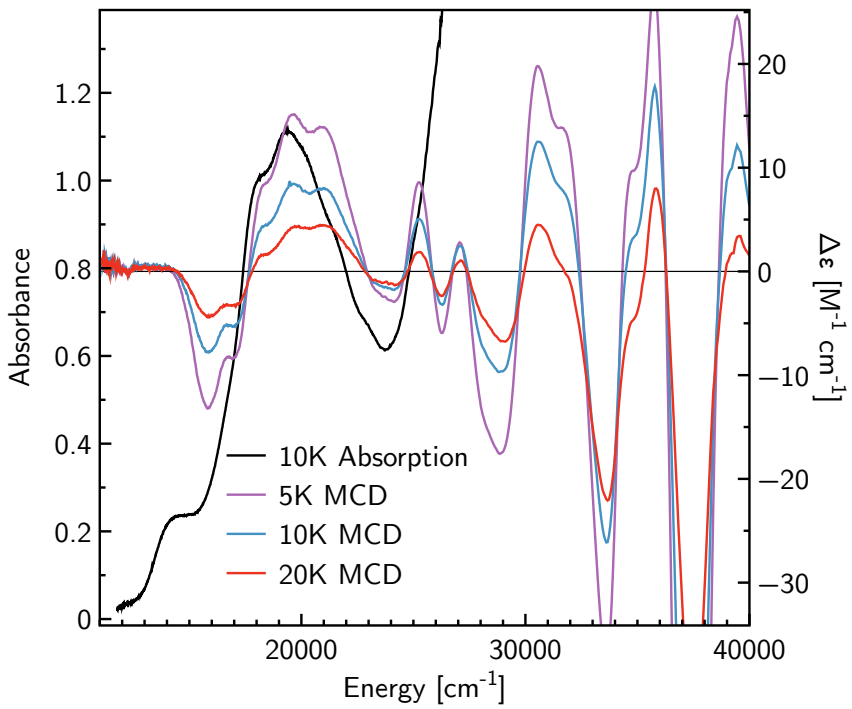

Figure 4.5: VT-MCD and low-temperature absorption spectra of (dtb-bpy)Pt(cat-NN). Field strength: 7T, solvent: 2-methyltetrahydrofuran.

ground state A and excited states K[16, 17]:

$$C(A \to J) \propto (-)\epsilon_{\alpha\beta\gamma} \sum_{K \neq J} L_{\alpha}^{JK} D_{\beta}^{AJ} D_{\gamma}^{AK} + L_{\alpha}^{AK} D_{\beta}^{AJ} D_{\gamma}^{JK} \tag{4.1}$$

where L are spin-orbit matrix elements, and e.g. D_{α}^{AK} is the transition dipole matrix element for $A \to K$ in direction α(x, y, or z). Note that the excited state mechanism requires two excited states with non-collinear transition dipoles that are coupled by a spin-orbit interaction which are also non-collinear with the transition dipoles. Here we will ignore the ground state mechanism, as it is often a minor contribution[16] and the spectra show little sign of sum-rule violation and the EPR spectra (Figure 4.4) are identical to that of the free ligand[4]. Therefore, to derive expressions for

[4]EPR spectra are sensitive to ground state spin-orbit coupling (SOC) effects, and and the absence of any g-anisotropy or Pt hyperfine clearly demonstrates that none is present.

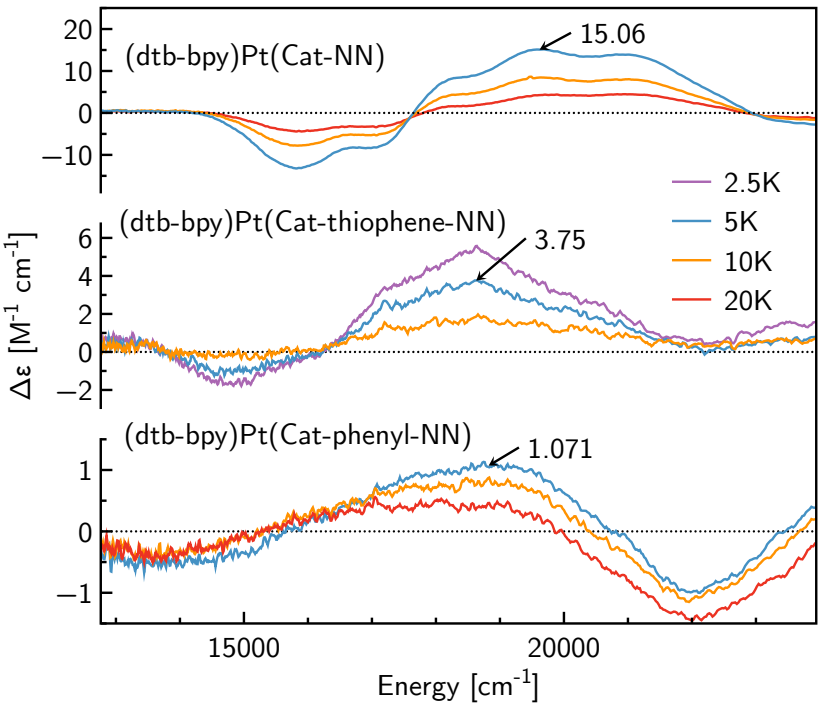

Figure 4.6: VT-MCD spectra of (bpy)Pt(catechol) complexes. Solvent: 2-methyltetrahydrofuran.

the MCD we will need the spin-orbit and transition dipole matrix elements between the wavefunctions of choice. Here we use a similar treatment as has been applied to the determination of MCD C-term signs in $Mo(O)Cl_3$dppe[18], but cast in terms of a HDvV Hamiltonian to fully explore the exchange mixing origins of the observed MCD behavior. In this chapter only the final expressions will be shown; however, full derivations can be found in Appendix D.

A three-spin, two J HDvV Hamiltonian has the following general form:

$$\hat{H} = -2J'\hat{S}_{bpy}\hat{S}_{SQ} - 2J\hat{S}_{SQ}\hat{S}_{NN} \tag{4.2}$$

with the eigenvalues[19, 20] (Figure 4.7),

$$E_{1/2} = {}^1/_2\left(J + J' \pm 2\sqrt{J^2 - JJ' + J'^2}\right) \tag{4.3a}$$

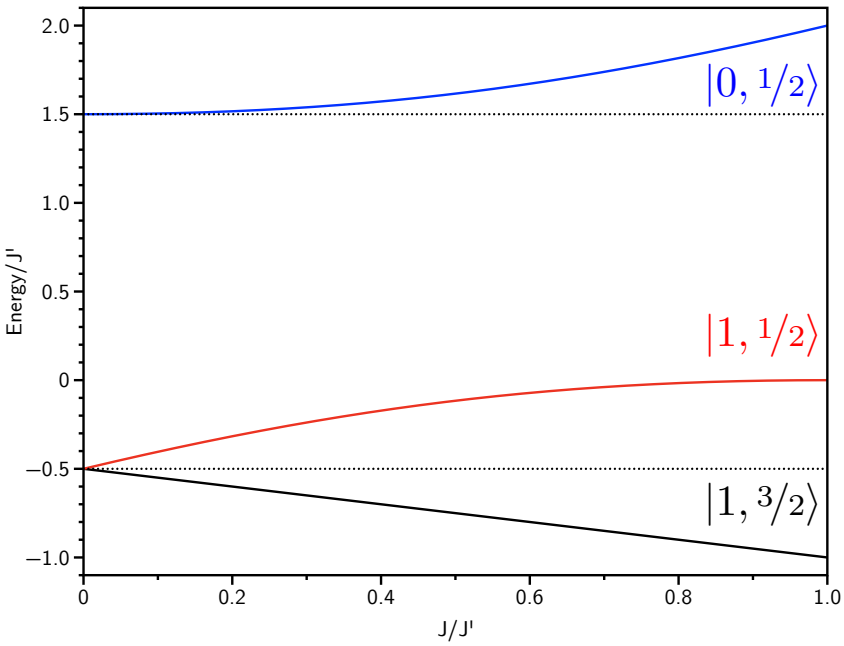

Figure 4.7: Eigenvalues of the 3 spin, 2 J HDvV Hamiltonian. States are labeled with a $|S_{AB}, S_T\rangle$

$$E_{3/2} = -1/2\,(J + J') \tag{4.3b}$$

where e.g. the $1/2$ refers to the $S = 1/2$ manifold. The exchange mixed doublet states (denoted by the prime notation) have the corresponding eigenvectors,

$$|1', 1/2\rangle = cos\lambda\,|1, 1/2\rangle + sin\lambda\,|0, 1/2\rangle \tag{4.4a}$$

$$|0', 1/2\rangle = cos\lambda\,|0, 1/2\rangle - sin\lambda\,|1, 1/2\rangle \tag{4.4b}$$

where $\lambda$is the mixing coefficient, which is defined as a function of J and J':

$$\lambda = 1/2 Tan^{-1}\left(\frac{\sqrt{3}J}{2J' - J}\right) \tag{4.5}$$

These eigenvalues result in an energy manifold as seen in Figure 4.7, with two doublet states ("sing-doublet" and "trip-doublet") and a quartet state. The doublet states can be named based upon whether they originated from the triplet or singlet

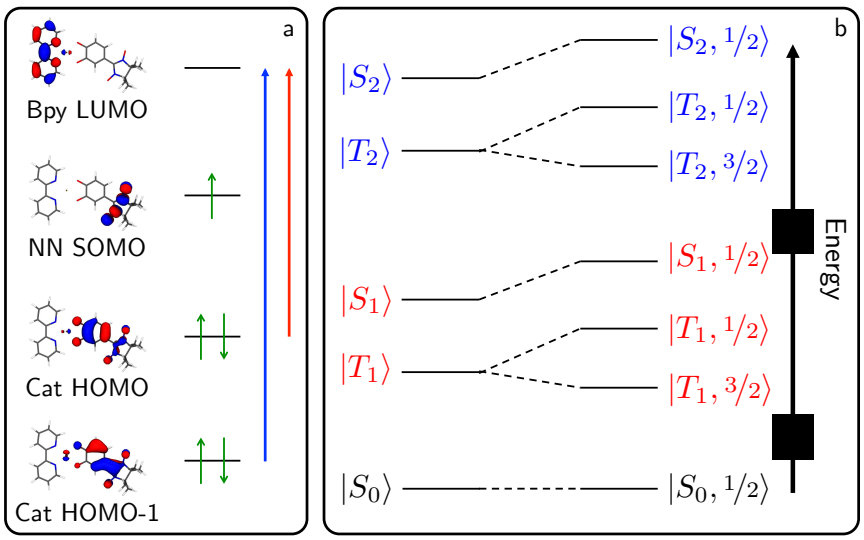

Figure 4.8: Orbital origins of the LLCT states. A) Frontier MOs (CASSCF orbitals), B) results of coupling a pendant radical to triplet and singlet states.

radical pair state of the parent two-spin system, a convention developed by Ake and Gouterman's studies on metal porphyrins[21].

In (bpy)Pt(Cat) systems the lowest two excited configurations are known to be cat→bpy charge transfer excitations (LLCT) from the cat HOMO and cat HOMO-1 to the bpy LUMO[4] (see Figure 4.8, left for a set of CASSCF derived orbitals), which results in a manifold of two singlet and two triplet excited states[4, 5, 22] (Figure 4.8, right). Upon addition of a radical these states couple as described above to form four excited doublet states (the quartet states will be ignored in this treatment): $|T_1, 1/2\rangle$, $|S_1, 1/2\rangle$, $|T_2, 1/2\rangle$, and $|S_2, 1/2\rangle$, where e.g. $|T_1, 1/2\rangle$ represents the trip-doublet which arises from the cat HOMO → bpy LUMO excitation. These states and the ground state are represented by the following combinations of Slater determinants[23]:

$$|S_1, 1/2\rangle = 1/\sqrt{2}\left(\left|\phi_L\overline{\phi_H}\phi_{NN}\right| - \left|\overline{\phi_L}\phi_H\phi_{NN}\right|\right) \tag{4.6a}$$

$$|T_1, 1/2\rangle = 1/\sqrt{6}\left(\left|\phi_L\overline{\phi_H}\phi_{NN}\right| + \left|\overline{\phi_L}\phi_H\phi_{NN}\right| - 2\left|\phi_L\phi_H\overline{\phi_{NN}}\right|\right) \tag{4.6b}$$

$$|S_2, 1/2\rangle = 1/\sqrt{2}\left(\left|\phi_L\overline{\phi_{H-1}}\phi_{NN}\right| - \left|\overline{\phi_L}\phi_{H-1}\phi_{NN}\right|\right) \tag{4.6c}$$

$$|T_2, 1/2\rangle = 1/\sqrt{6}\left(\left|\phi_L\overline{\phi_{H-1}}\phi_{NN}\right| + \left|\overline{\phi_L}\phi_{H-1}\phi_{NN}\right| - 2\left|\phi_L\phi_{H-1}\overline{\phi_{NN}}\right|\right) \tag{4.6d}$$

where ϕ_L, ϕ_H, ϕ_{H-1}, and ϕ_{NN} are the LUMO, HOMO, HOMO-1, and NN SOMO respectively, and an overbar represents a β electron.

Equation 4.1 shows that in order to derive equations for MCD intensity, we require the dipole matrix elements between the ground state and all excited states of interest, and spin-orbit matrix elements between the excited states. The dipole matrix elements are:

$$\langle S_0 \left| r_\alpha \right| S_1, 1/2\rangle = D_\alpha^{S_0,S_1} = \sqrt{2}\left\langle \phi_H \left| r_\alpha \right| \phi_L \right\rangle \tag{4.7a}$$

$$\langle S_0 \left| r_\alpha \right| T_1, 1/2\rangle = D_\alpha^{S_0,T_1} = 0 \tag{4.7b}$$

$$\langle S_0 \left| r_\alpha \right| S_2, 1/2\rangle = D_\alpha^{S_0,S_2} = \sqrt{2}\left\langle \phi_{H-1} \left| r_\alpha \right| \phi_L \right\rangle \tag{4.7c}$$

$$\langle S_0 \left| r_\alpha \right| T_2, 1/2\rangle = D_\alpha^{S_0,T_2} = 0 \tag{4.7d}$$

and the spin-orbit matrix elements are:

$$\langle S_2 \left| l_\alpha \cdot s_\alpha \right| S_1, 1/2\rangle = 0 \tag{4.8a}$$

$$\langle S_2 \left| l_\alpha \cdot s_\alpha \right| T_1, 1/2\rangle = L_\alpha^{S_2,T_1} = -1/\sqrt{12}\left\langle \phi_{H-1} \left| l_\alpha \right| \phi_H \right\rangle = -1/\sqrt{12} l_\alpha^{H-1,H} \tag{4.8b}$$

$$\langle T_2 \left| l_\alpha \cdot s_\alpha \right| S_1, 1/2\rangle = L_\alpha^{T_2,T_1} = -1/\sqrt{12} l_\alpha^{H-1,H} \tag{4.8c}$$

$$\langle T_2 \left| l_\alpha \cdot s_\alpha \right| T_1, 1/2\rangle = L_\alpha^{T_2,T_1} = 1/3 l_\alpha^{H-1,H} \tag{4.8d}$$

where $l_\alpha^{H-1,H}$ is the orbital spin-orbit coupling matrix element between HOMO and HOMO-1. Note that all of these matrix elements are between the 0^{th} order states, i.e. *before* the effects of any exchange mixing. The matrix elements between the exchange mixed states (denoted by a prime, e.g. S_1') are simply related to these 0th-order states through the exchange mixing coefficient λ and the Clebsch-Gordon coefficients:

$$\langle S_0 \left| r_\alpha \right| S_1', 1/2\rangle = D^{S_0,S_1'} = cos\lambda D^{S_0,S_1} \tag{4.9a}$$

$$\langle S_0 \left| r_\alpha \right| T_1', 1/2\rangle = D^{S_0,T_1'} = sin\lambda D^{S_0,S_1} \tag{4.9b}$$

$$\langle S_0 \left| r_\alpha \right| S_2', 1/2\rangle = D^{S_0,S_2'} = cos\lambda D^{S_0,S_2} \tag{4.9c}$$

$$\langle S_0 \left| r_\alpha \right| T_2', 1/2\rangle = D^{S_0,T_2'} = sin\lambda D^{S_0,S_2} \tag{4.9d}$$

$$\langle S_2', 1/2 \left| l_\alpha \cdot s_\alpha \right| S_1', 1/2\rangle = L_\alpha^{S_2',S_1'} = \frac{2cos\lambda sin\lambda}{\sqrt{12}} l_\alpha^{H-1,H} \tag{4.10a}$$

$$\langle T_2', 1/2 \left| l_\alpha \cdot s_\alpha \right| S_1', 1/2\rangle = L_\alpha^{T_2',S_1'} = -\frac{1}{\sqrt{12}} l_\alpha^{H-1,H} \tag{4.10b}$$

$$\langle S_2', 1/2 \left| l_\alpha \cdot s_\alpha \right| T_1', 1/2\rangle = L_\alpha^{S_2',T_1'} = -\frac{1}{\sqrt{12}} l_\alpha^{H-1,H} \tag{4.10c}$$

$$\langle T_2', 1/2 \left| l_\alpha \cdot s_\alpha \right| T_1', 1/2\rangle = L_\alpha^{T_2',T_1'} = \frac{1}{3} l_\alpha^{H-1,H} \tag{4.10d}$$

Using Equation 4.1 and the matrix elements given in Equations 4.7a-4.10 expressions for the MCD intensity can be obtained. By analysis of the orbitals involved in the transitions between the states of interest, the equation can be simplified by realizing that all transitions to the S_1 manifold are x-polarized and those to the S_2 manifold are y-polarized (Figure). The necessary SOC is therefore L_z. With this, the equation for the MCD of $S_0 \rightarrow T_1'$ is:

$$C(S_0 \rightarrow T_1') \propto -\frac{\lambda l_z^{H-1,H}}{\sqrt{12}\Delta_{S_2'T_1'}} D_y^{S_0S_2} D_x^{S_0S_1} \tag{4.11}$$

Similarly, for $S_0 \rightarrow S_1'$:

$$C(S_0 \rightarrow S_1') \propto \frac{\lambda l_z^{H-1,H} D_y^{S_0S_2} D_x^{S_0S_1}}{\sqrt{12}} \left(\frac{2}{\Delta_{S_2'S_1'}} - \frac{1}{\Delta_{T_2'S_1'}} \right) \tag{4.12}$$

With these expressions an expression for the C-term intensity ratio presents itself:

$$\frac{C(S_0 \rightarrow S_1')}{C(S_0 \rightarrow T_1')} = -\Delta_{S_2'T1'} \left(2\Delta_{S_2'S_1'}^{-1} - \Delta_{T_2'S_1'}^{-1} \right) \quad = -\left(\epsilon + \delta\right) \left(\frac{2}{\epsilon} - \frac{1}{\epsilon - \delta} \right) \tag{4.13}$$

where ϵ is the $S_1 \rightarrow S_2$ energy gap and $\delta = \sqrt{J^2 - JJ' + J'^2}$.

These equations predict a near linear dependency[5] of the total MCD intensity on J (through λ, see Equation D.15), while the *relative* intensities of $C(S_0 \rightarrow S_1)$

[5]Strictly speaking $\Delta\epsilon \propto cos\lambda sin\lambda$, however for small $\lambda cos\lambda sin\lambda \approx \lambda$.

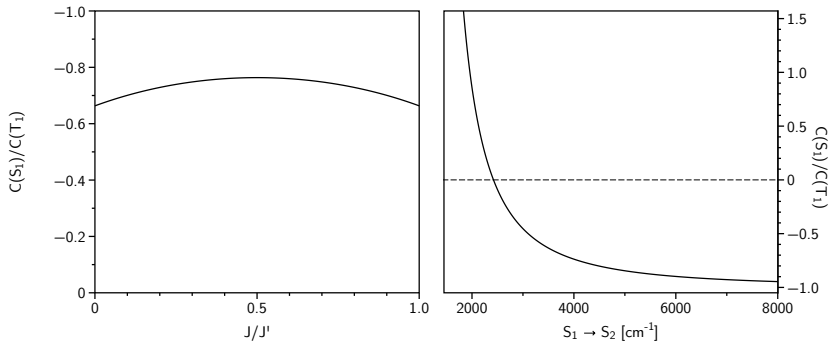

Figure 4.9: Effect of of J (left) and $S_1 \rightarrow S_2$ (ϵ, right) on $C(S_1)/C(T_1)$.

and $C(S_0 \rightarrow T_1)$ are only minimally affected (Figure 4.9, left). Experimental data is in support of this model (Figure 4.10), with excellent linear correlation between $sin\lambda cos\lambda$. The S_1/T_1 ratio is strongly affected not by J, but rather by the relative energetics of the S_1 and S_2 manifolds (Figure 4.9, right). It can be shown that the sign of S_1' can flip if $\Delta^{-1}_{T_2'S_1'} > 2\Delta^{-1}_{S_2'S_1'}$, which occurs if the T_2' is lowered in energy enough such as has been proposed to occur in (bpy)Pt(bdt)[5].

These equations enable several other interesting conclusions. As alluded to earlier, the observed -/+ pattern places a lower bound on the relative energetics of the S1/S2 manifolds (and corresponding triplet states). This has strong implications for understanding intersystem crossing and internal conversion events in (diimine)Pt(dichalcogen) systems.

Expressions for the MCD intensity of $S_0 \rightarrow S_2'$ and $S_0 \rightarrow T_2'$ are able to be derived, allowing for the potential assignment of these states in the experimental spectrum:

$$C\left(S_0 \rightarrow S_2'\right) \propto -\frac{\lambda l_z^{H-1,H} D_x^{S_0S_1} D_y^{S_0S_2}}{\sqrt{12}} \left(\frac{2}{\Delta_{S_2'S_1'}} - \frac{1}{\Delta_{S_2'T_1'}}\right) \tag{4.14}$$

and

$$C\left(S_0 \rightarrow T_2'\right) \propto \frac{\lambda \bar{l}_z^{H-1,H}}{\sqrt{12}\Delta_{T_2'S_1'}} D_y^{S_0S_2} D_x^{S_0S_1} \tag{4.15}$$

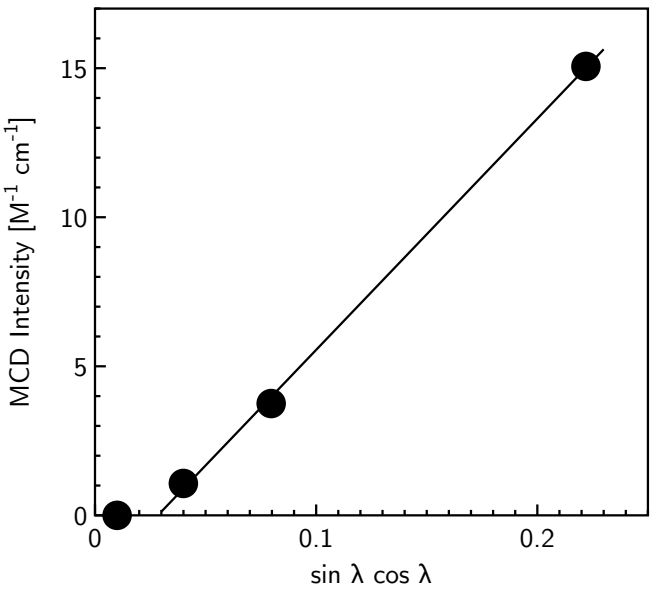

Figure 4.10: MCD intensity of $C\,(S_0 \rightarrow S_1)$ as a function of λ.

and it is easily seen that $C\,(T_2') \propto -C\,(T_1')$. Since $\Delta_{S_2'T_1'}$ is always greater than $\Delta_{S_2'S_1'}$, $C\,(S_2') \propto -C\,(S_1')$ provided also that $\Delta^{-1}_{T_2'S_1'} > 2\Delta^{-1}_{S_2'S_1'}$.

With this in hand, we can now assign the primary features in the absorption spectrum. Again assuming that $\Delta^{-1}_{T_2'S_1'} > 2\Delta^{-1}_{S_2'S_1'}$ the above equations predict either a -/+/+/- or +/-/-/+ MCD pattern, dependent upon the specific signs of $l_z^{H-1,H}$, $d_x^{H,L}$, and $d_y^{H-1,L}$. The signs of these matrix elements can be determined by the so-called graphical method[17] where simple graphical constructs allow us to evaluate these signs (Figure 4.11). First, the spin orbit dipole is shown to be $-z$, obtained by first applying the l_z operator to ϕ_H and seeing that the resultant rotated orbital is the negative of ϕ_{H-1}. Dipole matrix elements are even more simply evaluated, by multiplying the two orbitals in the matrix element and drawing a vector from the center of negative sign (dark) to the positive center (white). By combining these three matrix elements, the absolute sign for $C(T_1')$ can be predicted:

$$C(S_0 \rightarrow T_1') \propto -l_z^{H-1,H} D_y^{S_0S_2} D_x^{S_0S_1}$$

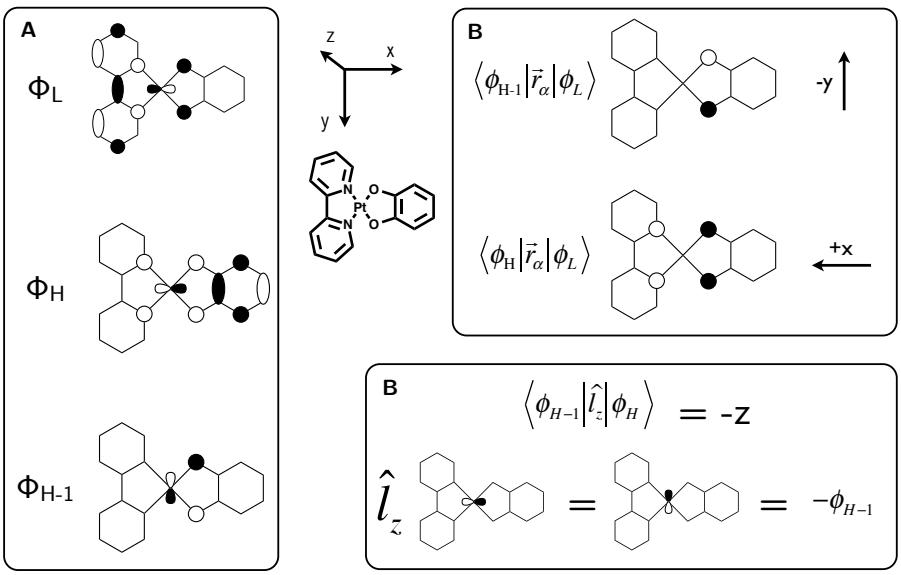

Figure 4.11: Graphical evaluation of spin-orbit and dipole matrix elements. A) Simplified representation of frontier MOs (obtained from CASSCF calculations), B) dipole matrix elements, obtained by multiplying the two orbitals in the matrix element and drawing a vector from the center of negative sign (dark) to the positive center (white). C) Spin-orbit matrix element, obtained by rotating the right orbital counter-clockwise (while looking down the z-axis) and observing the overlap with the left orbital. The coordinate system used is given in the center, which follows C_s symmetry conventions (xy plane is defined as the plane of mirror symmetry).

$$\begin{aligned} &\propto (-)(-z)(-y)(+x) \\ &\propto (-) \end{aligned} \tag{4.16}$$

and therefore the -/+/+/- pattern is expected. Indeed, experimental data clearly shows this pattern (Figure 4.12), enabling for accurate estimates of 1) $\Delta_{S_1'T_1'}$, 2) $\Delta_{S_2'T_2'}$, and 3) $\Delta_{S_1'S_2'}$. While DFT calculations of the MCD spectrum were unsuccessful, a CASSCF calculation supports the above spectral assignments, with the -/+ C term components arising from the $\phi_H \rightarrow \phi_L$ LLCT.

With the assignment of the trip-doublet and sing-doublet wavefunctions, the

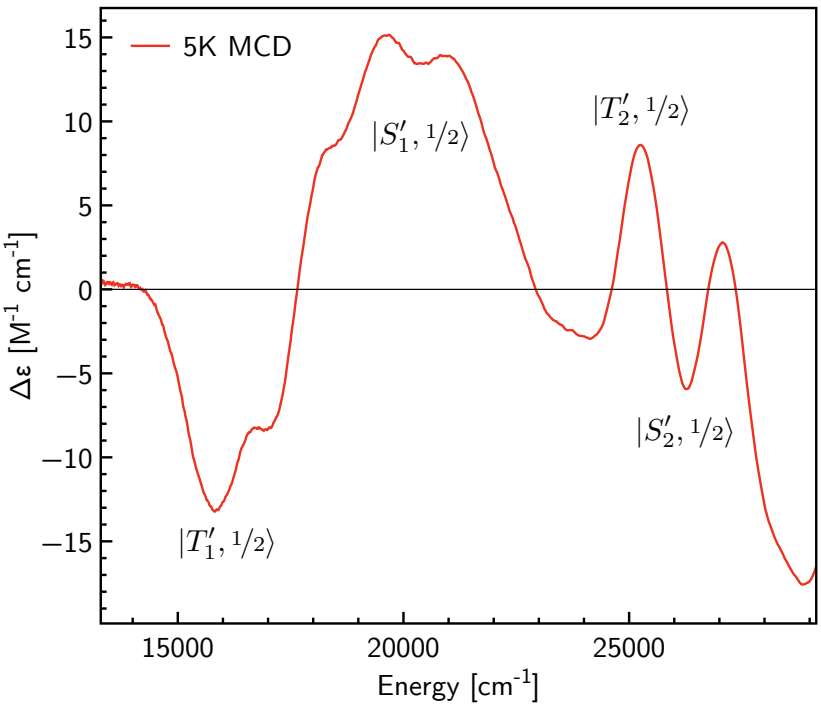

Figure 4.12: MCD spectral assignements. See text for a full explanation of the band assignments.

singlet-triplet splitting of the parent compound (J') can be determined:

$$\begin{aligned}\Delta =& E(|S_1, 1/2\rangle) - E(|T_2, 1/2\rangle) \\ =& 4\sqrt{J^2 - JJ' + J'^2}\end{aligned}$$

$$J' = 1/2(J + \sqrt{-3J + \Delta^2}) \tag{4.17}$$

which gives a value of J'=1394 cm^{-1} for Δ=2466 cm^{-1} and J=550 cm^{-1}. This value is in excellent agreement with CASSCF calculations of the parent (bpy)Pt(cat) compound, which give a J' of 1310 cm^{-1}, a difference of less than 10%. A similar calculation using the Δ derived from (dtb-bpy)Pt(cat-Th-NN) gives a J' of 1339 cm^{-1}, which is quite close considering the error inherent in determining the $0 \rightarrow 0$ band position in the MCD spectra. CASSCF calculations (see Appendix D) of the MCD

spectrum appears to put the low energy feature at slightly too high of an energy, possibly due to an underestimation of the singlet-triplet splitting of **1** and subsequent overestimation of exchange mixing of the sing-doublet and trip-doublet states.

Further information can be extracted by having explicit wavefunctions for the sing-doublet and trip-doublet states, and the effect of the exchange mixing can be further examined by determination of the spin populations on the three spin-bearing fragments of the molecule[6]. Figure 4.13 shows how the spin polarization by the pendant radical varies strongly both between the two states as a function of NN-SQ J. At $J/J' = 0$ the sing-doublet state is described as having no net spin population on the bipyridine and catechol fragments (Figure 4.13, left), with the NN having the entire unpaired electron. As the exchange coupling becomes operative, we see the catechol fragment gaining positive spin while the bipyridine is negative. This facilitates the favorable SQ-NN interaction, which is net ferromagnetic. Conversely, the trip-doublet state shows bipyridine-catechol positive spin with a negative contribution from the NN fragment, which is what would be expected for a subtractive coupling between the local triplet pair state and the NN.

4.4 Conclusions and Outlook

The use of MCD spectroscopy in conjunction with radical elaboration of diamagnetic compounds has been shown to provide a high-resolution probe of their ground and excited state electronic structure. Theoretical calculations support the simple three-spin isotropic exchange Hamiltonian model that we have used to understand the origins of the observed MCD sign and intensity. Using the equations derived above, an extremely detailed picture of the excited state manifold can be constructed, and this includes the specifics of excited state energy splittings and spin densities, which are

[6]A full derivation of the spin population equations are given in Section D.2.

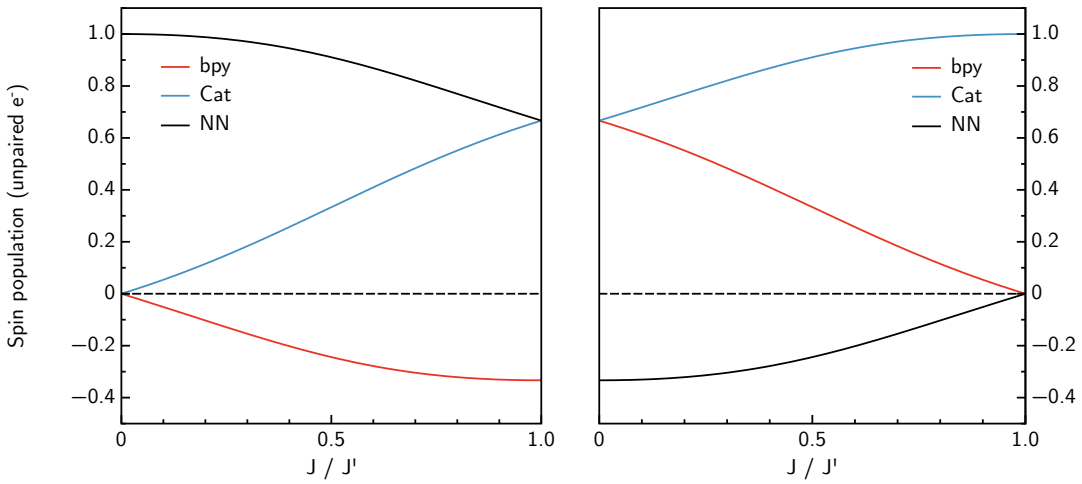

Figure 4.13: Calculated spin populations of the $S_0 \rightarrow S_1', T_1'$ excited states. Left: sing-doublet, right: trip-doublet

important properties that are exceedingly difficult or impossible to determine. Typically, in order to gain a more advanced understanding of excited states of differing spin than the ground state the compound of interest must be capable of undergoing intersystem crossing so that phosphorescence or transient absorption measurements can be made. The former only gives information about the lowest lying state[7], and while transient absorption is fairly well developed, the interpretation of the data is often exceedingly difficult due to the low resolution of the data. While many systems containing multiple organic and inorganic radicals have been studied, this work represents the first where an appended radical was used specifically to probe the electronic structure of a diamagnetic molecule, rather than e.g. the magnetic coupling between the radical and metal.

This method appears to be broadly applicable to a number of important systems

[7]Due to Kasha's rule.

and is capable of extracting an extraordinary amount of electronic and magnetic structure information, such as the relative energetics of spin-forbidden states and detailed band assignments. Relatively simple wavefunctions can be used to understand the entirety of the excited state manifold, and higher level calculations (e.g. CASSCF) can be used for additional insight. Some basic guidelines for the use of this technique can be developed based upon the experience gained during this study. It was found that the minimal amount of metal spin density in the excited states of these compounds limited the overall signal to noise ration of the the MCD measurements. The use of a heavy element such as platinum neatly sidestepped this issue, however, future studies may incorporate compounds with greater degrees of metal-ligand covalency to avoid this problem. Also, it was found that due to the large parent compound singlet-triplet splitting (J'), the overall mixing of the sing-doublet and trip-doublet states by the action of the pendant radical was minimized. CASSCF calculations found this to be due to the large degree of HOMO→LUMO CI mixing into the ground state, described within a single-configuration MO approach as HOMO/LUMO mixing. This is not expected to be universal, and so systems with smaller singlet-triplet gaps may find increased signal intensity.

As a final point of interest, several interesting compounds can be proposed which bring together the ideas discussed in Chapter 2. Previous work on donor-acceptor biradicals have found that these systems are very powerful in studying how varied bridge moieties modulate electronic communication and transport[24, 25]. One could now imagine studying the communication through models which seek to replicate varied portions of the complicated ppd cofactor, and how these modulate electronic communication with the metal center. As an example, consider Tp*MoO(bdt-NN) shown in Figure 4.14 (top). This would study how a simple dithiolene facilitates this communication, and simple VTVH-MCD studies would be extremely powerful at elucidating and ZFS and exchange interactions between the Mo^{V} and NN radicals. A second interesting model would be based upon the fascinating pyranopterin dithi-

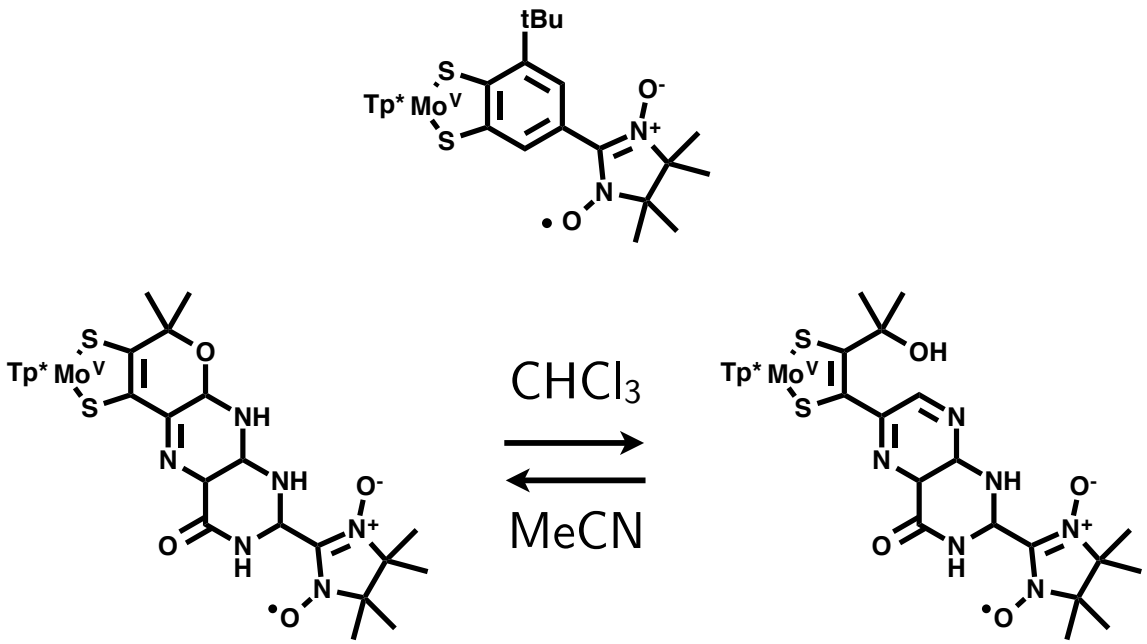

Figure 4.14: Hypothetical radical appended pyranopterin dithiolene model compounds. Top: Tp*MoO(bdt-NN), bottom: reversible pyran ring opening in a radical appended pyranopterin dithiolene model.

olene model Tp*MoO(S_2BMOPP), which has only recently been synthesized and characterized[26]. This model was found to exhibit facile and reversible pyran ring opening, the equilibrium of which is easily affected by solvent polarity. This provides an opportunity to study how the distortions induced by the pyran effect electronic coupling, which were shown in Section 2.2 to be of possibly great importance.

4.5 References

(1) Cummings, S. D.; Eisenberg, R. *J. Am. Chem. Soc.* **1996**, *118*, 1949–1960.

(2) Hissler, M.; McGarrah, J. E.; Connick, W. B.; Geiger, D. K.; Cummings, S. D.; Eisenberg, R. *Coord. Chem. Rev.* **2000**, *208*, 115–137.

(3) Zuleta, J. A.; Burberry, M. S.; Eisenberg, R. *Coord. Chem. Rev.* **1990**, *97*, 47–64, DOI: 10.1016/0010-8545(90)80079-9.

(4) Best, J.; Sazanovich, I. V.; Adams, H.; Bennett, R. D.; Davies, E. S.; Meijer, A. J. H. M.; Towrie, M.; Tikhomirov, S. A.; Bouganov, O. V.; Ward, M. D.; Weinstein, J. A. *Inorg. Chem.* **2010**, *49*, 10041–10056, DOI: 10.1021/ic101344t.

(5) Yang, J.; Kersi, D. K.; Giles, L. J.; Stein, B. W.; Feng, C.; Tichnell, C. R.; Shultz, D. A.; Kirk, M. L. *Inorg. Chem.* **2014**, *53*, 4791–4793, DOI: 10.1021/ic500217y.

(6) Teki, Y.; Miyamoto, S.; Iimura, K.; Nakatsuji, M.; Miura, Y. *J. Am. Chem. Soc.* **2000**, *122*, 984–985, DOI: 10.1021/ja993151e.

(7) Ito, A.; Shimizu, A.; Kishida, N.; Kawanaka, Y.; Kosumi, D.; Hashimoto, H.; Teki, Y. *Angewandte Chemie International Edition in English* **2014**, n/a–n/a, DOI: 10.1002/anie.201310291.

(8) Chernick, E. T.; Mi, Q.; Kelley, R. F.; Weiss, E. A.; Jones, B. A.; Marks, T. J.; Ratner, M. A.; Wasielewski, M. R. *J. Am. Chem. Soc.* **2006**, *128*, 4356–4364, DOI: 10.1021/ja0576435.

(9) Neese, F. *WIREs Comput Mol Sci* **2012**, *2*, 73–78, DOI: 10.1002/wcms.81.

(10) Weigend, F.; Ahlrichs, R. *Phys. Chem. Chem. Phys.* **2005**, *7*, 3297–3305, DOI: 10.1039/b508541a.

(11) Perdew, J. P.; Burke, K.; Ernzerhof, M. *Phys. Rev. Lett.* **1996**, *77*, 3865–3868.

(12) Ganyushin, D.; Neese, F. *J. Chem. Phys.* **2008**, *128*, 114117, DOI: 10.1063/1.2894297.

(13) Bublitz, G. U.; Boxer, S. G. *J. Am. Chem. Soc.* **1998**, *120*, 3988–3992, DOI: 10.1021/ja971665c.

(14) Kirk, M. L.; Shultz, D. A.; Habel-Rodriguez, D.; Schmidt, R. D.; Sullivan, U. *J. Phys. Chem. B* **2010**, *114*, 14712–14716, DOI: 10.1021/jp102955j.

(15) Paw, W.; Cummings, S. D.; Adnan Mansour, M.; Connick, W. B.; Geiger, D. K.; Eisenberg, R. *Coord. Chem. Rev.* **1998**, *171*, 125–150, DOI: 10.1016/S0010-8545(98)90023-6.

(16) Kirk, M. L.; Peariso, K. *Curr. Opin. Chem. Biol.* **2003**, *7*, 220–227.

(17) Neese, F.; Solomon, E. I. *Inorg. Chem.* **1999**, *38*, 1847–1865, DOI: 10.1021/ic981264d.

(18) Westphal, A.; Broda, H.; Kurz, P.; Neese, F.; Tuczek, F. *Inorg. Chem.* **2012**, DOI: 10.1021/ic300201t.

(19) Bencini, A.; Benelli, C.; Dei, A.; Gatteschi, D. *Inorg. Chem.* **1985**, *24*, 695–699, DOI: 10.1021/ic00199a012.

(20) Bencini, A.; Gatteschi, D., *EPR of Exchange Coupled Systems*; Dover Publications: Mineola, NY, 2012.

(21) Ake, R. L.; Gouterman, M. *Theor. Chim. Acta* **1969**, *15*, 20–42, DOI: 10.1007/BF00526463.

(22) Archer, S.; Weinstein, J. A. *Coord. Chem. Rev.* **2012**, *256*, 2530–2561, DOI: 10.1016/j.ccr.2012.07.010.

(23) Pauncz, R., *Spin Eigenfunctions: Construction and Use*; Plenum Press: New York, 1979.

(24) Kirk, M. L.; Shultz, D. A.; Depperman, E. C.; Brannen, C. L. *J. Am. Chem. Soc.* **2007**, *129*, 1937–1943, DOI: 10.1021/ja065384t.

(25) Kirk, M. L.; Shultz, D. A. *Coord. Chem. Rev.* **2013**, *257*, 218–233, DOI: 10.1016/j.ccr.2012.07.007.

(26) Williams, B. R.; Fu, Y.; Yap, G. P. A.; Burgmayer, S. J. N. *J. Am. Chem. Soc.* **2012**, *134*, 19584–19587, DOI: 10.1021/ja310018e.

Appendix A

Computational Methods

Only the very briefest of overviews of the computational methods used in this work will be discussed here. For more complete discussions, there exist several excellent review articles on the subject[1–4].

Most modern computational chemistry methods which are used on molecular scale problems seek to solve the problem of electron correlation, which is typically defined as the energy difference between the true molecular energy and the Hartree-Fock energy,

$$E_{corr} = E_{exact} - E_{HF} \tag{A.1}$$

and unfortunately is typically of the same magnitude of chemical bonds. The conceptually simplest, but by far the least efficient, method is that of configuration interaction (CI). By expanding the wavefunction to include excitations from occupied to unoccupied orbitals, the exact energy can be approached. However, with any non-infinite basis sets this limit is never reached. Typically this expansion is cut-off at some number of excitations (e.g. CI-singles, CI-singles and doublets, etc.).

By allowing for the variation of the orbital coefficients, the broader class of multi-

configurational SCF (MC-SCF) methods arise, of which the complete active space SCF (CASSCF) is a member. These methods extend upon the Hartree-Fock (HF) wavefunction ansatz by relaxing the restriction that the wavefunction consists of a single reference configuration. As compared to CI methods, the orbital coefficients c are optimized in addition to the CI coefficients C:

$$\Psi_{CI} = \sum_{n=0} C_n \Phi_n$$

where the Φ_n are configuration state functions (CSFs) formed from excitations from the reference configuration ground configuration. While the varied single-reference CI methods differ in how many excitations are included, e.g. CIS, CISD, etc., a CASSCF wavefunction is made from all possible excitations within a specified *active space*, chosen by the user. These active spaces are specified the number of orbitals (n) and number of electrons (m), often abbreviated as CAS(n,m). The cost of the calculation is factorially dependent on the number of orbitals and electrons, and so are often limited to 15 orbitals. This is not necessarily a large limitation, as perturbational methods are available which correct for the neglect of excitations not included in the active space, provided their contribution is not large.

CASSCF (and other MC-SCF methods) only treat what is known as *static* correlation, that is electron correlation effects which arise from near degeneracies in configurations and only usually involve a handful of orbitals. *Dynamic* correlation typically involves a large number of orbitals, and slowly converges with active space size. This is best handled through the use of either a limited CI with a reference space formed by a CAS method (multi-reference CI) or ideally a perturbational approach such as CASPT2 or NEVPT2.

An efficient alternative to CI type methods is density functional theory (DFT). While the origins of DFT date back to the early 1900s[5], all modern formulations of the theory are based on the Hohenberg-Kohn theorem and Kohn-Sham equations. In their groundbreaking paper[6], it was shown that the electronic energy is a *functional*

of the electron density, and has a variational principle which shows that any trial density will have a higher energy than the true electron density. Subsequently, it was shown[7] that there is also a one-to-one mapping between a the density of a collection of interacting electrons and a fictional non-interacting system. This allows for the use of orbitals, known as Kohn-Sham orbitals, which are from the non-interacting system.

Unfortunately the exact functional remains unknown, and so a "functional soup" has arisen which necessitates extensive benchmarking to ensure that the chosen functional is appropriate for a given problem. Luckily, functionals within one of the varied families (e.g. GGA, hybrid, meta-GGA, etc.) typically behave similarly and so it is only necessary to compare within a limited set. Throughout this work most calculations have typically used the PBE[8] GGA functional or the PBE0 hybrid functional[9]. These have been shown[3, 10] to give excellent results with transitional metal and other "electronically difficult" systems.

A.1 References

(1) Neese, F.; Petrenko, T.; Ganyushin, D.; Olbrich, G. *Coord. Chem. Rev.* **2007**, *251*, 288–327, DOI: 10.1016/j.ccr.2006.05.019.

(2) Dreuw, A.; Head-Gordon, M. *Chem. Rev.* **2005**, *105*, 4009–4037, DOI: 10.1021/cr0505627.

(3) Orio, M.; Pantazis, D. A.; Neese, F. *Photosyn Res* **2009**, *102*, 443–453, DOI: 10.1007/s11120-009-9404-8.

(4) Neese, F. *Coord. Chem. Rev.* **2009**, *253*, 526–563, DOI: 10.1016/j.ccr.2008.05.014.

(5) Parr, R. G.; Yang, W., *Density-functional theory of atoms and molecules*; Oxford university press: New York, 1989.

(6) Hohenberg, P.; Kohn, W. *Phys. Rev.* **1964**, *136*, B864–B871.

(7) Kohn, W.; Sham, L. J. *Phys. Rev.* **1965**, *140*, A1133–A1138.

(8) Perdew, J. P.; Burke, K.; Ernzerhof, M. *Phys. Rev. Lett.* **1996**, *77*, 3865–3868.

(9) Adamo, C.; Barone, V. *J. Chem. Phys.* **1999**, *110*, 6158–6170.

(10) Adamo, C.; Barone, V. *Theor. Chim. Acta* **2000**, *105*, 169–172.

Appendix B

NEGF Calculations with ADF

NEGF calculations with the ADF program package are relatively straightforward, if time consuming. It is the Author's wish that this appendix will enable the interested reader to perform these calculations with a minimum of confusion. It is assumed that the reader has a working installation of ADF and is familiar with creating and running ADF jobs, whether on a local installation or remotely[1].

A successful ADF NEGF electron transport calculation is composed of several steps:

- Calculation of an appropriate gold atomic fragment wavefunction. The example given in the ADF manual creates a very small relativistic basis set for gold, greatly speeding up the calculations.
- Calculation of the electrode self-energies, which creates both the keyfiles and the electrode wavefunction (`.t21`) files. This is done with a calculation on

[1]With the exception of the simplest systems, NEGF calculations are computationally intensive and it is strongly recommended to perform these calculations on a powerful computer cluster.

three principle layers of gold, each constructed of three atomic layers.

- Removal of the bulk layer and insertion of the molecule fragment. It is typically not necessary to optimize the geometry, but attention should be paid to how the contact atoms are orientated with respect to the gold surface.

- Single-point calculation of the model system, using the free molecule `.t21` file and the gold `layer.t21` files as fragment guesses.

- NEGF calculation using the `green` module of ADF.

- Integration of the resultant transmission data, using a desired range of bias voltages (typically 0-1V, larger biases are likely less accurate due to assumption that the transmission is independent of bias).

Transport calculations, including the DZ/large frozen core gold basis set and gold slab coordinates were derived from the examples given in the ADF2013 manual. Model systems were constructed as follows: ppd cofactors (neutral form) containing a thiol group in place of the terminal amine were optimized at the PBE/TZVP level using ADF2012.01. The seperately optimized cofactor was inserted between two 27-atom gold slabs (3 layers of 9 atoms), with the sulfur atoms located at Au(111) hollow sites and at a S-Au distance of 2.55Å[1]. NEGF calculations were performed with the `GREEN` module of ADF2013.01 [2, 3].

Example ADF input file for single point calculation

This example input file needs the TAPE21 files from proceeding calculations: `layer.t21` from the calculation on the gold electrode and the TAPE21 file from the free bridge molecule (`dh_opt.t21` in this example). These large calculations are typically diffi-

cult to converge, so different convergence settings will need to be tried for your own system.

```
TITLE 10,10a-Dihydro with gold contacts

ATOMS
Coordinates go here (see below for full coordinate definitions)
END

CHARGE -3

XC
LDA SCF VWN
END

RELATIVISTIC Scalar ZORA

Fragments
    left $SCM_RESULTDIR/layer.t21
    pterin $SCM_RESULTDIR/dh_opt.t21
    right $SCM_RESULTDIR/layer.t21
end
SAVE  TAPE21 TAPE13

SCF
iterations 1000
diis  n=20
LISTi
```

```
END

OCCUPATIONS keeporbitals=9999

FULLSCF
```

Example ADF *green* input file

This is an example input file for the `green` module in ADF. The left and right keyfiles (.kf) are generated by the example given in the ADF manual[2]. In this example dihydro.t21 refers to the TAPE21 file formed from the single point calculation on the entire model system as discussed above.

```
DOS $SCM_RESULTDIR/dihydro.t21
TRANS $SCM_RESULTDIR/dihydro.t21
EPS -0.2 0.5 2000
ETA 1e-6
LEFT $SCM_RESULTDIR/right.kf
    FRAGMENT left
END
RIGHT $SCM_RESULTDIR/left.kf
    FRAGMENT right
END
NOSAVE DOS_B, TRANS_B
```

[2]As of the writing of this manuscript, the example can be found either in the ADF package or on the SCM website: http://www.scm.com/Doc/Doc2014/ADF/Examples/page140.html.

Coordinates of model systems used in this work

Below are the coordinates of the three model systems described in Section 2.2 given in the ADF input file format.

Tetrahydro pyranopterin

```
ATOMS
1 Au  -12.029758130000 -7.610267581000  1.703669855000  f=left b=left
2 Au  -12.029759130000 -5.111788581000  0.261171859900  f=left b=left
3 Au  -12.029759130000 -5.111788581000  3.146167855000  f=left b=left
4 Au  -12.029759130000 -2.613308581000 -1.181326145000  f=left b=left
5 Au  -12.029759130000 -2.613308581000  1.703669855000  f=left b=left
6 Au  -12.029759130000 -2.613308581000  4.588665855000  f=left b=left
7 Au  -12.029759130000 -0.114829582300  0.261171859900  f=left b=left
8 Au  -12.029759130000 -0.114829582300  3.146167855000  f=left b=left
9 Au  -12.029759130000  2.383650419000  1.703669855000  f=left b=left
10 Au   -9.67417020700 -5.944614581000  1.703669855000  f=left b=left
11 Au   -9.67417020700 -3.446135581000  0.261171859900  f=left b=left
12 Au   -9.67417020700 -3.446135581000  3.146167855000  f=left b=left
13 Au   -9.67417020700 -0.947655582800 -1.181326145000  f=left b=left
14 Au   -9.67417020700 -0.947655582800  1.703669855000  f=left b=left
15 Au   -9.67417020700 -0.947655582800  4.588665855000  f=left b=left
16 Au   -9.67417020700  1.550824419000  0.261171859900  f=left b=left
17 Au   -9.67417020700  1.550824419000  3.146167855000  f=left b=left
18 Au   -9.67417020700  4.049303420000  1.703669855000  f=left b=left
```

```
19 Au   -7.31858120700 -4.278961581000  1.703669855000  f=left b=left
20 Au   -7.31858120700 -1.780481581000  0.261171859900  f=left b=left
21 Au   -7.31858120700 -1.780481581000  3.146167855000  f=left b=left
22 Au   -7.31858120700  0.717997417400 -1.181326145000  f=left b=left
23 Au   -7.31858120700  0.717997417400  1.703669855000  f=left b=left
24 Au   -7.31858120700  0.717997417400  4.588665855000  f=left b=left
25 Au   -7.31858120700  3.216477420000  0.261171859900  f=left b=left
26 Au   -7.31858120700  3.216477420000  3.146167855000  f=left b=left
27 Au   -7.31858220700  5.714956420000  1.703669855000  f=left b=left
28 Au    7.82603093300  2.481847053000  1.460699784000  f=right b=right
29 Au    7.87262049500  4.966736313000 -0.004343750451  f=right b=right
30 Au   10.03688508000 -3.413079757000  0.054297781020  f=right b=right
31 Au   10.08347469000 -0.928189498300 -1.410745773000  f=right b=right
32 Au   10.10468164000 -0.902524642700  1.474058119000  f=right b=right
33 Au   10.13006425000  1.556699763000 -2.875789313000  f=right b=right
34 Au   10.15127120000  1.582364618000  0.009014585466  f=right b=right
35 Au   10.17247815000  1.608029474000  2.893818473000  f=right b=right
36 Au   10.19786079000  4.067254878000 -1.456028969000  f=right b=right
37 Au   10.21906774000  4.092919733000  1.428774924000  f=right b=right
38 Au   10.26565630000  6.577809016000 -0.036268602850  f=right b=right
39 Au    7.80482398300  2.456182198000 -1.424104109000  f=right b=right
40 Au    5.25081251000 -6.635225138000  0.118147493000  f=right b=right
41 Au    5.29740107300 -4.150335856000 -1.346896045000  f=right b=right
42 Au    5.31860802300 -4.124671000000  1.537907848000  f=right b=right
43 Au    5.34399065700 -1.665445596000 -2.811939594000  f=right b=right
44 Au    5.36519760800 -1.639780741000  0.072864304700  f=right b=right
45 Au    5.38640455800 -1.614115885000  2.957668192000  f=right b=right
46 Au    5.41178717000  0.845108517800 -1.392179240000  f=right b=right
47 Au    5.43299412000  0.870773373400  1.492624652000  f=right b=right
48 Au    5.47958370500  3.355663634000  0.027581109340  f=right b=right
```

```
49 Au    7.64384830100 -5.024152437000  0.086222640330  f=right b=right
50 Au    7.69043786300 -2.539263177000 -1.378820905000  f=right b=right
51 Au    7.71164481300 -2.513598321000  1.505982988000  f=right b=right
52 Au    7.73702744800 -0.054372918660 -2.843864454000  f=right b=right
53 Au    7.75823439800 -0.028708063120  0.040939444980  f=right b=right
54 Au    7.77944134800 -0.003043207664  2.925743332000  f=right b=right
55 N    -1.759807581000 -0.310984792900 -0.690472384100  f=tet b=tet
56 N     0.252323323700  0.512820281600  1.055542060000  f=tet b=tet
57 C    -1.029341467000  1.037739611000  1.147467299000  f=tet b=tet
58 C    -2.054768016000  0.575662029100  0.339590893800  f=tet b=tet
59 C     0.543067352000 -3.048011034000 -0.114348365100  f=tet b=tet
60 C     1.858610848000 -2.279977303000 -0.039144852850  f=tet b=tet
61 C     1.889245876000 -0.928480080400 -0.044140472020  f=tet b=tet
62 C     0.633650548400 -0.103399270800 -0.209302692000  f=tet b=tet
63 C    -0.509595140300 -1.002529659000 -0.715869952300  f=tet b=tet
64 O    -0.588995272400 -2.193614083000  0.082910549810  f=tet b=tet
65 C    -1.302373974000  2.042257495000  2.132310369000  f=tet b=tet
66 N    -3.363558302000  0.954427793300  0.464163130800  f=tet b=tet
67 C     0.421297561800 -4.160531566000  0.920345991600  f=tet b=tet
68 S     3.290106170000 -3.323896587000  0.010073118590  f=tet b=tet
69 S     3.386695182000  0.046904619860  0.102079846900  f=tet b=tet
70 N    -2.674155726000  2.394844613000  2.184438673000  f=tet b=tet
71 C    -3.632711494000  1.838784497000  1.386788173000  f=tet b=tet
72 H    -2.904392674000  3.117886521000  2.864719674000  f=tet b=tet
73 S    -5.308567595000  2.367162664000  1.713633113000  f=tet b=tet
74 H     0.965128178700  1.092421668000  1.500676437000  f=tet b=tet
75 O    -0.474884860300  2.582483169000  2.881033209000  f=tet b=tet
76 H    -0.283835845900 -1.291333436000 -1.759666761000  f=tet b=tet
77 H    -2.563287243000 -0.811622577900 -1.062788011000  f=tet b=tet
78 H    -0.557377598000 -4.645930370000  0.810819152400  f=tet b=tet
```

```
79 H    0.817796515100  0.655560099300 -0.999193779600  f=tet b=tet
80 H    0.490420451600 -3.492640386000 -1.131363333000  f=tet b=tet
81 H    0.500481953100 -3.745478774000  1.933814485000  f=tet b=tet
82 H    1.202855664000 -4.919210699000  0.779385352100  f=tet b=tet
END
```

10,10a-dihydro pyranopterin

```
ATOMS
1 N   -2.771643984000 -3.482777052000 -0.881979422500  f=pterin b=pterin
2 N   -0.604058642300 -1.828979276000 -0.506235968200  f=pterin b=pterin
3 C   -1.884636630000 -1.384407585000 -0.335996359400  f=pterin b=pterin
4 C   -3.004156015000 -2.203633979000 -0.500274721800  f=pterin b=pterin
5 C   -0.217782890400 -5.901104275000 -0.798682393600  f=pterin b=pterin
6 C    0.946688972200 -5.055389121000 -1.228438539000  f=pterin b=pterin
7 C    0.918006152300 -3.653590754000 -1.098897812000  f=pterin b=pterin
8 C   -0.383450534500 -3.070831590000 -0.849477673200  f=pterin b=pterin
9 C   -1.503783535000 -4.032396346000 -1.135200116000  f=pterin b=pterin
10 O   -1.35100024800  -5.18458254500  -0.325202827800  f=pterin b=pterin
11 C   -2.16037181800  -0.03278368466   0.046755731050  f=pterin b=pterin
12 N   -4.30404075100  -1.87811797200  -0.353787067800  f=pterin b=pterin
13 C    0.14602683030  -6.85248644800   0.308947164700  f=pterin b=pterin
14 S    2.25457925400  -6.00477171200  -1.832083274000  f=pterin b=pterin
15 S    2.30179911700  -2.63749696500  -1.320213541000  f=pterin b=pterin
16 N   -3.52912076600   0.21842572000   0.191922580200  f=pterin b=pterin
17 C   -4.57817811700  -0.63777098140   0.001284482619  f=pterin b=pterin
18 H   -3.76594627700   1.17723203500   0.461086971200  f=pterin b=pterin
19 S   -6.16553978600  -0.00127750094   0.244368790000  f=pterin b=pterin
20 H   -0.53367247560  -6.50626983900  -1.691174182000  f=pterin b=pterin
```

```
21 O   -1.37391596600   0.90004719450   0.258131725300  f=pterin b=pterin
22 H   -3.60850077200  -4.04812790200  -1.041690483000  f=pterin b=pterin
23 H   -0.71184717660  -7.50975663100   0.557249422500  f=pterin b=pterin
24 H   -1.42650042800  -4.38749323000  -2.197810050000  f=pterin b=pterin
25 H    0.42176970020  -6.24891943400   1.193970475000  f=pterin b=pterin
26 H    1.02655956200  -7.42360724300  -0.037049265150  f=pterin b=pterin
27 Au  -12.7935833000   -9.8814370200    0.321297689300  f=left b=left
28 Au  -12.7935843000   -7.3829580200   -1.121200306000  f=left b=left
29 Au  -12.7935843000   -7.3829580200    1.763795689000  f=left b=left
30 Au  -12.7935843000   -4.8844780200   -2.563698311000  f=left b=left
31 Au  -12.7935843000   -4.8844780200    0.321297689300  f=left b=left
32 Au  -12.7935843000   -4.8844780200    3.206293689000  f=left b=left
33 Au  -12.7935843000   -2.3859990210   -1.121200306000  f=left b=left
34 Au  -12.7935843000   -2.3859990210    1.763795689000  f=left b=left
35 Au  -12.7935843000    0.1124809804    0.321297689300  f=left b=left
36 Au  -10.4379953800   -8.2157840200    0.321297689300  f=left b=left
37 Au  -10.4379953800   -5.7173050200   -1.121200306000  f=left b=left
38 Au  -10.4379953800   -5.7173050200    1.763795689000  f=left b=left
39 Au  -10.4379953800   -3.2188250210   -2.563698311000  f=left b=left
40 Au  -10.4379953800   -3.2188250210    0.321297689300  f=left b=left
41 Au  -10.4379953800   -3.2188250210    3.206293689000  f=left b=left
42 Au  -10.4379953800   -0.7203450196   -1.121200306000  f=left b=left
43 Au  -10.4379953800   -0.7203450196    1.763795689000  f=left b=left
44 Au  -10.4379953800    1.7781339810    0.321297689300  f=left b=left
45 Au   -8.0824063750   -6.5501310200    0.321297689300  f=left b=left
46 Au   -8.0824063750   -4.0516510200   -1.121200306000  f=left b=left
47 Au   -8.0824063750   -4.0516510200    1.763795689000  f=left b=left
48 Au   -8.0824063750   -1.5531720220   -2.563698311000  f=left b=left
49 Au   -8.0824063750   -1.5531720220    0.321297689300  f=left b=left
50 Au   -8.0824063750   -1.5531720220    3.206293689000  f=left b=left
```

```
51 Au   -8.0824063750    0.9453079814   -1.121200306000  f=left b=left
52 Au   -8.0824063750    0.9453079814    1.763795689000  f=left b=left
53 Au   -8.0824073750    3.4437869810    0.321297689300  f=left b=left
54 Au    6.7399439420   -0.2189329410    0.007847577000  f=right b=right
55 Au    6.7865335040    2.2659563190   -1.457195957000  f=right b=right
56 Au    8.9507980890   -6.1138597510   -1.398554426000  f=right b=right
57 Au    8.9973876990   -3.6289694920   -2.863597980000  f=right b=right
58 Au    9.0185946490   -3.6033046370    0.021205912000  f=right b=right
59 Au    9.0439772590   -1.1440802310   -4.328641520000  f=right b=right
60 Au    9.0651842090   -1.1184153760   -1.443837622000  f=right b=right
61 Au    9.0863911590   -1.0927505200    1.440966266000  f=right b=right
62 Au    9.1117737990    1.3664748840   -2.908881176000  f=right b=right
63 Au    9.1329807490    1.3921397390   -0.024077283000  f=right b=right
64 Au    9.1795693090    3.8770290220   -1.489120810000  f=right b=right
65 Au    6.7187369920   -0.2445977960   -2.876956316000  f=right b=right
66 Au    4.1647255190   -9.3360051320   -1.334704714000  f=right b=right
67 Au    4.2113140820   -6.8511158500   -2.799748252000  f=right b=right
68 Au    4.2325210320   -6.8254509940    0.085055641000  f=right b=right
69 Au    4.2579036660   -4.3662255900   -4.264791801000  f=right b=right
70 Au    4.2791106170   -4.3405607350   -1.379987902000  f=right b=right
71 Au    4.3003175670   -4.3148958790    1.504815985000  f=right b=right
72 Au    4.3257001790   -1.8556714760   -2.845031447000  f=right b=right
73 Au    4.3469071290   -1.8300066210    0.039772445000  f=right b=right
74 Au    4.3934967140    0.6548836400   -1.425271098000  f=right b=right
75 Au    6.5577613100   -7.7249324310   -1.366629567000  f=right b=right
76 Au    6.6043508720   -5.2400431710   -2.831673112000  f=right b=right
77 Au    6.6255578220   -5.2143783150    0.053130781000  f=right b=right
78 Au    6.6509404570   -2.7551529130   -4.296716661000  f=right b=right
79 Au    6.6721474070   -2.7294880570   -1.411912762000  f=right b=right
80 Au    6.6933543570   -2.7038232020    1.472891125000  f=right b=right
```

```
END
```

Quinonoid pyranopterin

```
ATOMS
1 Au  -11.59952243000 -8.175169677000  2.896588954000  f=left b=left
2 Au  -11.49118977000 -5.675454951000  1.460314237000  f=left b=left
3 Au  -11.56478581000 -5.679988533000  4.344367328000  f=left b=left
4 Au  -11.38285740000 -3.175739742000  0.024038695920  f=left b=left
5 Au  -11.45645345000 -3.180273325000  2.908091787000  f=left b=left
6 Au  -11.53004900000 -3.184806089000  5.792145181000  f=left b=left
7 Au  -11.34812059000 -0.680557297600  1.471816549000  f=left b=left
8 Au  -11.42171664000 -0.685090880100  4.355869640000  f=left b=left
9 Au  -11.31338427000  1.814624328000  2.919594099000  f=left b=left
10 Au   -9.1979760510  -6.57776457900   2.960383352000  f=left b=left
11 Au   -9.0896436850  -4.07804937000   1.524107811000  f=left b=left
12 Au   -9.1632392420  -4.08258213400   4.408161204000  f=left b=left
13 Au   -8.9813108310  -1.57833334300   0.087832572800  f=left b=left
14 Au   -9.0549068760  -1.58286692600   2.971885664000  f=left b=left
15 Au   -9.1285029210  -1.58740050800   5.855938755000  f=left b=left
16 Au   -8.9465745100   0.91684828280   1.535610123000  f=left b=left
17 Au   -9.0201700680   0.91231551920   4.419663517000  f=left b=left
18 Au   -8.9118377020   3.41203072800   2.983387976000  f=left b=left
19 Au   -6.7964294810  -4.98035818000   3.024177228000  f=left b=left
20 Au   -6.6880971150  -2.48064297100   1.587901688000  f=left b=left
21 Au   -6.7616931600  -2.48517655400   4.471954779000  f=left b=left
22 Au   -6.5797647490   0.01907223732   0.151626147200  f=left b=left
23 Au   -6.6533603060   0.01453947375   3.035679541000  f=left b=left
24 Au   -6.7269563510   0.01000589116   5.919732632000  f=left b=left
25 Au   -6.5450279400   2.51425468200   1.599404000000  f=left b=left
```

```
26 Au   -6.6186239860   2.50972110000   4.483457091000  f=left b=left
27 Au   -6.5102913210   5.00943582600   3.047182374000  f=left b=left
28 Au    7.8260309380   2.48184705300   1.460699786000  f=right b=right
29 Au    7.8726205020   4.96673631300  -0.004343753982  f=right b=right
30 Au   10.0368850900  -3.41307975900   0.054297777900  f=right b=right
31 Au   10.0834746800  -0.92818949980  -1.410745771000  f=right b=right
32 Au   10.1046816300  -0.90252464430   1.474058122000  f=right b=right
33 Au   10.1300642400   1.55669976000  -2.875789310000  f=right b=right
34 Au   10.1512711900   1.58236461500   0.009014582599  f=right b=right
35 Au   10.1724781400   1.60802947100   2.893818476000  f=right b=right
36 Au   10.1978607800   4.06725487500  -1.456028966000  f=right b=right
37 Au   10.2190677300   4.09291973000   1.428774927000  f=right b=right
38 Au   10.2656562900   6.57780901300  -0.036268605550  f=right b=right
39 Au    7.8048239890   2.45618219800  -1.424104107000  f=right b=right
40 Au    5.2508125090  -6.63522513700   0.118147488200  f=right b=right
41 Au    5.2974010740  -4.15033585400  -1.346896044000  f=right b=right
42 Au    5.3186080230  -4.12467099800   1.537907849000  f=right b=right
43 Au    5.3439906610  -1.66544559400  -2.811939593000  f=right b=right
44 Au    5.3651976100  -1.63978073900   0.072864300030  f=right b=right
45 Au    5.3864045590  -1.61411588300   2.957668193000  f=right b=right
46 Au    5.4117871750   0.84510852080  -1.392179240000  f=right b=right
47 Au    5.4329941240   0.87077337630   1.492624653000  f=right b=right
48 Au    5.4795837110   3.35566363600   0.027581104740  f=right b=right
49 Au    7.6438483010  -5.02415243600   0.086222636610  f=right b=right
50 Au    7.6904378650  -2.53926317700  -1.378820903000  f=right b=right
51 Au    7.7116448140  -2.51359832100   1.505982990000  f=right b=right
52 Au    7.7370274530  -0.05437291722  -2.843864452000  f=right b=right
53 Au    7.7582344020  -0.02870806175   0.040939441320  f=right b=right
54 Au    7.7794413510  -0.00304320628   2.925743334000  f=right b=right
55 N    -1.66345287400 -0.259903026800 -0.295770742000  f=ppd b=ppd
```

```
56 N    0.49244797880  0.397012565600  1.398489986000  f=ppd b=ppd
57 C   -0.75239944920  0.572006426600  1.762306347000  f=ppd b=ppd
58 C   -1.89876670100  0.342287570600  0.895503735800  f=ppd b=ppd
59 C    0.60878000480 -3.055920767000  0.120082934800  f=ppd b=ppd
60 C    1.94743366500 -2.331233074000  0.158114338800  f=ppd b=ppd
61 C    2.00882876000 -0.947474791800  0.125739150800  f=ppd b=ppd
62 C    0.72178071680 -0.144412194800  0.063271273800  f=ppd b=ppd
63 C   -0.42948240820 -0.987058060000 -0.459318155000  f=ppd b=ppd
64 O   -0.53430844320 -2.185777028000  0.304739505800  f=ppd b=ppd
65 C   -1.05741641300  1.111481467000  3.118892384000  f=ppd b=ppd
66 N   -3.12913786200  0.714422542600  1.205270300000  f=ppd b=ppd
67 C    0.45312182680 -4.129645615000  1.184471588000  f=ppd b=ppd
68 S    3.33931849700 -3.380307008000  0.052864360800  f=ppd b=ppd
69 S    3.45192093700  0.029490722010  0.113691280800  f=ppd b=ppd
70 N   -2.33802282600  1.499150672000  3.379215599000  f=ppd b=ppd
71 C   -3.26546035400  1.309271721000  2.432853860000  f=ppd b=ppd
72 H    0.86995155480  0.704648172600 -0.632134262000  f=ppd b=ppd
73 S   -4.88211633300  1.843029890000  2.792194453000  f=ppd b=ppd
74 H    0.51546314480 -3.525895889000 -0.882623758000  f=ppd b=ppd
75 O   -0.15230939520  1.228846890000  3.975937725000  f=ppd b=ppd
76 H   -2.48440640300 -0.580774121800 -0.818741386000  f=ppd b=ppd
77 H   -0.54023913820 -4.594986026000 1.094747486000  f=ppd b=ppd
78 H   -0.29543748120 -1.212650922000 -1.530324796000  f=ppd b=ppd
79 H    0.54926899380 -3.674541149000 2.183185803000  f=ppd b=ppd
80 H    1.22791078900 -4.895149872000 1.065118393000  f=ppd b=ppd
END
```

B.1 References

(1) Larsson, J. A.; Nolan, M.; Greer, J. C. *J. Phys. Chem. B* **2002**, *106*, 5931–5937, DOI: 10.1021/jp014483k.

(2) Velde, G. T.; Bickelhaupt, F. M.; Baerends, E. J.; Guerra, C. F.; Van Gisbergen, S. J. A.; Snijders, J. G.; Ziegler, T. *J. Comput. Chem.* **2001**, *22*, 931–967.

(3) Seldenthuis, J. S. Electrical and Mechanical Effects in Single-Molecule Junctions., Ph.D. Thesis, Delft, Netherlands, 2011.

Appendix C

CASSCF/NEVPT2 Calculations with ORCA

To correct for any excitations not described by the active space (dynamic correlation), ORCA provides the n-electron valence perturbation theory (NEVPT2) method which is quite powerful at correcting the energies of CASSCF states. With these methods, results can be achieved which rival that of very expensive MRCI calculations. For example, the spectra shown in Figure C.1 were calculated with the powerful SORCI method and NEVPT2. The SORCI calculation took several weeks while the NEVPT2 calculation only needed 6 hours, yet the results are extremely similar[1].

To perform a CASSCF calculation in ORCA there are several steps involved:

- Calculation of an appropriate set of starting orbitals.

[1]The SORCI method is very sensitive to even small terms in the CI expansion, necessitating large active spaces to capture nearly every excited configuration. CASSCF and NEVPT2 only needs the orbitals necessary to describe the leading terms (>10-20%) of the wavefunction.

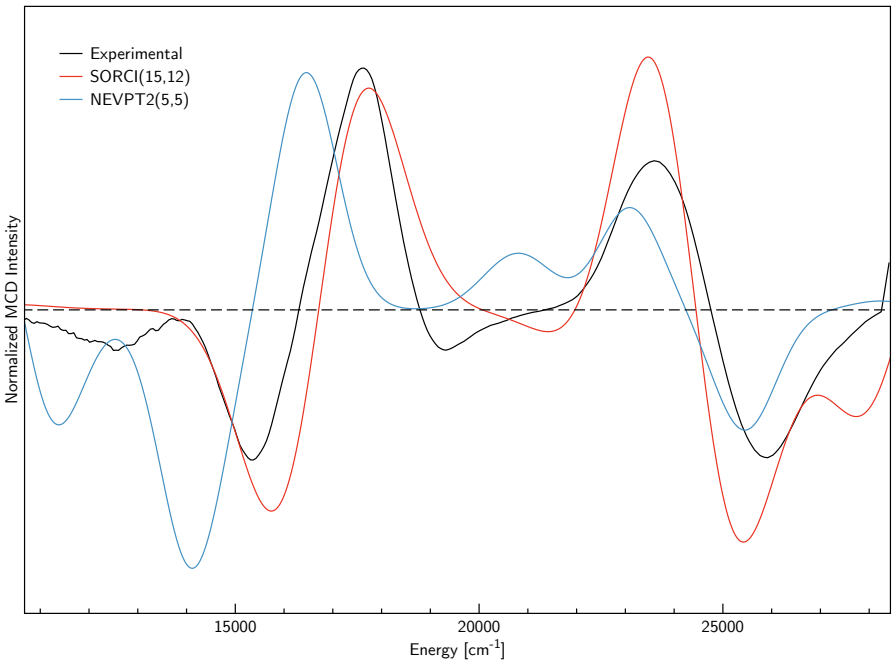

Figure C.1: Experimental and calculated MCD spectra of the high-g split DMSOr intermediate. Experimental and SORCI spectra published in[1].

- Examination of the starting orbitals to determine which are needed in the active space.
- CASSCF calculation with the starting orbitals[2].

The starting orbitals are typically taken from a DFT calculation. Open-shell molecules must have some sort of restricted set of orbitals created, and ORCA can generate a wide variety of these. The quasi-restricted orbitals (QROs) are useful in that the occupation numbers are integer values, whereas the unrestricted natural orbitals (UNOs) often have fractional numbers, complicating the interpretation. To

[2]Often beginning with the desired active space results in poor convergence issues. An initial CASSCF calculation with a smaller active space often provides excellent starting orbitals for a larger calculation.

generate the QROs and UNOs, the keyword UNO must be in the input file. An example is given below:

```
!PBE UNO def2-TZVP def2-TZVP/J ZORA/RI NRSCF

%pal
nprocs 32
end

%method
SpecialGridAtoms 42
SpecialGridIntAcc 14
end

%output
Print[ P_ReducedOrbPopMO_L] 1
Print[ P_FragPopMO_L ] 1
Print[P_UNO_OccNum] = 1;
Print[P_UNO_ReducedOrbPopMO_L] = 1;
Print[P_UNO_AtPopMO_L] =1;
end

%rel
OneCenter true
end

* xyz -1 2
Mo(1)       0.038961      0.007731      0.016748
```

```
S(2)        1.331288     -1.770168      0.977452
S(2)       -0.511276     -1.778039     -1.498356
C(2)        1.114030     -3.245185      0.077213
C(2)        0.307047     -3.243159     -1.021618
C(2)        0.008608     -4.433822     -1.893882
H(2)        0.536397     -5.337912     -1.560889
H(2)       -1.071500     -4.653597     -1.902494
H(2)        0.298785     -4.238458     -2.939017
C(2)        1.853706     -4.436104      0.627626
H(2)        1.685125     -5.342688      0.029841
H(2)        2.939763     -4.248503      0.658428
H(2)        1.539753     -4.649455      1.662186
S(3)       -1.724118      1.033040     -1.216180
S(3)       -1.665341     -0.178644      1.640015
C(3)       -3.220291      0.814639     -0.339766
C(3)       -3.187017      0.279080      0.912963
C(3)       -4.457494      1.240090     -1.083677
H(3)       -5.348268      1.251400     -0.439840
H(3)       -4.330891      2.249780     -1.505498
H(3)       -4.661608      0.565241     -1.931037
C(3)       -4.389000      0.024973      1.782975
H(3)       -5.300451      0.486984      1.379964
H(3)       -4.576614     -1.055712      1.893226
H(3)       -4.223190      0.422953      2.796165
O(4)        1.093144      0.986406      1.400516
H(4)        1.973172      1.175342      1.025386
O(5)        1.145306      1.063099     -1.247333
C(5)        1.317330      2.444886     -1.295942
```

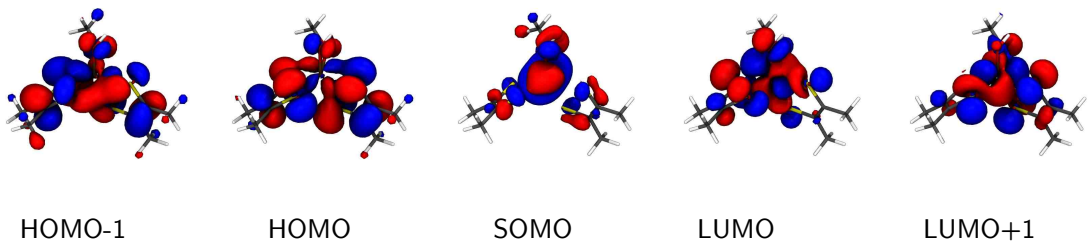

Figure C.2: Active space orbitals for the high-g split DMSOr intermediate.

```
H(5)        1.476395      2.887724      -0.290997
H(5)        2.194653      2.687492      -1.927159
H(5)        0.428865      2.946549      -1.732480
*
```

This will generate a `.qro` file which can be read into a subsequent job for population analysis or plotted with the `orca_plot` utility. From the QROs 5 frontier orbitals were selected, shown in Figure 4.2. With these active space orbitals a CASSCF/NEVPT2 calculation was performed with the following input file, which results in the calculation of the MCD spectra shown in Figure C.1. Note that CASSCF calculations are often very difficult to converge, and so there are many options described in the ORCA manual which help with these problems. It is strongly recommended to read the CASSCF sections throughly if any issues are encountered.

```
! MORead RHF AllowRHF RIJCOSX RI-NEVPT2 ZORA/RI def2-TZVP def2-TZVP/C

%pal
    nprocs 2
end
```

```
%moinp "epr.qro"

%casscf
    nel 5
    norb 5
    mult 2
    nroots 20
    nevpt2 true
    nev_canonstep 1
    trafostep rimo
    switchstep diis
    maxiter 200
    switchiter 25
    rel
        dosoc true
        gtensor true
        ndoubgtensor 1
        printlevel 5
uv true
mcd true
B 50000
Temperature 5
    end
end

%maxcore 2000

* xyz -1 2
```

Mo(1)	0.038961	0.007731	0.016748
S(2)	1.331288	-1.770168	0.977452
S(2)	-0.511276	-1.778039	-1.498356
C(2)	1.114030	-3.245185	0.077213
C(2)	0.307047	-3.243159	-1.021618
C(2)	0.008608	-4.433822	-1.893882
H(2)	0.536397	-5.337912	-1.560889
H(2)	-1.071500	-4.653597	-1.902494
H(2)	0.298785	-4.238458	-2.939017
C(2)	1.853706	-4.436104	0.627626
H(2)	1.685125	-5.342688	0.029841
H(2)	2.939763	-4.248503	0.658428
H(2)	1.539753	-4.649455	1.662186
S(3)	-1.724118	1.033040	-1.216180
S(3)	-1.665341	-0.178644	1.640015
C(3)	-3.220291	0.814639	-0.339766
C(3)	-3.187017	0.279080	0.912963
C(3)	-4.457494	1.240090	-1.083677
H(3)	-5.348268	1.251400	-0.439840
H(3)	-4.330891	2.249780	-1.505498
H(3)	-4.661608	0.565241	-1.931037
C(3)	-4.389000	0.024973	1.782975
H(3)	-5.300451	0.486984	1.379964
H(3)	-4.576614	-1.055712	1.893226
H(3)	-4.223190	0.422953	2.796165
O(4)	1.093144	0.986406	1.400516
H(4)	1.973172	1.175342	1.025386
O(5)	1.145306	1.063099	-1.247333

```
C(5)        1.317330      2.444886     -1.295942
H(5)        1.476395      2.887724     -0.290997
H(5)        2.194653      2.687492     -1.927159
H(5)        0.428865      2.946549     -1.732480
*
```

Appendix D

Derivation of 3-Spin 2-J MCD Equations and other SI

Here are presented the full derivations are provided for all of the matrix elements and MCD intensity expressions given in Chapter 4. First, the eigenvectors of the S_1, T_1, S_2, T_2 states are given, followed by the dipole matrix elements between the ground state and all of the above excited states. The overall derivation is based upon that given by Westphal et. Al[1], however several errors were corrected and the nature of state mixing was recast in terms of a three-spin HDvV Hamiltonian[2]. Also given are the details of the CASSCF calculations, including orbital diagrams and calculated spectra.

D.1 Derivation of MCD Equations

For all of the following, we will use the following spin-coupled states, which are eigenvectors of S^2 and S_z[3]:

$$|S_0, {}^1\!/_2\rangle = \left|\phi_{H-1}\overline{\phi_{H-1}}\phi_H\overline{\phi_H}\phi_{NN}\right| \tag{D.1a}$$

$$|S_1, 1/2\rangle = 1/\sqrt{2}\left(\left|\phi_L\overline{\phi_H}\phi_{NN}\right| - \left|\overline{\phi_L}\phi_H\phi_{NN}\right|\right) \tag{D.1b}$$

$$|T_1, 1/2\rangle = 1/\sqrt{6}\left(\left|\phi_L\overline{\phi_H}\phi_{NN}\right| + \left|\overline{\phi_L}\phi_H\phi_{NN}\right| - 2\left|\phi_L\phi_H\overline{\phi_{NN}}\right|\right) \tag{D.1c}$$

$$|S_2, 1/2\rangle = 1/\sqrt{2}\left(\left|\phi_L\overline{\phi_{H-1}}\phi_{NN}\right| - \left|\overline{\phi_L}\phi_{H-1}\phi_{NN}\right|\right) \tag{D.1d}$$

$$|T_2, 1/2\rangle = 1/\sqrt{6}\left(\left|\phi_L\overline{\phi_{H-1}}\phi_{NN}\right| + \left|\overline{\phi_L}\phi_{H-1}\phi_{NN}\right| - 2\left|\phi_L\phi_{H-1}\overline{\phi_{NN}}\right|\right) \tag{D.1e}$$

D.1.1 Dipole and Spin-Orbit Matrix Elements

These states allow for the determination of the dipole matrix elements, D^{AJ},

$$\begin{aligned}
\langle S_0 \left|\overrightarrow{r}\right| S_1, 1/2\rangle = D^{S_0,S_1} &= \frac{1}{\sqrt{2}}\left\langle \phi_H\overline{\phi_H}\phi_{NN}\left|\overrightarrow{r}\right|\left(\phi_L\overline{\phi_H}\phi_{NN} - \overline{\phi_L}\phi_H\phi_{NN}\right)\right\rangle \\
&= \frac{1}{\sqrt{2}}\left[\langle\phi_H\left|\overrightarrow{r}\right|\phi_L\rangle - \left\langle\phi_H\overline{\phi_H}\phi_{NN}\left|\overrightarrow{r}\right|\overline{\phi_L}\phi_H\phi_{NN}\right\rangle\right] \\
&= \left[\langle\phi_H\left|\overrightarrow{r}\right|\phi_L\rangle + \left\langle\phi_H\overline{\phi_H}\phi_{NN}\left|\overrightarrow{r}\right|\phi_H\overline{\phi_L}\phi_{NN}\right\rangle\right] \\
&= \sqrt{2}\,\langle\phi_H\left|\overrightarrow{r}\right|\phi_L\rangle \\
&= \sqrt{2}\,d^{H,L}
\end{aligned} \tag{D.2}$$

where the swapping property of determinants, $|A| = -|B|$, where B and A differ by the order of one (or any odd number of) column(s), was used. To express the state matrix elements in terms of single orbital matrix elements, the Slater-Condon rules[4] were used. The single orbital matrix elements are vastly easier to handle, not only computationally, but they can also be evaluated graphically to determine the relative signs of the transition dipoles and spin-orbit vectors. Similarly, the remainder of the dipole matrix elements are:

$$\begin{aligned}
\langle S_0 \left|\overrightarrow{r}\right| S_2, 1/2\rangle &= \frac{1}{\sqrt{2}}\left\langle \phi_{H-1}\overline{\phi_{H-1}}\phi_{NN}\left|\overrightarrow{r}\right|\left(\phi_L\overline{\phi_{H-1}}\phi_{NN} - \overline{\phi_L}\phi_{H-1}\phi_{NN}\right)\right\rangle \\
&= \left[\langle\phi_{H-1}\left|\overrightarrow{r}\right|\phi_L\rangle + \left\langle\phi_{H-1}\overline{\phi_{H-1}}\phi_{NN}\left|\overrightarrow{r}\right|\phi_{H-1}\overline{\phi_L}\phi_{NN}\right\rangle\right] \\
&= \sqrt{2}\,\langle\phi_{H-1}\left|\overrightarrow{r}\right|\phi_L\rangle \\
&= \sqrt{2}\,d^{H-1,L}
\end{aligned} \tag{D.3}$$

$$\begin{aligned}
\langle S_0 \,|\, \overrightarrow{r} \,|\, T_1, {}^1\!/_2 \rangle &= \frac{1}{\sqrt{6}} \left\langle \phi_H \overline{\phi_H} \phi_{NN} \,|\, \overrightarrow{r} \,|\, \phi_L \overline{\phi_H} \phi_{NN} + \right. \\
&\quad \left. \overline{\phi_L} \phi_H \phi_{NN} - 2\phi_L \phi_H \overline{\phi_{NN}} \right\rangle \\
&= \frac{1}{\sqrt{6}} \left[\langle \phi_H \,|\, \overrightarrow{r} \,|\, \phi_L \rangle - \langle \phi_H \,|\, \overrightarrow{r} \,|\, \phi_L \rangle - \right. \\
&\quad \left. 2 \left\langle \phi_H \overline{\phi_H} \,|\, \overrightarrow{r} \,|\, \phi_L \phi_H \overline{\phi}_{NN} \right\rangle \right] \\
&= \frac{1}{\sqrt{6}} \left[0 - 2 \times 0 \right] \\
&= 0
\end{aligned} \tag{D.4}$$

$$\begin{aligned}
\langle S_0 \,|\, \overrightarrow{r} \,|\, T_2, {}^1\!/_2 \rangle &= \frac{1}{\sqrt{6}} \left\langle \phi_{H-1} \overline{\phi_{H-1}} \phi_{NN} \,|\, \overrightarrow{r} \,|\, \phi_L \overline{\phi_{H-1}} \phi_{NN} + \right. \\
&\quad \left. \overline{\phi_L} \phi_{H-1} \phi_{NN} - 2\phi_L \phi_{H-1} \overline{\phi_{NN}} \right\rangle \\
&= \frac{1}{\sqrt{6}} \left[\langle \phi_{H-1} \,|\, \overrightarrow{r} \,|\, \phi_L \rangle - \langle \phi_{H-1} \,|\, \overrightarrow{r} \,|\, \phi_L \rangle - \right. \\
&\quad \left. 2 \left\langle \phi_{H-1} \overline{\phi_{H-1}} \,|\, \overrightarrow{r} \,|\, \phi_L \phi_{H-1} \overline{\phi}_{NN} \right\rangle \right] \\
&= \frac{1}{\sqrt{6}} \left[0 - 2 \times 0 \right] \\
&= 0
\end{aligned} \tag{D.5}$$

An important fact to note here that the zero'th order trip-doublet states have strictly *zero* dipole intensity. This is simply understood as the transition to a triplet state is a spin-forbidden transition, and the presence of a pendant radical does not change this fact. When exchange mixing is taken into account (*vide infra*) we will see how this restriction will be lifted.

Next, the spin-orbital matrix elements can be derived in a manner identical to that of the transition dipoles above. First, we see that the spin-orbit between sing-

doublet states is zero[1]:

$$\begin{aligned}
\langle S_1, 1/2 \,|l \cdot s|\, S_2, 1/2\rangle = & \\
& \frac{1}{2}\Big[\langle \phi_L\bar{\phi}_H\phi_{NN} - \bar{\phi}_L\phi_H\phi_{NN}|\hat{l}_z \cdot \hat{s}_z \\
& \quad |\phi_L\bar{\phi}_{H-1}\phi_{NN} - \bar{\phi}_L\phi_{H-1}\phi_{NN}\rangle\Big] \\
= & \frac{1}{2}\Big[\left\langle \phi_L\bar{\phi}_H\phi_{NN}\left|\hat{l}_z \cdot \hat{s}_z\right|\phi_L\bar{\phi}_{H-1}\phi_{NN}\right\rangle - \\
& \left\langle \phi_L\bar{\phi}_H\phi_{NN}\left|\hat{l}_\alpha \cdot \hat{s}_\alpha\right|\bar{\phi}_L\phi_{H-1}\phi_{NN}\right\rangle - \\
& \left\langle \bar{\phi}_L\phi_H\phi_{NN}\left|\hat{l}_\alpha \cdot \hat{s}_\alpha\right|\phi_L\bar{\phi}_{H-1}\phi_{NN}\right\rangle + \\
& \left\langle \bar{\phi}_L\phi_H\phi_{NN}\left|\hat{l}_z \cdot \hat{s}_z\right|\bar{\phi}_L\phi_{H-1}\phi_{NN}\right\rangle\Big] \\
= & \frac{1}{2}\left[\left\langle \bar{\phi}_H\left|\hat{l}_z \cdot \hat{s}_z\right|\bar{\phi}_{H-1}\right\rangle - 0 - 0 + \left\langle \phi_H\left|\hat{l}_z \cdot \hat{s}_z\right|\phi_{H-1}\right\rangle\right] \\
= & \frac{1}{2}\left[-\frac{1}{2}\left\langle \bar{\phi}_H\left|\hat{l}_z\right|\bar{\phi}_{H-1}\right\rangle + \frac{1}{2}\left\langle \phi_H\left|\hat{l}_z\right|\phi_{H-1}\right\rangle\right] = 0
\end{aligned} \tag{D.6}$$

while spin-orbit coupling involving at least one trip-doublet state has no such restriction:

$$\begin{aligned}
\langle T_1, 1/2 \,|l \cdot s|\, S_2, 1/2\rangle = & \\
& L_z^{T_1S_2} \\
= & \frac{1}{\sqrt{12}}\Big[\langle \phi_L\bar{\phi}_H\phi_{NN} + \bar{\phi}_L\phi_H\phi_{NN} - \phi_L\phi_H\bar{\phi}_{NN}|\hat{l}_z \cdot \hat{s}_z| \\
& \quad |\phi_L\bar{\phi}_{H-1}\phi_{NN} - \bar{\phi}_L\phi_{H-1}\phi_{NN}\rangle\Big] \\
= & \frac{1}{\sqrt{12}}\left[\left\langle \bar{\phi}_H\left|\hat{l}_z \cdot \hat{s}_z\right|\bar{\phi}_{H-1}\right\rangle - \left\langle \phi_H\left|\hat{l}_z \cdot \hat{s}_z\right|\phi_{H-1}\right\rangle\right] \\
= & \frac{-1}{\sqrt{12}}\left\langle \phi_H\left|\hat{l}_z\right|\phi_{H-1}\right\rangle
\end{aligned} \tag{D.7}$$

$$\langle S_1, 1/2 \,|l \cdot s|\, T_2, 1/2\rangle =$$

[1]For all the following equations, any matrix element of the type $\left\langle \phi_a\left|\hat{l} \cdot \hat{s}\right|\phi_b\right\rangle$ implies the imaginary part of the matrix element, $Im\left(\left\langle \phi_a\left|\hat{l} \cdot \hat{s}\right|\phi_b\right\rangle\right)$. This has been omitted for clarity.

$$\frac{1}{\sqrt{12}}\Big[\langle\phi_L\bar{\phi}_H\phi_{NN} - \bar{\phi}_L\phi_H\phi_{NN}|\hat{l}_z\cdot\hat{s}_z| \\ |\phi_L\bar{\phi}_{H-1}\phi_{NN} + \bar{\phi}_L\phi_{H-1}\phi_{NN} - 2\phi_L\phi_{H-1}\bar{\phi}_{NN}\rangle\Big] = \\ \frac{1}{\sqrt{12}}\left[\left\langle\bar{\phi}_H\left|\hat{l}_z\cdot\hat{s}_z\right|\bar{\phi}_{H-1}\right\rangle - \left\langle\phi_H\left|\hat{l}_z\cdot\hat{s}_z\right|\phi_{H-1}\right\rangle\right] = \\ \frac{-1}{\sqrt{12}}\left\langle\phi_H\left|\hat{l}_z\right|\phi_{H-1}\right\rangle \tag{D.8}$$

$$\langle T_1,{}^1\!/_2\,|l\cdot s|\,T_2,{}^1\!/_2\rangle = \\ \frac{1}{6}\Big[\langle\phi_L\bar{\phi}_H\phi_{NN} + \bar{\phi}_L\phi_H\phi_{NN} - 2\phi_L\phi_H\bar{\phi}_{NN}|\hat{l}_z\cdot\hat{s}_z| \\ |\phi_L\bar{\phi}_{H-1}\phi_{NN} + \bar{\phi}_L\phi_{H-1}\phi_{NN} - 2\phi_L\phi_{H-1}\bar{\phi}_{NN}\rangle\Big] = \\ \frac{1}{6}\left[\left\langle\bar{\phi}_H\left|\hat{l}_z\cdot\hat{s}_z\right|\bar{\phi}_{H-1}\right\rangle + \left\langle\phi_H\left|\hat{l}_z\cdot\hat{s}_z\right|\phi_{H-1}\right\rangle + \right. \\ \left. 4\left\langle\phi_H\left|\hat{l}_z\cdot\hat{s}_z\right|\phi_{H-1}\right\rangle\right] \\ = \frac{1}{3}\left\langle\phi_H\left|\hat{l}_z\right|\phi_{H-1}\right\rangle \tag{D.9}$$

A few points are useful to note here: 1) the trip-doublet/trip-doublet coupling has an opposite sign as compared to the sing-doublet/trip-doublet matrix elements, which has strong implications as the overall C-term sign in the MCD experiment is proportional to the spin-orbit matrix element. Secondly, unlike the dipole matrix elements, the spin-orbit elements change sign upon reversal of the bra- and ket- states:

$$\langle T_1,{}^1\!/_2\,|l\cdot s|\,T_2,{}^1\!/_2\rangle = -\langle T_2,{}^1\!/_2\,|l\cdot s|\,T_1,{}^1\!/_2\rangle \tag{D.10}$$

however, this can be easily circumvented[2] when the orbital matrix elements are used (simply reverse the orbital bra- and ket-):

$$\langle T_1,{}^1\!/_2\,|l\cdot s|\,T_2,{}^1\!/_2\rangle = \frac{1}{3}\left\langle\phi_H\left|\hat{l}_z\right|\phi_{H-1}\right\rangle \tag{D.11}$$

$$\langle T_2,{}^1\!/_2\,|l\cdot s|\,T_1,{}^1\!/_2\rangle = \frac{1}{3}\left\langle\phi_{H-1}\left|\hat{l}_z\right|\phi_H\right\rangle \tag{D.12}$$

[2]This is very useful when dealing with MCD calculations, as the misplacement of a single negative sign can cause no end of problems!

D.1.2 Effect of Exchange Mixing on Matrix Elements

When the exchange mixing, J, is taken into account the states given in Equation (D.1a) are now mixed:

$$|T_1', 1/2\rangle = cos\lambda\,|T_1, 1/2\rangle + sin\lambda\,|S_1, 1/2\rangle \tag{D.13}$$

$$|S_1', 1/2\rangle = cos\lambda\,|S_1, 1/2\rangle - sin\lambda\,|T_1, 1/2\rangle \tag{D.14}$$

where λ is the mixing coefficient:

$$\lambda = 1/2\; Tan^{-1}\left(\frac{\sqrt{3}J}{2J' - J}\right) \tag{D.15}$$

Combining the above equations, matrix elements between the exchange mixed states can be easily derived:

$$\begin{aligned} D_\alpha^{S_0 S_1'} &= \langle S_0|\overrightarrow{r}_\alpha\,(cos\lambda|S_1, 1/2\rangle - sin\lambda|T_1, 1/2\rangle) \\ &= cos\lambda\; D_\alpha^{S_0 S_1} \end{aligned} \tag{D.16}$$

$$\begin{aligned} D_\alpha^{S_0 T_1'} &= \langle S_0|\overrightarrow{r}_\alpha\,(cos\lambda|T_1, 1/2\rangle + sin\lambda|S_1, 1/2\rangle) \\ &= sin\lambda\; D_\alpha^{S_0 S_1} \end{aligned} \tag{D.17}$$

$$\begin{aligned} D_\alpha^{S_0 S_2'} &= \langle S_0|\overrightarrow{r}_\alpha\,(cos\lambda|S_2, 1/2\rangle - sin\lambda|T_2, 1/2\rangle) \\ &= cos\lambda\; D_\alpha^{S_0 S_2} \end{aligned} \tag{D.18}$$

$$\begin{aligned} D_\alpha^{S_0 T_2'} &= \langle S_0|\overrightarrow{r}_\alpha\,(cos\lambda|T_2, 1/2\rangle + sin\lambda|S_2, 1/2\rangle) \\ &= sin\lambda\; D_\alpha^{S_0 S_2} \end{aligned} \tag{D.19}$$

$$\begin{aligned} L_z^{T_2' S_1'} &= (cos\lambda\langle T_2, 1/2| + sin\lambda\langle S_2, 1/2|)\,\hat{l}_z \cdot \hat{s}_z\,(cos\lambda|S_1, 1/2\rangle - sin\lambda|T_1, 1/2\rangle) \\ &= \cancelto{1}{cos^2\lambda}\, L_z^{T_2 S_1} - cos\lambda sin\lambda L_z^{T_2 T_1} + cos\lambda sin\lambda \cancelto{0}{L_z^{S_2 S_1}} - \cancelto{0}{sin^2\lambda}\, L_z^{T_2 S_1} \end{aligned}$$

$$
\begin{aligned}
&= L_z^{T_2S_1} - \lambda L_z^{T_2T_1} \\
&= -\frac{l_z^{H-1,H}}{\sqrt{12}} - l_z^{H-1,H}\frac{\lambda}{3} \\
&= -l_z^{H-1,H}\left(\frac{1}{\sqrt{12}} + \frac{\lambda}{3}\right) \\
&\approx \frac{-l_z^{H-1,H}}{\sqrt{12}}
\end{aligned} \tag{D.20}
$$

$$
\begin{aligned}
L_z^{S_2'S_1'} &= (cos\lambda\langle S_2, 1/2| - sin\lambda\langle T_2, 1/2|)\,\hat{l}_z \cdot \hat{s}_z\,(cos\lambda|S_1, 1/2\rangle - sin\lambda|T_1, 1/2\rangle) \\
&= cos^2\lambda \cancelto{0}{L_z^{S_2S_1}} - cos\lambda sin\lambda L_z^{S_2T_1} - cos\lambda sin\lambda L_z^{T_2S_1} + \cancelto{0}{sin^2\lambda} L_z^{T_2T_1} \\
&\approx -\lambda\left(L_z^{S_2T_1} + L_z^{T_2S_1}\right) \\
&= -\frac{\lambda}{\sqrt{12}}\left(-l_z^{H-1,H} - l_z^{H-1,H}\right) \\
&= \frac{2\lambda}{\sqrt{12}} l_z^{H-1,H}
\end{aligned} \tag{D.21}
$$

$$
\begin{aligned}
L_z^{T_2'T_1'} &= (cos\lambda\langle T_2, 1/2| + sin\lambda\langle S_2, 1/2|)\,\hat{l}_z \cdot \hat{s}_z\,(cos\lambda|T_1, 1/2\rangle + sin\lambda|S_1, 1/2\rangle) \\
&= \cancelto{1}{cos^2\lambda} L_z^{T_2T_1} + \lambda L_z^{T_2S_1} + \lambda L_z^{S_2T_1} + \cancelto{0}{sin^2\lambda L_z^{S_2S_1}} \\
&= L_z^{T_2S_1} + \lambda L_z^{T_2S_1} + \lambda L_z^{S_2T_1} \\
&= \frac{l_z^{H-1,H}}{3} - l_z^{H-1,H}\frac{2\lambda}{\sqrt{12}} \\
&= l_z^{H-1,H}\left(\frac{1}{3} - \frac{2\lambda}{\sqrt{12}}\right)
\end{aligned} \tag{D.22}
$$

$$
\begin{aligned}
L_z^{S_2'T_1'} &= (cos\lambda\langle S_2, 1/2| - sin\lambda\langle T_2, 1/2|)\,\hat{l}_z \cdot \hat{s}_z\,(cos\lambda|T_1, 1/2\rangle + sin\lambda|S_1, 1/2\rangle) \\
&= \cancelto{1}{cos^2\lambda} L_z^{S_2T_1} + cos\lambda sin\lambda \cancelto{0}{L_z^{S_2S_1}} - sin\lambda cos\lambda L_z^{T_2T_1} - \cancelto{0}{sin^2\lambda} L_z^{T_2T_1} \\
&= L_z^{S_2T_1} - \lambda L_z^{T_2T_1} \\
&= -\frac{1}{\sqrt{12}} l_z^{H-1,H} - \frac{\lambda}{3} l_z^{H-1,H} \\
&= -l_z^{H-1,H}\left(\frac{1}{\sqrt{12}} + \frac{\lambda}{3}\right)
\end{aligned}
$$

$$\approx \frac{-l_z^{H-1,H}}{\sqrt{12}} \tag{D.23}$$

D.1.3 MCD Intensity Expressions

With these fundamentals in place, we are now able to obtain our goal of deriving specific expressions for the MCD intensity. First, we will take the expression for MCD intensity derived by Neese and Solomon[5] and use the functions and matrix elements derived above. Several mathematical approximations will be made, namely that a) $sin^2\,\lambda = 0$, b) $cos^2\,\lambda = 1$, and c) $sin\,\lambda\,cos\,\lambda = \lambda$. These have been found to be good approximations when dealing with values of λ such as seen here. The equation for MCD intensity is a sum over excited states K:

$$C\left(A \to J\right) \propto -\sum_K \frac{\bar{L}_z^{KJ}}{\Delta_{KJ}} \left(D_x^{AK} D_y^{AJ} - D_y^{AK} D_x^{AJ}\right) \tag{D.24}$$

And so for $J = S_1'$ and $K = S_2', T_2'$ we have:

$$\begin{aligned}
C\left(S_0 \to S_1'\right) \propto & -\frac{\bar{L}_z^{T_2'S_1'}}{\Delta_{T_2'S_1'}} \left(\cancel{D_x^{S_0T_2'} D_y^{S_0S_1'}}^{\,0} - D_y^{S_0T_2'} D_x^{S_0S_1'}\right) \\
& -\frac{\bar{L}_z^{S_2'S_1'}}{\Delta_{S_2'S_1'}} \left(\cancel{D_x^{S_0S_2'} D_y^{S_0S_1'}}^{\,0} - D_y^{S_0S_2'} D_x^{S_0T_1'}\right) \\
& = \frac{\bar{L}_z^{T_2'S_1'}}{\Delta_{T_2'S_1'}} D_y^{S_0T_2'} D_x^{S_0S_1'} + \frac{\bar{L}_z^{S_2'S_1'}}{\Delta_{S_2'S_1'}} D_y^{S_0S_2'} D_x^{S_0S_1'} \\
& = \frac{\bar{L}_z^{T_2'S_1'}}{\Delta_{T_2'S_1'}} \left(sin\lambda D_y^{S_0S_2} cos\lambda D_x^{S_0S_1}\right) + \frac{\bar{L}_z^{S_2'S_1'}}{\Delta_{S_2'S_1'}} \left(\cancel{cos^2}^{\,1} \lambda D_y^{S_0S_2} D_x^{S_0S_1}\right) \\
& = \frac{\bar{L}_z^{T_2'S_1'}}{\Delta_{T_2'S_1'}} s\lambda c\lambda D_y^{S_0S_2} D_x^{S_0S_1} + \frac{\bar{L}_z^{S_2'S_1'}}{\Delta_{S_2'S_1'}} D_y^{S_0S_2} D_x^{S_0S_1} \\
& = -\frac{\lambda l_z^{H-1,H}}{\sqrt{12}\Delta_{T_2'S_1'}} D_y^{S_0S_2} D_x^{S_0S_1} + \frac{2\lambda l_z^{H-1,H}}{\sqrt{12}\Delta_{S_2'S_1'}} D_y^{S_0S_2} D_x^{S_0S_1} \\
& = \frac{\lambda l_z^{H-1,H} D_y^{S_0S_2} D_x^{S_0S_1}}{\sqrt{12}} \left(\frac{2}{\Delta_{S_2'S_1'}} - \frac{1}{\Delta_{T_2'S_1'}}\right)
\end{aligned} \tag{D.25}$$

$J = T_1'$ and $K = S_2', T_2'$:

$$\begin{aligned} C\left(S_0 \to T_1'\right) \propto & -\frac{\bar{L}_z^{T_2'T_1'}}{\Delta_{T_2'T_1'}}\left(\cancelto{0}{D_x^{S_0T_2'}D_y^{S_0T_1'}} - D_y^{S_0T_2'}D_x^{S_0T_1'}\right) \\ & -\frac{\bar{L}_z^{S_2'T_1'}}{\Delta_{S_2'T_1'}}\left(\cancelto{0}{D_x^{S_0S_2'}D_y^{S_0T_1'}} - D_y^{S_0S_2'}D_x^{S_0T_1'}\right) \\ = & \frac{\bar{L}_z^{T_2'T_1'}}{\Delta_{T_2'T_1'}}\cancelto{0}{sin^2\lambda}D_y^{S_0S_2}D_x^{S_0S_1} \\ & +\frac{\bar{L}_z^{S_2'T_1'}}{\Delta_{S_2'T_1'}}\lambda D_y^{S_0S_2}D_x^{S_0S_1} \\ = & \frac{-\lambda l_z^{H-1,H}}{\sqrt{12}\Delta_{S_2'T_1'}}D_y^{S_0S_2}D_x^{S_0S_1} \end{aligned} \tag{D.26}$$

$J = S_2'$ and $K = S_1', T_1'$:

$$\begin{aligned} C\left(S_0 \to S_2'\right) \propto & -\frac{\bar{L}_z^{T_1'S_2'}}{\Delta_{T_1'S_2'}}\left(D_x^{S_0T_1'}D_y^{S_0S_2'} - \cancelto{0}{D_y^{S_0T_1'}D_x^{S_0S_2'}}\right) \\ & -\frac{\bar{L}_z^{S_1'S_2'}}{\Delta_{S_1'S_2'}}\left(D_x^{S_0S_1'}D_y^{S_0S_2'} - \cancelto{0}{D_y^{S_0S_1'}D_x^{S_0S_2'}}\right) \\ = & \frac{\lambda l_z^{H,H-1}}{\sqrt{12}\Delta_{T_1'S_2'}}D_x^{S_0S_1}D_y^{S_0S_2} - \frac{2\lambda l_z^{H,H-1}}{\sqrt{12}\Delta_{S_1'S_2'}}D_x^{S_0S_1}D_y^{S_0S_2} \\ = & \frac{\lambda l_z^{H,H-1}D_x^{S_0S_1}D_y^{S_0S_2}}{\sqrt{12}}\left(\frac{1}{\Delta_{T_1'S_2'}} - \frac{2}{\Delta_{S_1'S_2'}}\right) \end{aligned} \tag{D.27}$$

To ease comparison between $C\left(S_0 \to S_1'\right)$ and $C\left(S_0 \to S_2'\right)$, this can be rewritten:

$$\begin{aligned} C\left(S_0 \to S_2'\right) \propto & \frac{\lambda l_z^{H,H-1}D_x^{S_0S_1}D_y^{S_0S_2}}{\sqrt{12}}\left(\frac{1}{\Delta_{T_1'S_2'}} - \frac{2}{\Delta_{S_1'S_2'}}\right) \\ = & -\frac{\lambda l_z^{H-1,H}D_x^{S_0S_1}D_y^{S_0S_2}}{\sqrt{12}}\left(\frac{1}{\Delta_{T_1'S_2'}} - \frac{2}{\Delta_{S_1'S_2'}}\right) \\ = & -\frac{\lambda l_z^{H-1,H}D_x^{S_0S_1}D_y^{S_0S_2}}{\sqrt{12}}\left(\frac{-1}{\Delta_{S_2'T_1'}} + \frac{2}{\Delta_{S_2'S_1'}}\right) \\ = & -\frac{\lambda l_z^{H-1,H}D_x^{S_0S_1}D_y^{S_0S_2}}{\sqrt{12}}\left(\frac{2}{\Delta_{S_2'S_1'}} - \frac{1}{\Delta_{S_2'T_1'}}\right) \end{aligned} \tag{D.28}$$

Finally, for $J = T_2'$ and $K = S_1', T_1'$ we have:

$$C\left(S_0 \to T_2'\right) \propto -\frac{\bar{L}_z^{S_1'T_2'}}{\Delta_{S_1'T_2'}}D_y^{S_0T_2'}D_x^{S_0S_1'}$$

$$
\begin{aligned}
&- \frac{\bar{L}_z^{T_1'T_2'}}{\Delta_{T_1'T_2'}} D_y^{S_0T_2'} D_x^{S_0T_1'} \\
=&- \frac{\bar{L}_z^{S_1'T_2'}}{\Delta_{S_1'T_2'}} \lambda D_y^{S_0S_2} D_x^{S_0S_1} \\
&- \frac{\bar{L}_z^{T_1'T_2'}}{\Delta_{T_1'T_2'}} \cancelto{0}{sin^2\lambda} D_y^{S_0S_2} D_x^{S_0SS_1} \\
=&\frac{\lambda \bar{l}_z^{H,H-1}}{\sqrt{12}\Delta_{S_1'T_2'}} D_y^{S_0S_2} D_x^{S_0S_1} \\
=&\frac{\lambda \bar{l}_z^{H-1,H}}{\sqrt{12}\Delta_{T_2'S_1'}} D_y^{S_0S_2} D_x^{S_0S_1}
\end{aligned}
\tag{D.29}
$$

D.2 Spin Populations

With the eigenfunctions shows in Equation D.13, expressions for the fragment spin populations can be derived. For a discussion on how these are obtained from Slater determinants, please see [6], page 307.

For clarity, let:

$$A = \frac{sin\lambda}{\sqrt{2}} \tag{D.30a}$$

$$B = \frac{cos\lambda}{\sqrt{2}} \tag{D.30b}$$

$$C = \frac{sin\lambda}{\sqrt{6}} \tag{D.30c}$$

$$D = \frac{cos\lambda}{\sqrt{6}} \tag{D.30d}$$

so for the spin populations within the sing-doublet state, $|S_1, {}^1\!/_2\rangle$,

$$\rho_{\text{Cat}} = 4D^2 - 4BD \tag{D.31a}$$

$$\rho_{\text{bpy}} = 4D^2 + 4BD \tag{D.31b}$$

$$\rho_{\text{NN}} = 2B^2 - 2D^2 \tag{D.31c}$$

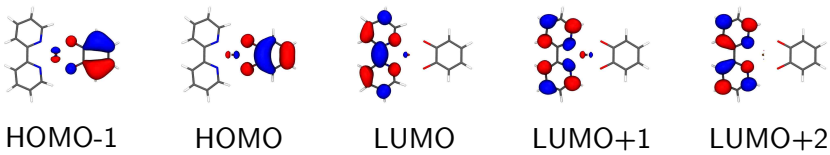

Figure D.1: CASSCF(4,5) active space orbitals of (bpy)Pt(cat).

and for the trip-doublet state, $|T_1, {}^1/_2\rangle$,

$$\rho_{\text{Cat}} = 4AC + 4C^2 \tag{D.32a}$$

$$\rho_{\text{bpy}} = -4AC + 4C^2 \tag{D.32b}$$

$$\rho_{\text{NN}} = 2A^2 - 2C^2 \tag{D.32c}$$

D.3 Computational Results

All calculations were performed with the ORCA 3.0.1 or 3.0.2 program suite[7]. Density functional theory (DFT) geometry optimizations were done with the def2-TZVP basis and the PBE GGA functional. CASSCF/NEVPT2 calculations used quasi-restricted orbitals (QROs) from the DFT calculations as the initial guess orbitals. Minimal active space calculations (CAS(3,3) or CAS(2,2) for radical elaborated or non-elaborated compounds, respectively) were first performed, and the molecular orbitals obtained were used for subsequent calculations using larger active spaces (see Appendix D). MCD spectra were calculated using the quasi-degenerate perturbation theory (QDPT) spin-orbit coupling module in ORCA[8].

Calculations of the parent (bpy)Pt(catechol) complex were performed to get an accurate estimate of J', the parent singlet-triplet splitting. To this end, a CASSCF(4,5) calculation was done with the 6 lowest S=0 states and 5 lowest S=1 states. The active space is shown in Figure D.1. The singlet-triplet splitting of the HOMO $\rightarrow$ LUMO was found to be quite sensitive to the number of states included in the state-averaging

procedure, with large numbers of states resulting in a reduction in the singlet-triplet gap[3]. In addition the NEVPT2 corrections were found to decrease this gap as well, often reducing it to an unrealistically small number or flipping the state ordering[4]. The results shown below give a 2J' of 2619.4 cm^{-1}, which is in excellent agreement with the experimentally determined value given in the text.

```
------------------------------
SA-CASSCF TRANSITION ENERGIES
------------------------------

LOWEST ROOT (ROOT 0 ,MULT 1) = -19994.583591377 Eh -544080.280 eV

STATE   ROOT MULT  DE/a.u.    DE/eV    DE/cm**-1
   1:    0    3   0.020081     0.546   4407.3
   2:    1    1   0.032016     0.871   7026.7
   3:    1    3   0.080239     2.183  17610.4
   4:    2    1   0.080823     2.199  17738.6
   5:    2    3   0.084713     2.305  18592.4
   6:    3    1   0.085314     2.322  18724.3
   7:    3    3   0.094397     2.569  20717.7
   8:    4    1   0.094897     2.582  20827.4
   9:    4    3   0.144204     3.924  31649.2
  10:    5    1   0.144490     3.932  31712.0
```

The MCD spectrum of (bpy)Pt(cat-NN) was calculated in a similar fashion as

[3]This is to be expected, as the inclusion of additional states in the averaging procedure will reduce the accuracy of the description of any given state.

[4]Careful selection of the orbitals used in the NEVPT2 calculation may assist (see the documentation for `nev_canonstep` in the ORCA manual.) with this problem.

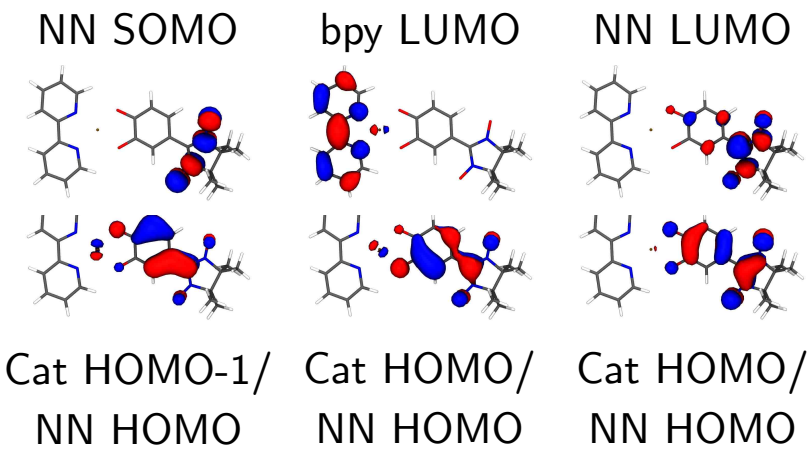

Figure D.2: CASSCF(7,6) active space orbitals of (bpy)Pt(cat-NN).

above, with the active space being extended to CASSCF(7,6), which was created by the addition of the NN-SOMO, HOMO, and LUMO while removing the bpy LUMO+1 and LUMO+2 (Figure D.2). A calculation with this active space and 10 roots results in the MCD spectrum shown in Figure D.3. The lower energy negative C-term feature is assigned as a transition to the trip-doublet state, with the higher energy positive feature assigned as the sing-doublet. This is in excellent agreement with the model presented above. The only limitation of these CASSCF calculations is the apparent underestimation of J' when using using many roots in the state averaging procedure which overestimates the absorption intensity of the trip-doublet state. This could likely be corrected by careful selection of the states included in the averaging procedure or with more advanced (but very expensive!) SORCI calculations.

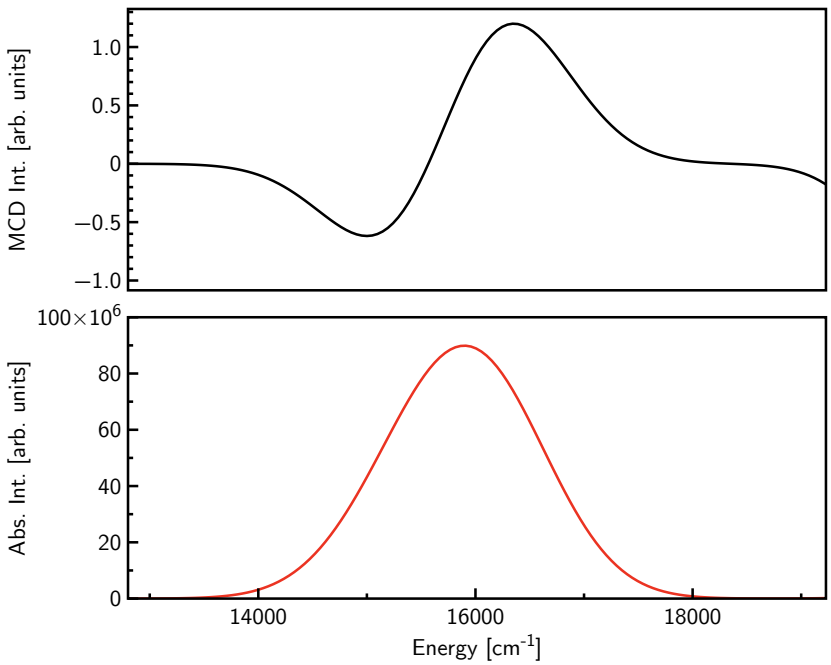

Figure D.3: CASSCF(7,6) MCD spectrum of (bpy)Pt(Cat-NN).

D.4 References

(1) Westphal, A.; Broda, H.; Kurz, P.; Neese, F.; Tuczek, F. *Inorg. Chem.* **2012**, DOI: 10.1021/ic300201t.

(2) Bencini, A.; Gatteschi, D., *EPR of Exchange Coupled Systems*; Dover Publications: Mineola, NY, 2012.

(3) Buchachenko, A. L.; Berdinsky, V. L. *Chem. Rev.* **2002**, *102*, 603–612, DOI: 10.1021/cr010370l.

(4) Szabo, A.; Ostlund, N. S., *Modern Quantum Chemistry : Introduction to Advanced Electronic Structure Theory*; Dover Publications: Mineola, NY, 1996.

(5) Neese, F.; Solomon, E. I. *Inorg. Chem.* **1999**, *38*, 1847–1865, DOI: 10.1021/ic981264d.

(6) Kahn, O., *Molecular magnetism*; Wiley-VCH: New York, 2001.

(7) Neese, F. *WIREs Comput Mol Sci* **2012**, *2*, 73–78, DOI: 10.1002/wcms.81.

(8) Ganyushin, D.; Neese, F. *J. Chem. Phys.* **2008**, *128*, 114117, DOI: 10.1063/1.2894297.

Appendix E

Calculation of the Missing Mode Effect

The missing mode effect (MIME)[1] describes a situation in which an observed vibronic progression does not correspond to any known vibrational modes of a molecule. This interesting phenomenon arises from a combination of at least two vibrational modes which are distorted upon excitation of a molecule, and is related to the time-dependent overlap of the excited state wavepacket. When both modes have returned to their initial point, a peak in the overlap is seen and causes an effective frequency which is a weighted average of the constituent modes. A simplification of the MIME results in an easy to evaluate equation[2]:

$$\omega_{eff} = \frac{\sum_k (\omega_k^2 \Delta_k^2) + 4\Gamma^2}{\sum_k \omega_k \Delta_k^2 n_k} \tag{E.1}$$

which can be solved with a small computer script. The only necessary parameters are a list of normal mode frequencies, ω and displacements, Δ along with a gaussian damping factor Γ. The equation is solved self-consistently, as the n_k factors are dependent upon the calculated effective frequency, and so can change in an iterative fashion.

Here is a python program which calculates the missing mode, as described in [2], Equation 6.

```
from itertools import izip

# Parameters are from Tutt 1987, Figure 1
# Simply replace with those of your choice.
initialMimeGuess = 500
gamma = 130
freqs = [500,1100]
ddncs = [1.7, 1.7]

# Calculate MIME frequency
newGuess = initialMimeGuess
print "\n Calculating MIME."
# Iterate, updating the n_k each cycle.
while True:
        nk = []
        numerator = 0.0
        denominator = 0.0
        print 'Current guess: {:.0f}'.format(newGuess)
        for freq,diff in izip(freqs,ddncs):
                currentNk = round(freq/newGuess)
                nk.append(currentNk)
                numerator += freq**2 * diff**2
                denominator += freq * diff**2 * currentNk

        numerator += 4 * gamma**2
```

```
        effectiveFreq = numerator/denominator
        print 'New effectiveFreq = {:.0f}'.format(effectiveFreq)
        # Check if the MIME frequency has not changed from the
        # previous cycle...if not we're done.
        if abs(newGuess - effectiveFreq) < 1:
                break
        else:
                newGuess = effectiveFreq

print 'MIME frequency: {:.0f}'.format(effectiveFreq)
```

E.1 References

(1) Tutt, L.; Tannor, D.; Heller, E. J.; Zink, J. I. *Inorg. Chem.* **1982**, *21*, 3858–3859, DOI: 10.1021/ic00140a057.

(2) Tutt, L. W.; Zink, J. I.; Heller, E. J. *Inorg. Chem.* **1987**, *26*, 2158–2160, DOI: 10.1021/ic00260a029.